Politecnico di Torino

ScuDo
Scuola di Dottorato ~ Doctoral School
WHAT YOU ARE, TAKES YOU FAR

Doctoral Dissertation
Doctoral Program in Mechanical Engineering (36^{th}cycle)

Global/local and coupled high order FEM-Peridynamics models for fracture analysis of isotropic and composite structures

By

Marco Enea

******

Supervisor(s):
Prof. Erasmo Carrera, Supervisor
Prof. Matteo Filippi, Co-Supervisor
Prof. Alfonso Pagani, Co-Supervisor

Doctoral Examination Committee:
Prof. Sara Bagassi , Referee, Università di Bologna
Prof. Mirco Zaccariotto, Referee, Università degli studi di Padova

Politecnico di Torino
2024

Declaration

I hereby declare that, the contents and organization of this dissertation constitute my own original work and does not compromise in any way the rights of third parties, including those relating to the security of personal data.

Marco Enea
2024

* This dissertation is presented in partial fulfillment of the requirements for **Ph.D. degree** in the Graduate School of Politecnico di Torino (ScuDo).

Alla mia famiglia

Acknowledgements

First, I would like to extend my deepest gratitude to my supervisors, Prof. Erasmo Carrera, Alfonso Pagani, and Matteo Filippi, for their continuous guidance and timely supervision during the PhD. Prof. Erasmo Carrera's priceless guidance was a fundamental contribution to my professional and personal growth. Prof. Alfonso Pagani and Matteo Filippi have provided me with constant help during every step of my activities and have encouraged me with their devotion to research. I am also profoundly grateful to Prof. Marco Petrolo and Enrico Zappino for their constant and kind support. The most significant takeaway I'll carry from my time in the MUL2 Group is the realization that with passion and dedication, nothing is truly impossible. I express my gratitude to all of you for this invaluable gift. Thank you to all the colleagues who shared with me all the highs and lows of these years. A special thank goes to Alberto, Mattia, Rebecca and Rodolfo. I was lucky to find in you not only colleagues, but also real friends.

I would like to acknowledge DEVISU project, funded by Ministero dell'Istruzione, dell'Universitá della Ricerca research programme PRIN 2017.

I am truly grateful to my parents and sister for their continuous support and encouragement. I could not have done this without you. Thanks also to the rest of my relatives, particularly my grandparents and the Cittati family.

Last but not least, my recognition goes to you, Giuliana, for always being there for me all these years. You have been and will always be the sunshine that, even from afar, illuminates my days with its light.

Marco Enea

Abstract

In industrial practice, design and maintenance phases mainly rely on similitudes and past experience to characterize the current integrity state and to take into account its effect on performance. However, this approach can easily lead to unjustified heavy structures or not ideal inspection procedures and intervals. This thesis aims to provide high-fidelity numerical models that can be integrated with data from experience to support design and maintenance procedures. The framework relies on higher-order structural theories based on the well-established Carrera Unified Formulation (CUF). CUF is a generalized hierarchical formulation that generates a class of refined structural theories through variable kinematic description. CUF-based models can provide accurate 3D-like stress fields at a reduced computational cost, e.g., approximately one to two orders of magnitude of degrees of freedom less than standard 3D brick elements.

CUF-based finite element models are combined with a Hashin-based orthotropic damage model for dealing with damage in fibre-reinforced composite materials. This method belongs to the family of computational models based on the so-called Continuum Damage Mechanics (CDM). Hence, cracks are smeared out within the volume of the finite element, degrading the stiffness of the involved material points. The proposed method's main novelty lies in its capability to consider a full three-dimensional stress state to describe the damage propagation. Furthermore, this approach can also view three independent failure modes: fibre, matrix and interlaminar.

In order to deal with progressive failure analysis, CUF-based Finite Elements (FE) are also coupled with Peridynamics (PD). PD is a non-local formulation capable of coping with discontinuities, such as cracks. The PD theory does not suffer from the inapplicability of the classical continuum mechanics theory when cracks or interfaces happen due to the integro-differential nature of the governing equations. Thus, PD presents a unique capability of analyzing damage and progressive failure of materials and structures by directly predicting the displacements, crack nucleation

and propagation with arbitrary paths without any special numerical techniques or criteria.
Furthermore, a global-local approach has been extended to deal with the refined local analysis of larger regions. This new feature will allow us to perform, among others, optimization analysis on areas of higher interest, such as an aircraft wing patch. This approach has then been combined with the previously mentioned coupled FEM-PD models for dealing with progressive failure analysis in specific regions of large structures, for example, in regions where a crack is more likely to develop or has been detected in previous inspections.
Finally, CUF-based finite element models have also been employed as a data generator for the training of data-driven deep learning approaches, to create a complete mapping of damages in aeronautical structures, even considering those occurring in localized components.

Contents

List of Figures

List of Tables

Chapter 1

Introduction

1.1 Characterization of failure in isotropic and composite structures

Continuum damage mechanics

Progressive damage analysis presents significant challenges, particularly in composite laminates, owing to the diverse failure modes that manifest under specific loading conditions and the interactions between these modes. The failure modes in composites are inherently complex. Their accurate representation in a numerical material model while preserving the physical aspects of damage progression and its impact on structural integrity is a non-trivial endeavor. A family of computational models to simulate progressive damage is based on the so-called Continuum Damage Mechanics (CDM). They are quite widespread in recent literature due to their relative simplicity in terms of implementation and lower computational costs when compared to different approaches. Due to these challenges, composite material models based on continuum damage mechanics are currently very spread in the literature. In these continuum-based approaches, the cracks within the composite matrix are smeared out throughout the finite element volume, and their effects are characterized by damage parameters that influence the material point's stiffness within the overall structure. The process of smearing out the crack ensures mesh continuity, avoiding the need for computationally intensive discontinuity handling techniques and enhancing the efficiency of continuum models. However, a notable drawback of

this approach is its strong dependence on mesh refinement, as the crack width is influenced by the finite element size. To mitigate this issue, mesh dependency is commonly addressed through the adoption of crack-band theory [1], which scales the constituent fracture energy using an appropriate length parameter typically derived from the finite element dimensions. The concept of CDM was first introduced by Kachanov [2] to describe creep damage in metallic materials, where damage was characterized by a scalar internal state variable. After this, Lemaitre and Chaboche [3] applied applied Kachanov's work to analyze materials with distributed cavities and cracks. Further progress in CDM theory was made by Krajcinovic [4], who not only linked CDM theory with concepts from fracture mechanics and plasticity but also explored its thermodynamic implications. Regarding the application of CDM to composites, one of the earliest endeavors was by Talreja [5], who later expanded the theory to predict damage evolution in cross-ply laminates [6]. Other notable CDM theories for laminate analysis include those proposed by Matzenmiller et al. [7] and Ladeveze et al. [8, 9]. In this research, an orthotropic damage model that considers a full 3D stress state for the evaluation of the failure onset and damage propagation is considered.

Peridynamics and coupled models

The CDM category has the advantage of relatively low computational costs. Nevertheless, CDM is not able to involve the explicit geometrical representation of cracks within the structure. For doing so, Discrete Damage Models (DDM) can be employed. This method offers a physically realistic representation of damage mechanisms and their interactions, albeit requiring significant computational resources. In discrete modeling, interface elements are commonly employed, utilizing cohesive zone modeling to replicate matrix cracks within plies and delamination between plies [10–13]. Alternatively, discrete modeling techniques may involve the eXtended Finite Element Method (XFEM), which employs enriched kinematics to depict the displacement discontinuity across cracks [14]. However, the use of DDM does not solve the issue related to the spatial partial derivatives, which are used to define stress and strain in a body. In fact, even adopting these methods will lead to undefined or ill-suited derivatives when dealing with discontinuities. Thus, these numerical methods still suffer from a lack of simulation accuracy and low efficiency when handling complex problems. For example, neither CDM nor DDM can take into

account the spontaneous nucleation and propagation of multiple interacting cracks when the structure is subjected to complex three-dimensional loading conditions. Acknowledging that the inherent limitations of conventional methods for approximating the mathematical expressions of classical continuum mechanics cannot be fully addressed solely by integrating specialized techniques into standard numerical methods (e.g., FEM), Silling [15] introduced a peridynamic formulation of elasticity theory to handle discontinuities and long-range forces.

The peridynamics theory overcomes the limitations of classical continuum mechanics theory in cases involving cracks or interfaces. It offers a distinct ability to analyze material and structural damage, as well as progressive failure, by directly predicting displacements, crack initiation, and propagation along arbitrary paths without relying on specialized numerical techniques or criteria. Xu et al. [16] applied peridynamics to analyze damage and failure in composite structures. Silling and Askari [17] developed a peridynamics-based damage model to investigate crack initiation and propagation under cyclic loading. Ha and Bobaru [18, 19] explored dynamic brittle fractures using peridynamics. Madenci et al. [20] developed a methodology for examining crack propagation in structures subjected to complex loading conditions. The non-locality feature of PD and its capability to deal with discontinuities are key factors that make PD a powerful tool for crack propagation analysis. However, these aspects would represent a significant drawback when used to analyse large structures, due to the exponential increase of the computational costs. In fact, since every point of a PD grid interacts with all points within its neighbourhood, PD-based numerical methods are computationally more expensive than those based on classical mechanics, such as FEM, where the interaction is limited to the nodes of adjacent elements. This issue is amplified when implicit numerical schemes are adopted, and the tangent stiffness matrix has to be computed because the number of non-zero elements produces a not negligible bandwidth in the matrix [21]. Finally, applying boundary conditions on a PD domain introduces some difficulties due to the problem of boundary condition definitions in non-local theories. Several studies have been conducted to overcome this limitation in imposing boundary conditions [22–24]. Concerning the demanding computational cost, a promising strategy is the coupling of PD with a numerical method based on classical continuum mechanics, such as FEM. In this way, the advantages of both methods can be exploited, for example, by introducing a PD grid in small regions where the crack is likely to develop and modelling the remaining domain with FEM discretization. Several

methods have been proposed in past years for the coupling of PD grids with FEM subdomains, i.e., [25–32]. It should be noted that most of the methods presented in literature couple dimensionally consistent domains, such as 1D FEs with 1D PD grids, 2D FEs and 2D PD grids. Nevertheless, when cases of practical interest are investigated, an accurate 3D description of the problem is required, making using 3D FEs and 3D PD grids unavoidable, leading to potentially prohibitive computational costs.

From classical to high order structural theories

The necessity of accurate numerical models for high-fidelity design and analysis of structures is one of the main issue in structural mechanics. This applies especially when complex assemblies, i.e. aeronautical structural components, are considered. In fact, a typical composite laminate can reach a scale ratio between the main dimension and the single-ply thickness of 10^4. Generally, the finite element method is used to predict the structural behavior of composite laminates. However, the large-scale ratio value leads to highly time-consuming mathematical models, especially if 3D elements are adopted.

One approach to address this challenge involves employing advanced reduced-dimensional numerical models. One-dimensional (beam) classical theories, as Timoshenko Beam Theory (TBT) [33], and Euler-Bernoulli Beam Theory (EBBT) [34], as well as two-dimensional (plate/shell) theories, such as Reissner-Mindlin plate theory [35] and Kirchhoff theory [36], often encounter significant limitations because of the simplifying kinematic assumptions inherent in their formulation. These limitations result in inadequate resolution of kinematic fields in the cross-section of one-dimensional models and throughout the thickness of two-dimensional models, making them ill-suited for many problems that necessitate accurate three-dimensional resolution.

A generalized framework to generate higher-order structural theories with a variable kinematic description was introduced by Carrera, and is known as the Carrera Unified Formulation (CUF). Originally developed as a method to obtain 2D structural theories [37, 38],CUF has evolved into a computational framework for deriving classical and higher-order 1D (beam) and 2D (plate/shell) structural theories in a fully generalised manner, eliminating the necessity for ad-hoc modifications of the

framework [39]. This formulation utilizes two-dimensional expansion functions and one-dimensional thickness functions to characterize the cross-sectional and thickness kinematics of 1D and 2D models, respectively, resulting in a three-dimensional representation of field variables and outcomes that rival the accuracy of full 3D models but with significantly reduced computational costs. For comprehensive coverage, readers are directed to [40–48] for various engineering applications of the CUF.

Global/local approach

A different solution to the problem of huge computational cost required for accurate numerical models is represented by the adoption of a global/local approach. This technique can provide a reduction in terms of simulation time, keeping a high level of accuracy. Early research works developed in the past decades with limited computing power were successfully applied to linear [49–52] and non-linear [53, 54] analysis. A distinction between the different approaches described in the literature is between two-way [55–60] and one-way couplings [61–64]. The first approach involves exchanging information between global and local models in both directions, whereas one-way couplings involve information transferring from the global model to the refined local model just once. The global/local approaches can be applied for a more reliable stress analysis of a composite laminate. More specifically, phenomena that may occur within a composite structure; i.e., free-edge effects and failure, demand a 3D description of the stress distribution. Thus, 3D solid elements can be used at the local level [65]. If a typical aeronautical lay-up with tens of layers is considered, even a relatively small region analysis leads to a considerable number of solid elements. Therefore, aircraft companies and composite designers must rely on experimental rules, such as Angle Minus Longitudinal (AML) method [66]. Furthermore, classical theories are not able to accurately describe the 3D effects that arise at the free-edge of a composite laminate due to the mismatch of the mechanical properties of different ply in a composite laminate. Recently, a global/local approach with one-way coupling has been proposed, where the global analysis is performed using the commercial software Nastran. Then, a local region is investigated using advanced layer-wise models based on CUF. This strategy provides accurate solutions for stress and strain transverse components, which can be essential when the onset of failure in laminates has to be predicted. Recent works [67, 68] have shown this

global/local approach's capability to recover the 3D stress state at the ply level accurately. However, in these researches, a so-called element-wise (EW) formulation is used, meaning that a single global element can be chosen as the local area to be analyzed through advanced LW theories, leading to some limitations in terms of accuracy and dimension of the region to locally refined.

Damage detection

A preliminary step for the failure characterization, before the analysis of its propagation, is represented by the identification and quantification of the damage. For instance, aircraft manufacturers must adhere to a predetermined maintenance schedule to guarantee the success and safety of operations. These schedules rely on Non-Destructive Testing (NDT) techniques, including visual inspection, eddy current testing, thermography, and ultrasonic inspection [69]. Nonetheless, NDT methods encounter certain limitations, such as difficulty in detecting damage in specific areas of the structure, the requirement to anticipate potential damage locations beforehand, and considerable operational costs. For this reason, structural health monitoring techniques (SHM) have emerged as a crucial area of research in recent years. The goal of SHM is to detect, localize, quantify, and classify damage [70]. Various techniques are being developed for SHM applications in composite materials, including Lamb-waves [71, 72], distributed optical fibre sensors [73, 74] and intelligent coating monitoring [75]. However, in recent years, researchers have directed their efforts towards uncovering the unknown relationship that may exist between a measured quantity and the distribution of damage. This relationship can be discerned by employing artificial intelligence (AI) techniques, such as Artificial Neural Networks (ANN). Various types of input can be utilized to train these neural networks, enabling them to learn the correlation between input data and patterns of damage. Examples of employed input include dynamic parameters [76, 77] and static parameters [78], frequency response functions (FRFs) [79], and wavelet transform coefficients [80]. The proposed study initially explores the impact of localized damages on the alterations in the vibrational characteristics of the structure, such as changes in natural frequencies or mode shapes. Numerous investigations [81–84] have demonstrated that damage significantly influences the dynamic parameters of a structure. Consequently, the inverse problem can be addressed: given the dynamic parameters of a structures, such as natural frequencies and mode shapes (or a combination of thereof), FRFs

and modal strain energy, an ANN is employed to obtiain both location and severity of all damages. Sahin and Shenoi introduced a methodology that integrates both global (alteration in natural frequencies) and local (curvature mode shapes) dynamic analysis information as input for the ANN. This method has been implemented in the analysis of beam-like structures [85] and laminated composites [76]. Das and Pahri employed the relative discrepancy in the first three natural frequencies and mode shapes of a cantilever beam to train the ANN [86]. Suresh et al. introduced a modular method to detect crack location and depth in a beam, employing two different ANNs: one for guessing the crack location and the other for determining the crack depth [87]. Jayasehar and Sumangala examined prestressed concrete beams by employing natural frequency measurements as dynamic data, in conjunction with parameters such as deflection, crack width, first crack load, and ultimate load [88]. aeed et al. conducted finite element analysis to compute natural frequencies and FRFs in both damaged and undamaged curvilinear beams, utilizing the deviation in these parameters (from undamaged to damaged) to train four types of ANNs [89]. Aydin and Kisi integrated material and geometrical characteristics of the beam into the neural network, introducing mode shape rotation deviations alongside natural frequencies for the first time [90]. Fathnejat et al. employed the Modal Strain Energy Based Index (MSEBI) as input for a Cascade Feed Forward Neural Network (CFFNN) to identify the location of damage [91]. However, when faced with more complex challenges, ANNs could have some difficulties in terms of overfitting and bad generalization.To address this, a deep-learning technique known as Convolutional Neural Network (CNN) [92] has recently gained attention for damage detection applications [93–96]. Additionally, the utilization of dynamic parameters as training input has proven to be ineffective for monolithic structures [97], such as composite laminates. This is because computing higher-frequency modes becomes necessary to acquire adequate information for damage detection. Consequently, static parameter images (strain or displacement) are employed to establish the unknown correlation with damage distribution, often in conjunction with CNNs. For instance, in [98], a CNN is trained using numerically-simulated raw strain measurements for tasks related to detecting and localizing structural connections. In [99], a novel monitoring technique based on Digital Image Correlation (DIC) [100] is introduced. Two-dimensional axial strain images derived from numerical analysis serve as input for training CNNs. Meanwhile, [101] proposes a damage identification method leveraging strain mode differences and the inverse Finite Element Method (iFEM). Notably, the advantage

of this approach lies in its reliance solely on a series of low-order damaged data for strain mode differences. In current literature, raw data for data-driven training are typically acquired from conventional Finite Element (FE) models, as seen in [102]. However, these models often fail to capture certain mechanical behaviors, such as shear or thickness stretching. Such simplifications can result in an incomplete depiction of the effects coming from localized damages, such as delamination in composite material structures. Hence, this study aims to underscore the significance of structural modeling in neural network training.

1.2 Objectives

This thesis aims to build a framework that can address the challenges described in previous section, thus providing efficient and effective tools for dealing with progressive failure analysis and damage detection in both isotropic and composite structures. Concerning the latter, a Hashin-based orthotropic damage model has been proposed and combined with CUF-based finite elements to solve progressive failure analyses in composite laminates. An alternative method is represented by coupling 1D and 2D higher-order finite elements with 3D peridynamic grid. Two different coupling approaches are proposed in order to carry out static and progressive failure analysis. Nevertheless, the computational cost of these simulations can still be prohibitive for large or complex structures. Thus, the existent global/local tool has been first extended to a patch-wise (PW) formulation. In this case, the local region to be refined can be chosen as large as required. This extension allows us to analyze more significant areas of a complex structure and evaluate 3D stress states and failure onset while reducing the computational demand of the analysis. Furthermore, the possibility of arbitrarily choosing large regions permits to embed coupled FEM/PD model within the global/local tool for progressive failure analysis in localized zones of the structure. Regarding the damage detection challenge, the capabilities of CUF are exploited in this research to create a more extensive simulation-based database for training an ANN or CNN. Static or dynamic parameters are employed to feed the neural networks, whose output is represented by quantifying and localising all damages in a multi-component structure.

1.3 Thesis outline

The thesis is organized in two parts, each addressing one of the previously mentioned objectives. The content of the thesis is described in the following.

1.3.1 Part I

- **Chapter 2** introduces a novel Hashin-based orthotropic damage model for fibre-reinforced composite materials. The proposed method's main novelty lies in its capability to consider a full three-dimensional stress state to describe the damage propagation in composite laminates.
- **Chapter 3** presents the governing equation of peridynamics. First, a continuum formulation is proposed for the general state-based theory. Then, a meshfree method with uniform grid is employed to discretize the peridynamic body. The capability of peridynamics when dealing with crack propagation analysis is also made clear by introducing the algorithm implemented in this thesis.
- **Chapter 4** introduces the higher-order one-dimensional (1D) and two-dimensional (2D) models used in this work, developed within the CUF framework. The kinematics of beams and plates are expressed through a generic expansion of generalized displacements, incorporating arbitrary cross-sectional and thickness functions. By selecting different types and orders of functions, diverse beam, plate, and shell theories can be derived. In this research, both Lagrange-like (LE) and Taylor-like (TE) polynomials are considered. Following the CUF framework and incorporating Finite Element Method (FEM), the governing equations are expressed in a general yet unified and concise manner using Fundamental Nuclei (FNs). These FNs act as the fundamental elements of the proposed theory, using the Principle of Virtual Displacements (PVD).
- **Chapter 5** is devoted to the introduction of the coupling of higher-order 1D and 2D CUF-based finite elements with 3D PD sub-regions are presented. Two different procedures have been implemented. The first approach is based on the use of Lagrange multipliers at the interface between the FEM and PD domains, whereas the second method relies on the imposition of displacement continuity between the two regions.

- **Chapter 6** proposes a global/local approach adopted for the analysis of three-dimensional stress states of composite laminated structures. This two-step procedure, as a first step, makes use of finite element modelling based on classical 2D plate elements by using commercial FE software, whereas a refined layer-wise model based on CUF is employed to extract the 3D stress and strain fields in some critical regions that may have arbitrary dimensions. Moreover, the proposed method is extended to deal with localized progressive failure analysis using coupled FEM-PD models within the local refined domain.

- **Chapter 7** proposes a selection of numerical examples obtained by adopting the formulations and techniques presented in previous chapters. First, progressive failure analyses are performed using the continuum Hashin-based orthotropic model in fibre-reinforced composite laminates. Then, outcomes from static and progressive failure analyses performed using coupled FEM-PD models are presented. Finally, numerical examples that make use of the global/local approach are proposed for stress evaluation in composite structures, with a supplementary model where a global/local method is adopted for localized progressive failure analysis through coupled FEM-PD models.

1.3.2 Part II

- **Chapter 8** presents the numerical strategies and techniques employed in this work for damage detection purposes. First, the component-wise formulation within the CUF framework is illustrated, and its advantages when dealing with damage modelling are explained. Finally, the necessity of using higher-order theories to build high-fidelity models to be adopted for damage mapping is made clear by presenting the results from two different cases.

- **Chapter 9** is devoted to introducing two different AI techniques for damage detection. A vibration-based method is first introduced, where a structure's vibrational characteristics (e.g., natural frequencies and Modal Assurance Criterion (MAC) scalars) are employed as input. The influence of damage in aeronautical structures is first demonstrated in this chapter. Then, the procedure adopted to solve the inverse problem using ANN is illustrated. The second proposed technique uses displacement and strain field images to completely map damages in composite laminates. A Convolutional Neural

Network (CNN) architecture is employed here. The common feature between the two methods is the creation of a training database using CUF-based models, allowing a component-wise modelling of the structures and thus the capability of introducing a different damage in each component of the structure.

- **Chapter 10** proposes a selection of numerical examples obtained adopting the formulations and damage detection techniques presented in Chapters 8 and 9. First, the vibration-based method is applied to aeronautical thin-walled structures, considering an isotropic damage model. Then, convolutional neural networks are employed to predict damage location and intensity using displacement and strain field images as training database in composite laminates.
- **Chapter 11** provides an overview of the current study and offers concluding observations to underscore the noteworthy results of this thesis. Additionally, it suggests potential research avenues as subjects for future inquiries, building upon the advancements made during the duration of the ongoing PhD program.

Part I

Progressive failure analysis via coupled high order local-non-local models

Chapter 2

Continuum damage modelling

This chapter is devoted to a detailed description of a Hashin-based orthotropic damage model. It is here used for dealing with damage in fibre-reinforced composite materials. This method belongs to the family of computational models based on the so-called Continuum Damage Mechanics (CDM). Hence, cracks are smeared out within the volume of the finite element, degrading the stiffness of the involved material points. The proposed method's main novelty lies in its capability to consider a full three-dimensional stress state to describe the damage propagation. Furthermore, this approach can also consider three independent failure modes: fibre, matrix and interlaminar. The stiffness formulation is first presented, and then the failure onset and evolution mechanism are presented.

2.1 Hashin-based orthotropic model

This section offers an outline of the orthotropic damage model utilized in the current investigation. Initially, it presents the constitutive relation for a damaged material, encompassing the characterization of the damage variables. Subsequently, the initiation of failures is introduced in relation to failure criteria. Finally, it illustrates the linear damage evolution law that describes the progression of failure for the independent crack modes.

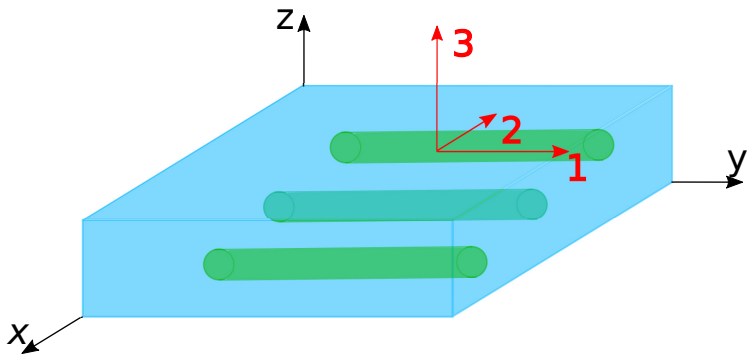

Fig. 2.1 Global (in black) and material (in red) reference frames. Direction 1 for the material frame represents the fiber direction, whereas 2 and 3 are the transversal directions.

2.1.1 Stiffness formulation

The current orthotropic model addresses the construction of the secant stiffness matrix in the damaged state, denoted as $\mathbf{C}^{\mathrm{d}}$, which is employed for calculating the constitutive elastic stress-strain relationship. This is accomplished by computing the stiffness matrix $\mathbf{C}^{\mathrm{d}}$ through the inversion of the compliance matrix $\mathbf{S}^{\mathrm{d}}$ (Eq. 2.1).

$$\mathbf{S}^{\mathrm{d}} = \begin{bmatrix} \frac{S_{11}}{1-d_f} & S_{12} & S_{13} & 0 & 0 & 0 \\ S_{21} & \frac{S_{22}}{1-d_m} & S_{23} & 0 & 0 & 0 \\ S_{31} & S_{32} & \frac{S_{33}}{1-d_i} & 0 & 0 & 0 \\ 0 & 0 & 0 & \frac{S_{44}}{1-ds_{12}} & 0 & 0 \\ 0 & 0 & 0 & 0 & \frac{S_{55}}{1-ds_{13}} & 0 \\ 0 & 0 & 0 & 0 & 0 & \frac{S_{66}}{1-ds_{23}} \end{bmatrix} \tag{2.1}$$

With

$$\begin{gathered} S_{jj} = \frac{1}{E_{jj}}, \quad S_{jk} = S_{kj} = \frac{\nu_{jk}}{E_{jj}} = \frac{\nu_{kj}}{E_{kk}}, \quad j,k = 1,2,3, \quad j \neq k \\ S_{44} = G_{12}, \quad S_{55} = G_{13}, \quad S_{66} = G_{23} \end{gathered} \tag{2.2}$$

Subscript 1 in Eq. (2.1) refers to the fiber direction in the material reference system (in red), whereas subscripts 2 and 3 represent the transversal directions. Constructing the compliance matrix involves incorporating damage terms along the main diagonal to ensure model consistency and thermodynamic admissibility [7, 103, 104]. The damage variables d_f, d_m, and d_i correspond to fiber, matrix, and interlaminar failure modes, respectively, with both tensile and compressive behaviors activated using the

relative effective stress $\hat{\sigma}_j$ [105]::

$$\hat{\sigma}_j = \frac{\sigma_j}{1-d_j}, \qquad j = 1,2,...,6 \tag{2.3}$$

With

$$\begin{aligned} d_f = d_1 &= \begin{cases} d_{ft} & \text{if } \hat{\sigma}_1 \geq 0 \\ d_{fc} & \text{if } \hat{\sigma}_1 \leq 0 \end{cases} \\ d_m = d_2 &= \begin{cases} d_{mt} & \text{if } \hat{\sigma}_2 \geq 0 \\ d_{mc} & \text{if } \hat{\sigma}_2 \leq 0 \end{cases} \\ d_i = d_3 &= \begin{cases} d_{it} & \text{if } \hat{\sigma}_3 \geq 0 \\ d_{ic} & \text{if } \hat{\sigma}_3 \leq 0 \end{cases} \end{aligned} \tag{2.4}$$

The terms ds_{12}, ds_{13} and ds_{23} regulate the shear damage evolution, that is affected by the fiber, matrix, and interlaminar damages, as stated in the following equation:

$$\begin{cases} ds_{12} = d_4 = 1 - \left(1-d_{ft}\right)\left(1-d_{fc}\right)\left(1-d_{mt}\right)\left(1-d_{mc}\right) \\ ds_{13} = d_5 = 1 - \left(1-d_{ft}\right)\left(1-d_{fc}\right)\left(1-d_{it}\right)\left(1-d_{ic}\right) \\ ds_{23} = d_6 = 1 - \left(1-d_{mt}\right)\left(1-d_{mc}\right)\left(1-d_{it}\right)\left(1-d_{ic}\right) \end{cases} \tag{2.5}$$

The comprehensive formulation of stiffness and the validation of thermodynamic consistency are provided [106, 107].

2.1.2 Failure onset and damage evolution

The onset of damage relies on the current stress field throughout the material. The damage mechanisms considered in this framework include both tensile and compressive failure modes. The simplifications applied in the proposed model are outlined in [108] and [107]. The fiber damage initiation in the longitudinal direction takes place when the failure criterion $F_f = 1$, where:

$$F_f = \begin{cases} F_{ft} = \left(\frac{\hat{\sigma}_1}{X_t}\right)^2 + \frac{\hat{\tau}_{12}^2 + \hat{\tau}_{13}^2}{S_L^2}, & \text{if } \hat{\sigma}_1 \geq 0 \\ F_{fc} = \left(\frac{\hat{\sigma}_1}{X_c}\right)^2, & \text{if } \hat{\sigma}_1 < 0 \end{cases} \tag{2.6}$$

X_t and X_c represent the fiber tensile and compressive strengths, whereas S_L is the longitudinal shear strength. In the same manner, matrix F_m and interlaminar F_i failure criteria are defined as:

$$F_m = \begin{cases} F_{mt} = \left(\frac{\hat{\sigma}_2+\hat{\sigma}_3}{Y_t}\right)^2 + \frac{\hat{\tau}_{23}^2-\hat{\sigma}_2\hat{\sigma}_3}{S_I^2} + \frac{\hat{\tau}_{21}^2+\hat{\tau}_{31}^2}{S_L^2}, & \text{if } \hat{\sigma}_2+\hat{\sigma}_3 \geq 0 \\ F_{mc} = \left[\left(\frac{Y_c}{2S_T}\right)^2 - 1\right]\left(\frac{\hat{\sigma}_2+\hat{\sigma}_3}{Y_c}\right) + \left(\frac{\hat{\sigma}_2+\hat{\sigma}_3}{2S_T}\right)^2 + \frac{\hat{\tau}_{23}^2-\hat{\sigma}_2\hat{\sigma}_3}{S_I^2} + \frac{\hat{\tau}_{21}^2+\hat{\tau}_{31}^2}{S_L^2}, & \text{if } \hat{\sigma}_2+\hat{\sigma}_3 < 0 \end{cases} \tag{2.7}$$

$$F_i = \begin{cases} F_{it} = \left(\frac{\hat{\sigma}_3}{Z_t}\right)^2 + \left(\frac{\hat{\tau}_{31}}{S_L}\right)^2 + \left(\frac{\hat{\tau}_{31}}{S_I}\right)^2, & \text{if } \hat{\sigma}_3 \geq 0 \\ F_{ic} = \left(\frac{\hat{\sigma}_3}{Z_c}\right)^2, & \text{if } \hat{\sigma}_3 < 0 \end{cases} \tag{2.8}$$

Y_t and Y_c are the matrix tensile and compressive strengths, Z_t and Z_c are the interlaminar tensile and compressive strengths, whereas S_T and S_I indicate the transversal and interlaminar shear strengths. According to [107], the computation of equivalent stress and strain can be obtained as:

$$\sigma_{eq}\varepsilon_{eq} = \sum \sigma_{ij}\varepsilon_{ij}, \quad \text{with} \quad \varepsilon_{eq} = \sqrt{\sum \varepsilon_{ij}^2}, \qquad i,j = 1,2,..,6 \tag{2.9}$$

ε_{eq} and σ_{eq} are the equivalent strain and stress consistent with [109],

$$\begin{cases} \varepsilon_{eq,ft} = \sqrt{\langle\varepsilon_1\rangle^2 + \gamma_{12}^2 + \gamma_{13}^2} \\ \varepsilon_{eq,fc} = \langle -\varepsilon_1 \rangle \\ \varepsilon_{eq,mt} = \sqrt{\langle\varepsilon_2\rangle^2 + \langle\varepsilon_3\rangle^2 + \gamma_{21}^2 + \gamma_{23}^2 + \gamma_{31}^2} \\ \varepsilon_{eq,mc} = \sqrt{\langle -\varepsilon_2\rangle^2 + \langle -\varepsilon_3\rangle^2 + \gamma_{21}^2 + \gamma_{23}^2 + \gamma_{31}^2} \\ \varepsilon_{eq,it} = \sqrt{\langle\varepsilon_3\rangle^2 + \gamma_{31}^2 + \gamma_{32}^2} \\ \varepsilon_{eq,ic} = \langle -\varepsilon_3 \rangle \end{cases} \tag{2.10}$$

$$\begin{cases} \sigma_{eq,ft} = \frac{\langle\sigma_1\rangle\langle\varepsilon_1\rangle+\tau_{12}\gamma_{12}+\tau_{13}\gamma_{13}}{\sqrt{\langle\varepsilon_1\rangle^2+\gamma_{12}^2+\gamma_{13}^2}} \\ \sigma_{eq,fc} = \langle-\sigma_1\rangle \\ \sigma_{eq,mt} = \frac{\langle\sigma_2\rangle\langle\varepsilon_2\rangle+\langle\sigma_3\rangle\langle\varepsilon_3\rangle+\tau_{21}\gamma_{21}+\tau_{23}\gamma_{23}+\tau_{31}\gamma_{31}}{\sqrt{\langle\varepsilon_2\rangle^2+\langle\varepsilon_3\rangle^2+\gamma_{21}^2+\gamma_{23}^2+\gamma_{31}^2}} \\ \sigma_{eq,mc} = \frac{\langle-\sigma_2\rangle\langle-\varepsilon_2\rangle+\langle-\sigma_3\rangle\langle-\varepsilon_3\rangle+\tau_{21}\gamma_{21}+\tau_{23}\gamma_{23}+\tau_{31}\gamma_{31}}{\sqrt{\langle-\varepsilon_2\rangle^2+\langle-\varepsilon_3\rangle^2+\gamma_{21}^2+\gamma_{23}^2+\gamma_{31}^2}} \\ \sigma_{eq,it} = \frac{\langle\sigma_3\rangle\langle\varepsilon_3\rangle+\tau_{31}\gamma_{31}+\tau_{32}\gamma_{32}}{\sqrt{\langle\varepsilon_3\rangle^2+\gamma_{31}^2+\gamma_{32}^2}} \\ \sigma_{eq,ic} = \langle-\sigma_3\rangle \end{cases} \tag{2.11}$$

where $\langle\cdot\rangle$ denotes the Macaulay bracket. Upon solving the failure criteria expressed in Equations 2.6, 2.7, and 2.8, the initial values of equivalent stress (σ_{eq}^0) and strain (ε_{eq}^0) are determined. The computation of equivalent stress and strain at the onset of damage is necessary to establish the constitutive evolution law. In this study, the damage progression follows a linear softening path, and the following equation defines the damage (d) in the post-peak region:

$$d = \begin{cases} \frac{\delta_{eq}^u\left(\delta_{eq}-\delta_{eq}^0\right)}{\delta_{eq}\left(\delta_{eq}^u-\delta_{eq}^0\right)}, & \text{if } \delta_{eq}^0 \leq \delta_{eq} \leq \delta_{eq}^u \\ 1, & \text{if } \delta_{eq} > \delta_{eq}^u \end{cases} \tag{2.12}$$

where δ_{eq} is the equivalent displacement, and δ_{eq}^u is considered as the equivalent displacement when the damage $d = 1$.

$$\delta_{eq} = L_c\varepsilon_{eq} \quad \text{and} \quad \delta_{eq}^u = \frac{2G_a}{\sigma_{eq}} \tag{2.13}$$

L_c denotes the characteristic length [110], utilized to mitigate mesh dependency. In this study, L_c is defined as $(VGP)^{\frac{1}{3}}$, where VGP represents the Gauss point volume of the respective element, as previously implemented in [111]. However, various methods can be employed to define the characteristic length, as demonstrated in [112]. G_a denotes the fracture energy of the individual damage mode a, corresponding to the area $A\hat{B}C \Rightarrow \left(\varepsilon_{eq}\left(d=0\right)\right)$ beneath the curve of the linear evolution law (refer to Fig. 2.2).

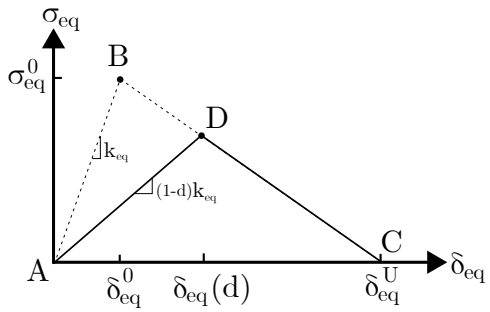

Fig. 2.2 Constitutive relation for the equivalent stress and displacement.

Chapter 3

Peridynamic theory

The damage model presented in Chapter 2 is based on continuum damage mechanics. This approach does not permit an explicit geometrical representation of cracks within the structure. An alternative is given by adopting discrete modelling techniques, which can describe the crack propagation within the structure. Nevertheless, external failure criteria are still needed. In this context, recognizing the limitations of the current methods of approximating the mathematical forms of the classical continuum mechanics, Silling [15] for the first time proposed a non-local formulation called Peridynamics (PD). The PD theory does not suffer from the inapplicability of the classical continuum mechanics theory when cracks or interfaces happen due to the integro-differential nature of the governing equations. Thus, PD presents a unique capability of analyzing damage and progressive failure of materials and structures by directly predicting the displacements, crack nucleation and propagation with arbitrary paths without any special numerical techniques or criteria. This chapter presents the continuum formulation and the meshless discretization of the more general state-based PD formulation. Then, the implementation of a progressive failure algorithm within the PD framework is described.

3.1 State-based Peridynamics

The initial formulation of the peridynamic theory, named bond-based Peridynamics [15], has been extensively used in recent years. The assumption of this formulation leads to a Poisson's ratio value constrained to $\nu = 0.25$ in 3D bodies. To

overcome this limitation, the state-based formulation of the theory was introduced in [113]. Both formulations have been adopted in this work. The governing equations of the state-based peridynamics will be shown in the following sections, being the bond-based formulation a particular case.

3.1.1 Continuum formulation

Two peridynamic points, for instance $\mathbf{x}$ and $\mathbf{x}'$ shown in Fig. 3.1, interact through a bond that is identified by their relative position vector

$$\boldsymbol{\xi} = \mathbf{x}' - \mathbf{x}\,. \tag{3.1}$$

This interaction vanishes when the distance between the interacting points surpasses a threshold value known as the horizon size, denoted by δ. As a result, within a 3D peridynamic framework, a point interacts with all other points located within a sphere centered around it, with a radius equal to δ. This collection of points within the sphere is referred to as the neighborhood and is represented by $\mathscr{H}$. In the deformed configuration, the relative displacement vector η is defined as follows:

$$\boldsymbol{\eta} = \mathbf{u}(\mathbf{x}',t) - \mathbf{u}(\mathbf{x},t)\,, \tag{3.2}$$

where $\mathbf{u}$ represents the displacement field. t's important to note that at time t, the relative position vector between points $\mathbf{x}$ and $\mathbf{x}'$ is expressed as $\boldsymbol{\xi} + \boldsymbol{\eta}$. The peridynamic equation of motion of point $\mathbf{x}$ is written as [113]

$$\rho(\mathbf{x})\,\ddot{\mathbf{u}}(\mathbf{x},t) = \int_{\mathscr{H}_\mathbf{x}} \left(\underline{\mathrm{T}}[\mathbf{x},t]\langle\boldsymbol{\xi}\rangle - \underline{\mathrm{T}}[\mathbf{x}',t]\langle-\boldsymbol{\xi}\rangle\right) \mathrm{d}V_{\mathbf{x}'} + \mathbf{b}(\mathbf{x},t)\,, \tag{3.3}$$

where ρ represents the material density, $\ddot{\mathbf{u}}$ the acceleration field, $\underline{\mathrm{T}}$ the force density vector state (force per unit volume squared), $\mathrm{d}V_{\mathbf{x}'}$ the differential volume of a point $\mathbf{x}'$ within the neighbourhood $\mathscr{H}_\mathbf{x}$ and $\mathbf{b}$ the external body force density field. The notation $\underline{\mathrm{T}}[\mathbf{x},t]\langle\xi\rangle$ implies that the force density scalar state $\underline{\mathrm{T}}$ depends on the point $\mathbf{x}$ and instant t, and is applied to the bond vector $\boldsymbol{\xi}$. In quasi-static conditions, the equilibrium equation for point $\mathbf{x}$ can be expressed as:s

$$-\int_{\mathscr{H}_\mathbf{x}} \left(\underline{\mathrm{T}}[\mathbf{x}]\langle\xi\rangle - \underline{\mathrm{T}}[\mathbf{x}']\langle-\xi\rangle\right) \mathrm{d}V_{\mathbf{x}'} = \mathbf{b}(\mathbf{x})\,. \tag{3.4}$$

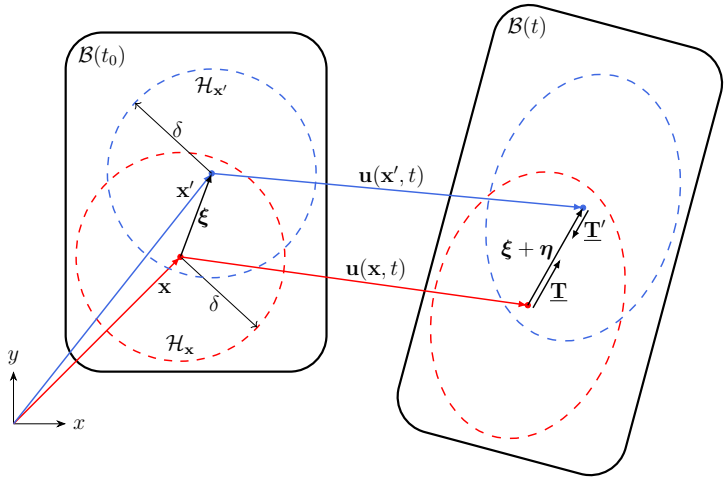

Fig. 3.1 Reference configuration of the body $\mathscr{B}$ at time t_0 (on the left) and deformed configuration at time t (on the right). When the bond ξ between the point $\mathbf{x}$ and $\mathbf{x}'$ is deformed, the force density vector states $\underline{\mathbf{T}} = \underline{\mathbf{T}}[\mathbf{x},t]\langle\xi\rangle$ and $\underline{\mathbf{T}}' = \underline{\mathbf{T}}[\mathbf{x}',t]\langle-\xi\rangle$ are created within the bond.

It's important to note that in bond-based Peridynamics, $\underline{\mathbf{T}}[\mathbf{x}]\langle\boldsymbol{\xi}\rangle$ and $\underline{\mathbf{T}}[\mathbf{x}']\langle-\xi\rangle$ must have identical magnitudes, while in state-based Peridynamics, they may have different magnitudes (see Fig. 3.1). Let us introduce some quantities that will aid in computing the force density vector state $\underline{\mathbf{T}}[\mathbf{x}]\langle\boldsymbol{\xi}\rangle$. The reference position scalar state $\underline{x}$, which signifies the bond length in the initial configuration, and the extension scalar state $\underline{e}$, representing the elongation (or contraction) of the bond in the deformed configuration, are defined as:

$$\underline{x}\langle\boldsymbol{\xi}\rangle = \|\boldsymbol{\xi}\|\,. \tag{3.5}$$

$$\underline{e}\langle\boldsymbol{\xi}\rangle = \|\boldsymbol{\xi}+\boldsymbol{\eta}\| - \|\boldsymbol{\xi}\|\,. \tag{3.6}$$

On the other hand, the weighted volume m and the dilatation θ of a point $\mathbf{x}$ are defined respectively as

$$m(\mathbf{x}) = \int_{\mathscr{H}_{\mathbf{x}}} \underline{\omega}\,\underline{x}^2\,\mathrm{d}V_{\mathbf{x}'}\,, \tag{3.7}$$

$$\theta(\mathbf{x}) = \frac{3}{m(\mathbf{x})}\int_{\mathscr{H}_{\mathbf{x}}} \underline{\omega}\,\underline{x}\,\underline{e}\,\mathrm{d}V_{\mathbf{x}'}\,, \tag{3.8}$$

where $\underline{\omega}$ is a prescribed spherical influence function. We adopt in this work the Gaussian influence function:

$$\underline{\omega} = \exp\left(-\frac{\|\boldsymbol{\xi}\|^2}{\delta^2}\right). \tag{3.9}$$

In ordinary state-based peridynamics, the force density vector state is aligned with the deformed direction vector state (unit vector in the direction of the corresponding bond):

$$\underline{\mathrm{M}}\langle\boldsymbol{\xi}\rangle = \frac{\boldsymbol{\xi}+\boldsymbol{\eta}}{\|\boldsymbol{\xi}+\boldsymbol{\eta}\|}\,. \tag{3.10}$$

Therefore, adopting the linear peridynamic solid model [113], the force density vector state is computed as

$$\underline{\mathrm{T}}[\mathbf{x}]\langle\boldsymbol{\xi}\rangle = \frac{\underline{\omega}\langle\boldsymbol{\xi}\rangle}{m(\mathbf{x})}\left[\,(3K-5\mu)\,\theta(\mathbf{x})\,\underline{x}\langle\boldsymbol{\xi}\rangle + 15\mu\,\underline{e}\langle\boldsymbol{\xi}\rangle\right]\underline{\mathrm{M}}\langle\boldsymbol{\xi}\rangle\,, \tag{3.11}$$

where K is the bulk modulus and μ is the shear modulus.

3.1.2 Discretization

The peridynamic body is discretized using the meshfree method with a uniform grid spacing h, which is widely employed in literature [21, 114, 115]. Each node represents a cell with a volume $V = h^3$. Consider a node i and its neighborhood $\mathscr{H}_i$, as depicted in Fig. 3.2. Here, β, referred to as the quadrature coefficient, denotes the volume cell fraction within $\mathscr{H}_i$. The quadrature coefficient β ranges between 0 (if the cell lies entirely within $\mathscr{H}_i$) and 1 (if the cell is completely outside $\mathscr{H}_i$). It's important to note that a node is considered part of the neighborhood only if the quadrature coefficient of its cell satisfies $\beta > 0$. The computation of quadrature coefficients in 3D Peridynamics can be performed in various ways (refer to, for instance,[115–117]). For simplicity, we adhere to the method outlined in [118] for the present study. The relative position vector of the bond ij that connects nodes i and j can be computed as

$$\boldsymbol{\xi}_{ij} = \mathbf{x}_j - \mathbf{x}_i\,, \tag{3.12}$$

where $\mathbf{x}_i$ and $\mathbf{x}_j$ are the position vectors of the two nodes. Similarly, the relative displacement vector of the bond is evaluated as

$$\boldsymbol{\eta}_{ij} = \mathbf{u}_j^{PD} - \mathbf{u}_i^{PD}\,, \tag{3.13}$$

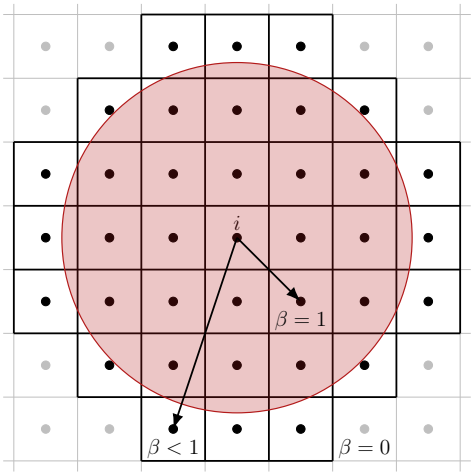

Fig. 3.2 The neighborhood $\mathscr{H}_i$ of a node i omprises nodes with $\beta > 0$, where β denotes the quadrature coefficient calculated as the fraction of the cell volume situated within the neighborhood.

where $\mathbf{u}_i^{PD}$ and $\mathbf{u}_j^{PD}$ are the displacement vectors of the peridynamic nodes. The reference position scalar state and the influence function of the bond are computed as

$$\underline{x}_{ij} = \|\boldsymbol{\xi}_{ij}\|\,, \tag{3.14}$$

$$\underline{\omega}_{ij} = \exp\left(-\frac{\|\boldsymbol{\xi}_{ij}\|^2}{\delta^2}\right). \tag{3.15}$$

Under the assumption of small displacements ($\|\boldsymbol{\eta}_{ij}\| \ll \|\boldsymbol{\xi}_{ij}\|$), the deformed direction vector state and the extension scalar state are respectively given as

$$\underline{\mathbf{M}}_{ij} = \frac{\boldsymbol{\xi}_{ij}+\boldsymbol{\eta}_{ij}}{\|\boldsymbol{\xi}_{ij}+\boldsymbol{\eta}_{ij}\|} \approx \frac{\boldsymbol{\xi}_{ij}}{\|\boldsymbol{\xi}_{ij}\|}\,. \tag{3.16}$$

$$\underline{e}_{ij} = \|\boldsymbol{\xi}_{ij}+\boldsymbol{\eta}_{ij}\| - \|\boldsymbol{\xi}_{ij}\| \approx \boldsymbol{\eta}_{ij}\cdot\underline{\mathbf{M}}_{ij}\,. \tag{3.17}$$

In the discretized model, the integrals over a neighborhood are numerically computed as the summation of the integrand evaluated for each node contained in that neighborhood. Therefore, the weighted volume m and the dilatation θ of a node i are given as

$$m_i = \sum_{j\in\mathscr{H}_i} \underline{\omega}_{ij}\,\underline{x}_{ij}^2\,\beta_{ij}V\,, \tag{3.18}$$

$$\theta_i = \frac{3}{m_i} \sum_{j \in \mathscr{H}_i} \underline{\omega}_{ij} \underline{x}_{ij} \underline{e}_{ij} \beta_{ij} V \,, \tag{3.19}$$

where β_{ij} is the quadrature coefficient of the bond ij and V is the volume of the cell of node j. Therefore, the force density vector state is computed as

$$\underline{\mathrm{T}}_{ij} = \frac{\underline{\omega}_{ij}}{m_i} \left[(3K - 5\mu)\, \theta_i \underline{x}_{ij} + 15\mu\, \underline{e}_{ij} \right] \underline{\mathrm{M}}_{ij} \,. \tag{3.20}$$

Now, we can write the equilibrium equation of a node i in the discretized form (multiplying both sides of the equation by the cell volume $V_i = V$) as follows:

$$-\sum_{j \in \mathscr{H}_i} \left(\underline{\mathrm{T}}_{ij} - \underline{\mathrm{T}}_{ji} \right) \beta_{ij} V^2 = \mathbf{b}_i V \,, \tag{3.21}$$

where $\mathbf{b}_i$ is the external force density vector applied to node i. Equation 3.21 can be rewritten in the standard form

$$\mathbf{K}^{PD} \mathbf{U}^{PD} = \mathbf{F}^{PD} \,, \tag{3.22}$$

where $\mathbf{K}^{PD}$ is the peridynamic stiffness matrix, $\mathbf{U}^{PD}$ is the peridynamic displacement vector and $\mathbf{F}^{PD}$ is the peridynamic force vector.

3.2 Progressive failure analysis

In the framework of peridynamics, material damage can be directly incorporated into the constitutive model by allowing bonds between particles to break. In this study, we have adopted a bond-based peridynamic formulation with progressive failure. As mentioned earlier, the bond-based formulation is a specific instance of the more general state-based formulation. The former says that the force exerted through the bond can be uniquely characterized by the relative initial and current position vectors between the two points defining the bond; no additional information from their surrounding points or bonds is necessary. However, this assumption gives rise to certain inherent limitations, such as a fixed value of Poisson's ratio, which is $\nu = 0.25$ when dealing with 3D problems. With these assumptions, the equilibrium

equation for a particle in discretized form (see Eq. 3.21) can be expressed as follows:

$$-\sum_{j\in\mathscr{H}_i^0} \mathbf{T}_{ij}\,\beta_{ij}V^2 = \mathbf{b}_i V \tag{3.23}$$

Various failure criteria have been explored in the literature within the peridynamic framework (e.g., [119–121]). A concise overview is provided in [122]. In the context of bond-based peridynamics, the most commonly utilized failure criterion is the bond stretch criterion, initially proposed by Silling and Askari in [123]. According to this criterion, a bond is deemed to have failed when it experiences a stretch exceeding its critical value s_c. Upon failure, the pairwise force between the implicated points is irreversibly eliminated. Consequently, the load is redistributed among all other bonds, potentially resulting in unguided crack initiation. To nullify the pairwise force between two points, a history-dependent scalar function μ must be introduced::

$$\mu(\boldsymbol{\eta},\boldsymbol{\xi}) = \begin{cases} 1, & s < s_c \\ 0, & s \geq s_c \end{cases} \tag{3.24}$$

A distinct scalar μ is assigned to each pair of particles within the horizon radius δ. Subsequently, this scalar is incorporated into the reformulated version of Eq. (3.20). Thus, when the critical stretch between two particles is attained, the corresponding scalar function μ will be set to 0, resulting in the removal of the pairwise force $\mathbf{T}$. The critical stretch is assumed to be uniform throughout the material. Its determination has been addressed through energetic considerations in [123]. Specifically, the critical stretch value is derived by equating the energy required to fracture all the bonds connecting two halves of a fracture surface with the critical energy release rate G_0. Assuming Linear Elastic Fracture Mechanics (LEFM) for an isotropic material and a 3D peridynamics grid, the critical stretch value s_c is given by:

$$s_c = \sqrt{\frac{5G_0}{6E\delta}} \tag{3.25}$$

The advantage of introducing failure directly at a bond level is the possibility of a unique identification of local damage, defined by the scalar function φ_x

$$\varphi_x = 1 - \frac{\int_{H_x} \mu(\boldsymbol{\eta},\boldsymbol{\xi})\,dV_{x'}}{\int_{H_x} dV_{x'}} \tag{3.26}$$

called damage index. The subscript x denotes that the damage index is associated with the individual particle x. The function φ_x can range from 0 to 1, representing the degree of damage experienced by the particle. A value of 0 signifies an intact bond, whereas a value of 1 indicates that all bonds connected to the source point are broken, resulting in its detachment from the structure. An illustrative example of φ_x calculation for a single particle x (depicted in red in the figure) is depicted in Fig. 3.3. It is assumed that a crack initiates when $\varphi_x \geq 0.5$.

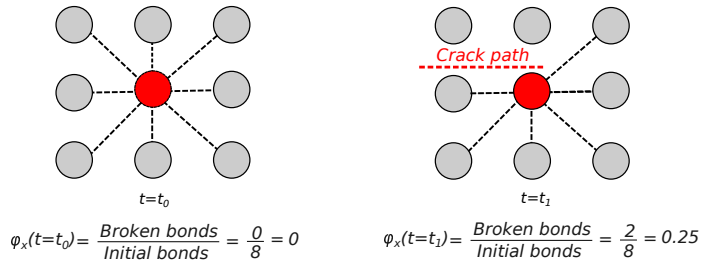

Fig. 3.3 An illustration depicting the computation of the damage index φ for a single point (highlighted in red) is provided. Only interactions involving this point are shown for clarity.

In this study, a series of sequentially quasi-static linear analyses are conducted, where an increasing displacement is applied at each step. Following the solution of the linear problem, the bond stretch s value is computed for each pair (i,j) of particles within the horizon radius δ. Subsequently, this stretch is compared with the critical bond stretch s_c, determined using Eq.(3.25). If $s(i,j)$ exceeds s_c for one or more bonds, the pairwise force exchanged between the involved points is nullified by setting the scalar $\mu(i,j)$ value to 0. Furthermore, the damage index φ_x is computed for each particle x to visualize crack initiation and propagation. Any broken bonds are subsequently removed in the following iteration. A flowchart depicting the entire algorithm introduced by Ni et al. in [124] is shown in Fig.3.4. However, it's important to note that the algorithm used in this study does not include a convergence check based on the number of broken bonds per iteration. Therefore, it necessitates an appropriate choice of applied displacement for each iteration.

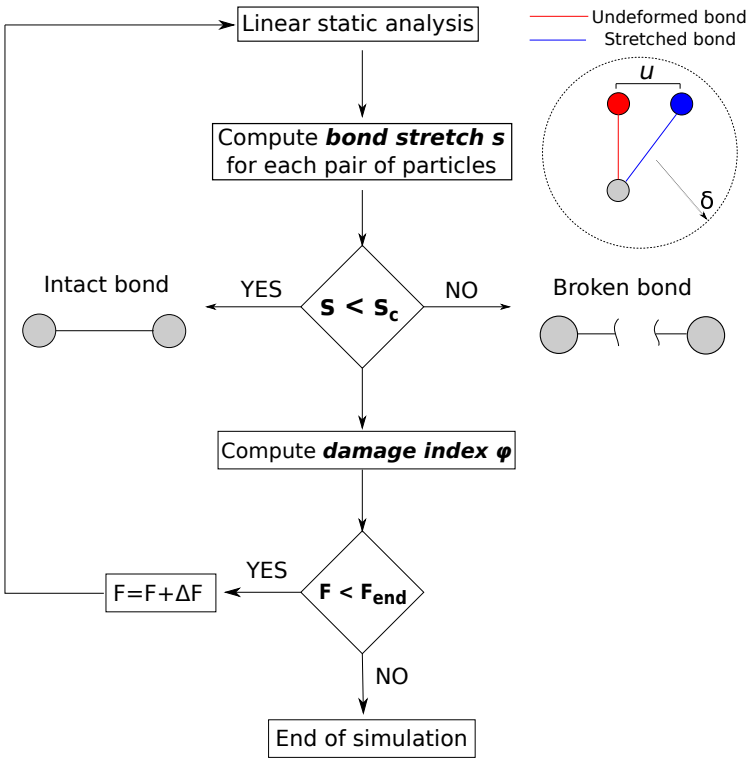

Fig. 3.4 Flowchart representing the failure algorithm.

Chapter 4

Derivation of high order 1D and 2D models

This chapter presents the Carrera Unified Formulation (CUF) and its application in the straightforward development of 1D (beam) and 2D (plate) higher-order models within a finite element framework in a hierarchical and automated way. Essentially, CUF employs an index notation to unify all structural theories into a single formula and facilitate the formulation of refined models in a simplified manner. The fundamental concept of this framework involves the incorporation of expansion functions, alongside standard finite element interpolation functions, to enhance the kinematic description of beam cross-sections and plate/shell thicknesses. This approach results in 1D and 2D CUF models that offer solution accuracy comparable to 3D solid finite element analysis (FEA) but with significantly reduced computational requirements [39].

The chapter begins by defining the notation, geometry, displacement, stress, and strain vectors. Subsequently, it presents the geometrical and material relations, as well as the governing equations, including the explicit form of the associated matrices. While some details have been omitted for brevity, interested readers can refer to [125, 126] for further information.

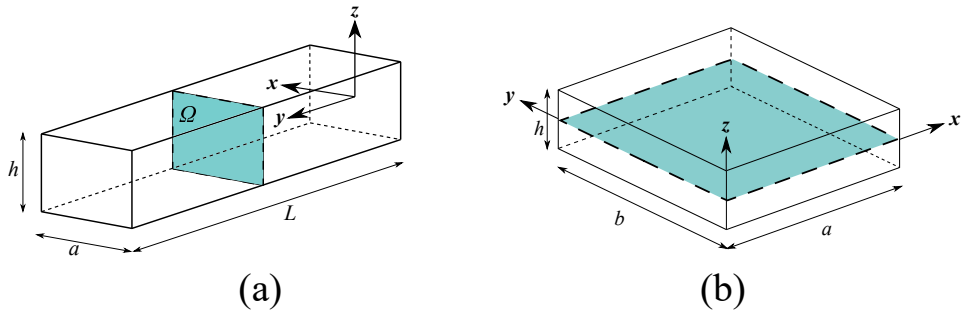

Fig. 4.1 Representative geometry and reference system for a) beam and b) plate models.

4.1 Preliminaries

Consider beam and plate models described by adopting a Cartesian reference system (x,y,z), as illustrated in Fig. 4.1. For a beam, the y-direction refers to the beam axis, whereas for a plate model the $x-y$ directions indicates the two in-plane directions, with z representing the through-the-thickness direction. The cross-section shape or thickness does not affect the following formulation, thus allowing an arbitrary choice.

Let us consider a 3D displacement vector for a generic point within the structural domain. This quantity may be expressed as follows:

$$\mathbf{u}(x,y,z)^k = \{u_x^k \;\; u_y^k \;\; u_z^k\}^T \tag{4.1}$$

where the superscript k is the k-th layer if a laminated structure is considered and T is the transpose operator. Note that the dynamic effects are not taken into account in this discussion, i.e. the time dependency is neglected. The stress σ and strain ε vectorial form is expressed as follows:

$$\begin{aligned} \boldsymbol{\varepsilon}^k &= \{\varepsilon_{xx}^k \;\; \varepsilon_{yy}^k \;\; \varepsilon_{zz}^k \;\; \varepsilon_{xz}^k \;\; \varepsilon_{yz}^k \;\; \varepsilon_{xy}^k\}^T \\ \boldsymbol{\sigma}^k &= \{\sigma_{xx}^k \;\; \sigma_{yy}^k \;\; \sigma_{zz}^k \;\; \sigma_{xz}^k \;\; \sigma_{yz}^k \;\; \sigma_{xy}^k\}^T \end{aligned} \tag{4.2}$$

Assuming small displacements and rotations, the strain-displacement relations are

$$\boldsymbol{\varepsilon} = \mathbf{B}\mathbf{u} \tag{4.3}$$

where **B** is the linear differential operator matrix that follows:

$$\begin{bmatrix} \frac{\partial}{\partial x} & 0 & 0 \\ 0 & \frac{\partial}{\partial y} & 0 \\ 0 & 0 & \frac{\partial}{\partial z} \\ \frac{\partial}{\partial x} & 0 & \frac{\partial}{\partial z} \\ 0 & \frac{\partial}{\partial y} & \frac{\partial}{\partial z} \\ \frac{\partial}{\partial x} & \frac{\partial}{\partial y} & 0 \end{bmatrix} \tag{4.4}$$

The relations between stress and strain are given by the Hooke's law, which states:

$$\boldsymbol{\sigma}^k = \mathbf{C}^k \boldsymbol{\varepsilon}^k \tag{4.5}$$

in which $\mathbf{C}^k$ is the 6×6 stiffness matrix of the material. In case of material nonlinearities, the material model provides the matrix $\mathbf{C}^k$ based on the system current state. Let us consider an orthotropic material, which has two planes of symmetry where the properties do not vary. In this case, the stiffness material matrix is written as:

$$\mathbf{C}^k = \begin{bmatrix} C_{11}^k & C_{12}^k & C_{13}^k & 0 & 0 & \\ & C_{22}^k & C_{23}^k & 0 & 0 & \\ & & C_{33}^k & 0 & 0 & \\ & & & C_{44}^k & C_{45}^k & 0 \\ & & & & C_{55}^k & 0 \\ sym & & & & & C_{66}^k \end{bmatrix} \tag{4.6}$$

The coefficients of the $\mathbf{C}^k$ matrix in Eq. 4.6 can be written in terms of 9 independent constants, given in the form of the engineering moduli: Young's moduli E_1, E_2, E_3; shear moduli G_{12}, G_{13}, G_{23}; and Poisson ratios ν_{12}, ν_{13}, ν_{23}. These quantities are expressed as follows:

$$E_i = \frac{\sigma_i}{\varepsilon_i}, \quad G_{ij} = \frac{\sigma_{ij}}{\varepsilon_{ij}}, \quad \nu_{ij} = -\frac{\varepsilon_j}{\varepsilon_i} \tag{4.7}$$

In the material reference system, the stiffness material matrix can be written as follows:

$$\boldsymbol{\sigma}^k = \widetilde{\mathbf{C}}^k \boldsymbol{\varepsilon}^k \tag{4.8}$$

where:

$$\widetilde{\mathbf{C}}^k = \mathbf{T}^{\mathrm{T}} \mathbf{C}^k \mathbf{T} \tag{4.9}$$

where $\mathbf{T}$ is the rotation matrix [65].

4.2 Carrera Unified Formulation

For decades, the scientific community has shown keen interest in introducing advanced models capable of addressing various structural challenges, particularly in the analysis of composite structures. In response to certain limitations of classical theories, Carrera introduced the Carrera Unified Formulation (CUF) as a means of generating structural theories for plates [127], subsequently extending it to 1D formulations [128]. According to CUF, the 3D displacement field of a structure can be expressed as:

$$\begin{aligned} &\textit{Beam}: \quad \mathbf{u}^k(x,y,z) = F_\tau^k(x,z)\mathbf{u}_\tau^k(y), \qquad \tau = 1,\ldots,M \\ &\textit{Plate}: \quad \mathbf{u}^k(x,y,z) = F_\tau^k(z)\mathbf{u}_\tau^k(x,y), \qquad \tau = 1,\ldots,M \end{aligned} \tag{4.10}$$

which indicates a generic expansion of the displacement unknowns over the cross-section and through-the-thickness for beam and plate models, respectively. The term F_τ in Eq. 4.10 indicates the set of expansion functions, $\mathbf{u}_\tau$ represents the generalized displacement vector, M the order of the expansion and the repeated index τ stands for summation. The choice of both parameters F_τ and M is arbitrary and provided by the user as input to define the structural theory to be adopted in the model. In the last years, different theories have been implemented within the CUF framework. Thanks to their capabilities, polynomial expression have been mostly used in CUF-based analyses.

4.2.1 Taylor expansion

Taylor expansions (TE) consider the Taylor series of the type $x-z$ as cross sectional or z as thickness expansion function F_τ for beam and plate models, respectively. As an example, the second-order Taylor expansion (TE2) for 1D and 2D models is here reported:

$$\begin{aligned}
&& u_x &= u_{x_1} + xu_{x_2} + zu_{x_3} + x^2u_{x_4} + xzu_{x_5} + z^2u_{x_6} \\
\text{1D}: && u_y &= u_{y_1} + xu_{y_2} + zu_{y_3} + x^2u_{y_4} + xzu_{y_5} + z^2u_{y_6} \\
&& u_z &= u_{z_1} + xu_{z_2} + zu_{z_3} + x^2u_{z_4} + xzu_{z_5} + z^2u_{z_6} \\
\\
&& u_x &= u_{x_1} + zu_{x_2} + z^2u_{x_2} \\
\text{2D}: && u_y &= u_{y_1} + zu_{y_2} + z^2u_{y_2} \\
&& u_z &= u_{z_1} + zu_{z_2} + z^2u_{z_2}
\end{aligned} \tag{4.11}$$

Note that the TE kinematics is hierarchial, meaning that the polynomial order of the transverse approximations is refined just by addition of higher-order functions. Thus, Eq. 4.11 takes into account constant, linear and quadratic terms. Moreover, it should be highlighted that classical theory can be retrieved just by truncation of the TE kinematic field. For instance, by consider only the expansion of five unknowns $(u_{x_1}, u_{y_1}, u_{z_1}, u_{y_2}, u_{y_3})$ in the case of 1D model, one will directly obtain from Eq.4.11 the Timoshenko Beam Theory (TBT) [129]. Further information about TE models can be found in [130, 131].

4.2.2 Lagrange expansion

Lagrange expansion (LE) class adopts Lagrange polynomials to generate 1D and 2D higher-order models. The isoparametric formulation is exploited in order to deal with any arbitrary shaped geometry. LE are used as F_τ functions over the cross-section for 1D model and thickness direction for 2D models. For the activities carried out in this research, three types of polynomials have been adopted for both 1D and 2D models, see Fig. 4.2. More specifically, four-point polynomials (L4), nine-point polynomials (L9), and sixteen-point polynomials (L16) were employed to build linear to cubic kinematics beam models. Conversely, the abbreviation LDN (Lagrange expansion, Displacement-based theory with order N) will be employed to denote particular refined plates. For instance, LD1, LD2, and LD3 represent linear (two-node), quadratic (three-node), and cubic (four-node) Lagrange expansion

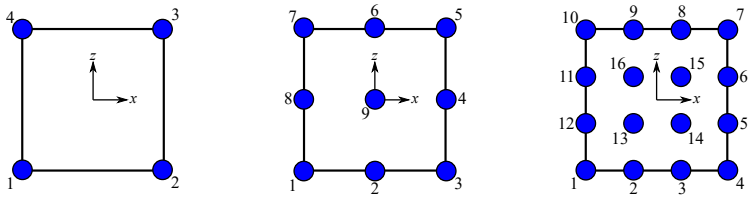

(a) 1D

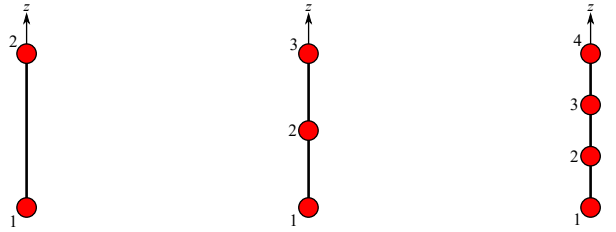

(a) 2D

Fig. 4.2 Lagrange expansion function for a) 1D and b) 2D models.

functions, respectively. These functions are utilized in the z-direction to construct linear to higher-order kinematics CUF 2D models. To elucidate, an illustration of interpolation functions is provided below for an L9 beam model:

$$\begin{aligned} F_\tau &= \tfrac{1}{4}(r^2+rr_\tau)(s^2+ss_\tau) && \tau = 1,3,5,7 \\ F_\tau &= \tfrac{1}{2}s_\tau^2(s^2-ss_\tau)(1-r^2)+\tfrac{1}{2}r_\tau^2(r^2-rr_\tau)(1-s^2) && \tau = 2,4,6,8 \\ F_\tau &= (1-r^2)(1-s^2) && \tau = 9 \end{aligned} \tag{4.12}$$

in which r and s vary from -1 to +1, while r_τ and s_τ are the coordinates of the 9 points whose numbering and location in the natural coordinate frame are depicted in Fig. 4.2. Consequently, the displacement field of an L9 beam theory will be:

$$\begin{aligned} u_x &= F_1\, u_{x_1} + F_2\, u_{x_2} + \ldots + F_9\, u_{x_9} \\ u_y &= F_1\, u_{y_1} + F_2\, u_{y_2} + \ldots + F_9\, u_{y_9} \\ u_z &= F_1\, u_{z_1} + F_2\, u_{z_2} + \ldots + F_9\, u_{z_9} \end{aligned} \tag{4.13}$$

where $u_{x_1},\ldots,u_{z_9}$ are the displacement variables of the problem and they represent the translational displacement components of each of the nine centres of the L9 polyno-

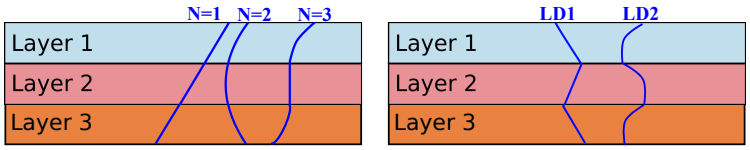

(a) **ESL** (b) **LW**

Fig. 4.3 (a) ESL and (b) LW behaviours of the primary variables through-the-thickness of a 2D model.

mial. TE models made use of degrees of freedom which include both displacements and N-order derivative of displacements. In contrast, LE models use only displacement unknowns; i.e., the only kind of degree of freedom is the displacement. This allows the imposition of displacement continuity among components of the same structure in a natural manner, without adopting any mathematical artifice. Furthermore, the LE formulation has been exploited to build a so-called Component-Wise (CW) method [132, 133]. More details about this approach will be given in Part II.

The selection of the polynomial class dictates various approaches for analyzing laminated composite structures. Opting for Taylor-like (TE) class polynomials yields an Equivalent-Single-Layer (ESL) approach. In this approach, the cross-section is treated as a unified domain where cross-sectional functions F_τ are defined, and stresses are computed based on the resulting strains in each layer. Consequently, the stiffness matrix is obtained through homogenization techniques, aggregating the contributions from each layer. Due to the heterogeneous nature of multi-layered structures, ESL models exhibit continuous transverse deformations throughout the thickness and discontinuous transverse stresses at layer interfaces. Consequently, while ESL theories offer reliable results for global responses such as fundamental vibration frequencies and transverse deflections, they often fall short in accurately evaluating 3D stress distributions. For visual clarity, Fig. 4.3a illustrates the typical behavior of primary variables in the z-direction of a plate structure. In contrast, the use of LE class leads to Layer-Wise (LW) theories. According to LW approach, the displacement field within each material layer is separated and then expanded. Thus, ensuring the continuity of displacements at the interface level is crucial for accurately assessing deformation and stress distributions. Homogenization is consequently conducted at the interface layer. Through the utilization of LE, the displacements on each interpolation are treated as unknowns, with the displacements at each interface adhering to compatibility conditions, as depicted in Fig. 4.3b [65]. For a compre-

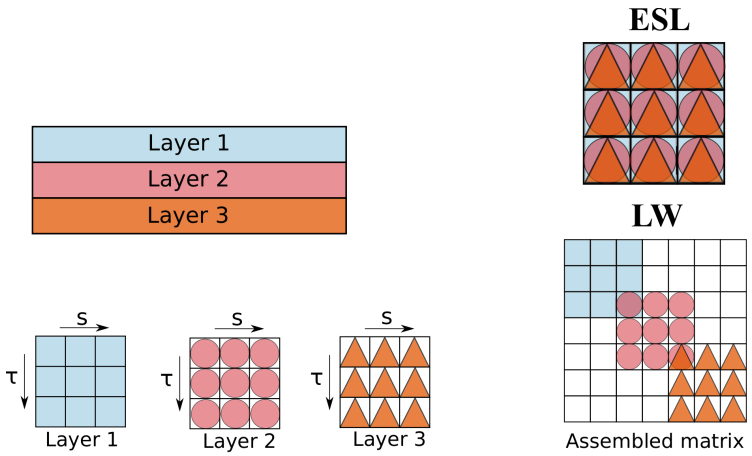

Fig. 4.4 The method of assembling the stiffness matrix for the 2D model using ESL and LW techniques is illustrated. Here, τ and s represent the two indices utilized for assembling the matrices.

hensive understanding, distinctions in the assembly procedure when employing ESL and LW for a 2D structure are depicted in Fig. 4.4.

4.3 The finite element method

Different methods have been employed to solve structural problems within the CUF framework, such as close-form Navier solutions [134] and dynamic stiffness method [135], among others. These models have the advantages of relatively low computational costs and the absence of convergence issues. However, analytical solution can generally deal with a certain range of boundary conditions and geometries, making them not suitable for a large number of structural problems. In recent years, a finite element formulation [125] has been adopted within the CUF framework to overcome these issues. The coupling of the CUF formulation with FEM allows to deal with arbitrary geometry, loadings and boundary conditions. Independently of the adopted beam and plate model kinematics, the FEM is used to discretize the generalized displacements vector $\mathbf{u}_\tau$ along the y-axis for the beam or in the $x-y$ plane for plate models as reported below:

$$\begin{aligned} &Beam: \quad \mathbf{u}^k_\tau(y) = N_i(y)\mathbf{q}^k_{\tau i}, && i = 1,\dots,N_n \\ &Plate: \quad \mathbf{u}^k_\tau(x,y) = N_i(x,y)\mathbf{q}^k_{\tau i}, && i = 1,\dots,N_n \end{aligned} \tag{4.14}$$

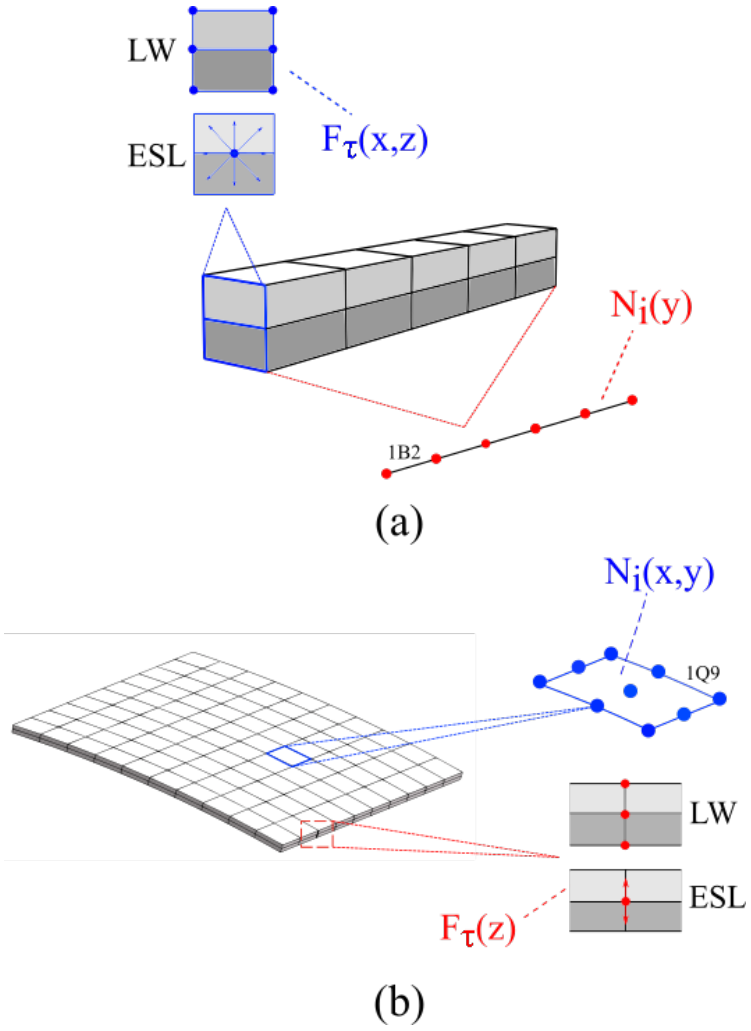

Fig. 4.5 CUF and FEM (a) 1D and (b) 2D model approximations.

where N_i are the shape functions, $\mathbf{q}_{\tau i}$ denotes the unknown nodal variables, N_n stands for the number of nodes per element and the i indicates summation. In this work, 1D beam elements with linear, quadratic and cubic approximation along the beam axis, i.e., two-node (B2), three-node (B3) and four-node (B4) are used. In contrast, classical 2D FEs with four-node bilinear (Q4), nine-node (Q9) and sixteen-node (Q16) are employed as shape functions in the $x-y$ plane. A graphical representation of CUF and FEM model approximation for both 1D and 2D models is illustrated in Fig. 4.5. Combining the FE approximation in Eq. 4.14 and CUF in Eq. 4.10, the 3D

displacement field becomes:

$$\begin{aligned} &Beam: \quad \mathbf{u}^k(x,y,z) = F_\tau^k(x,z)N_i(y)\mathbf{q}_\tau^k, \qquad \tau = 1,\ldots,M \qquad i = 1,\ldots,N_n \\ &Plate: \quad \mathbf{u}^k(x,y,z) = F_\tau^k(z)N_i(x,y)\mathbf{q}_\tau^k, \qquad \tau = 1,\ldots,M \qquad i = 1,\ldots,N_n \end{aligned} \tag{4.15}$$

The choice of the axial (1D model) or cross-sectional (2D model) shape functions N_i does not depend on the choice of the cross-sectional or thickness expansion function F_τ, respectively, thus allowing a significant flexibility in terms of structural modelling.

4.4 Derivation of the governing equations

The governing equations for the elasticity problem are derived using the Principle of Virtual Displacements (PVD). As per PVD, a body is in equilibrium if, for all kinematically admissible virtual displacements, the virtual work done by internal stresses and inertial loads equals the work done by external loads:

$$\delta L_{int} = \delta L_{ext} - \delta L_{ine} \tag{4.16}$$

where δL_{int}, δL_{ext} and δL_{ine} represent the virtual variation of the strain energy, the virtual variation of the work of external loads and the virtual variation of the inertia loads. The term related to the internal strain energy can be written as follows:

$$\delta L_{int} = \int_V \delta \boldsymbol{\varepsilon}^{k\mathrm{T}} \boldsymbol{\sigma}^k \, dV = \int_V \delta \varepsilon^{k\mathrm{T}} \widetilde{\mathbf{C}}^k \boldsymbol{\varepsilon}^k \, dV \tag{4.17}$$

where V is the volume of the body. The strain-displacement relation (Eq. 4.3) can be reformulated using Eq. 4.15, resulting in:

$$\boldsymbol{\varepsilon} = \mathbf{B}_{\tau i} \mathbf{q}_{\tau i} \tag{4.18}$$

with

$$\mathbf{B}_{\tau i} = \begin{bmatrix} N_i F_{\tau,x} & 0 & 0 \\ 0 & N_{i,y} F_\tau & 0 \\ 0 & 0 & N_i F_{\tau,z} \\ N_i F_{\tau,z} & 0 & N_i F_{\tau,x} \\ 0 & N_i F_{\tau,z} & N_{i,y} F_\tau \\ N_{i,y} F_\tau & N_i F_{\tau,x} & 0 \end{bmatrix} \tag{4.19}$$

The virtual variation of the strain tensor can then be expressed as:

$$\delta\boldsymbol{\varepsilon} = \mathbf{B}_{sj}\delta\mathbf{q}_{sj} \tag{4.20}$$

Thus, the virtual variation of the internal strain energy reads:

$$\delta L_{int} = \delta\mathbf{q}_{sj}^T \int_V \mathbf{B}_{sj^T} \widetilde{\mathbf{C}} \mathbf{B}_{\tau i} dV \mathbf{q}_{\tau i} = \delta\mathbf{q}_{sj}^T \mathbf{k}^{ij\tau s} \mathbf{q}_{\tau i} \tag{4.21}$$

where $\mathbf{k}^{ij\tau s}$ is a 3×3 matrix called Fundamental Nucleus (FN) of the structural stiffness matrix. For the sake of clarity, the $k_{ij\tau s}^{xx}$ component is reported below:

$$\begin{aligned} k_{xx}^{ij\tau s} = & \int_V \tilde{C}_{11} \frac{\partial}{\partial x}(N_j F_s) \frac{\partial}{\partial x}(N_i F_\tau) dV + \int_V \tilde{C}_{16} \frac{\partial}{\partial x}(N_j F_s) \frac{\partial}{\partial y}(N_i F_\tau) dV \\ & + \int_V \tilde{C}_{44} \frac{\partial}{\partial z}(N_j F_s) \frac{\partial}{\partial z}(N_i F_\tau) dV + \int_V \tilde{C}_{16} \frac{\partial}{\partial y}(N_j F_s) \frac{\partial}{\partial x}(N_i F_\tau) dV \\ & + \int_V \tilde{C}_{66} \frac{\partial}{\partial y}(N_j F_s) \frac{\partial}{\partial y}(N_i F_\tau) dV \end{aligned} \tag{4.22}$$

The remaining components of the FN can be retrieved in the same manner (see [136]). It should be noted that the formal expression of the FN remains invariable with respect to the structural theory or FE scheme chosen. Therefore, by simply looping on the indexes τ, i, j, s, any structural model can be created.

A similar procedure to the one used for the derivation of the virtual internal strain energy can be followed for the virtual variation of the internal loads, that is written as:

$$\delta L_{ine} = \delta\mathbf{q}_{sj}^T \int_V N_j F_s \rho \mathbf{I} N_i F_\tau dV \ddot{\mathbf{q}}_{\tau i} = \delta\mathbf{q}_{sj}^T \mathbf{m}^{ij\tau s} \ddot{\mathbf{q}}_{\tau i} \tag{4.23}$$

where $\mathbf{m}^{ij\tau s}$ is the fundamental nucleus of the mass matrix, whose components can be evaluated as those of the structural stiffness matrix.

The virtual variation of the work due to external loads is defined as:

$$\begin{aligned}\delta L_{ext} &= \int_V \delta\mathbf{u}^{\mathrm{T}}\mathbf{g}\, dV + \int_S \delta\mathbf{u}^{\mathrm{T}}\mathbf{b}\, dS + \int_l \delta\mathbf{u}^{\mathrm{T}}\mathbf{r}\, dl + \delta\mathbf{u}^{\mathrm{T}}P_m = \\ &= \delta\mathbf{q}_{sj}^{\mathrm{T}}\left(\int_V N_i F_\tau \mathbf{g}\, dV + \int_S N_i F_\tau \mathbf{b}\, dS + \int_l N_i F_\tau \mathbf{r}\, dl + N_i F_\tau P_m\right) = \\ &= \delta\mathbf{q}_{sj}^{\mathrm{T}}\mathbf{p}_{sj}\end{aligned} \tag{4.24}$$

Here, $\mathbf{g}$ represents the body force acting within the volume V, $\mathbf{b}$ signifies the surface force acting upon the surface S, $\mathbf{r}$ indicates the line force acting along a line l, and P_m denotes a point force exerted at point m. $\mathbf{p}_{sj}$ denotes the FN of the external equivalent nodal force vector. Following the assembly process, the global external nodal force vector $\mathbf{F}$ is acquired.

Upon substituting Eqs. 4.21, 4.23, and 4.24 into Eq. 4.16 and conducting straightforward mathematical manipulations, assuming undamped problems and a constant mass matrix, the governing equations for the elasticity problem are as follows:

$$\mathbf{M}\ddot{\mathbf{q}} + \mathbf{K}\mathbf{q} = \mathbf{F} \tag{4.25}$$

4.5 Physical nonlinear analysis and fracture

This work considers material non-linearities due to the presence of damage. The accurate numerical simulation of such behavior needs iterative resolution schemes. Approaches for the solution of nonlinear problems can be classified under two categories, namely implicit and explicit methods. This section provide a description of the implicit solution technique adopted within the CUF framework.

Using the notation introduced in previous sections, the compact form of Eq. (4.25) using CUF fundamental nuclei can be expressed as:

$$\mathbf{k}^{s}_{ij\tau s}\mathbf{u}_{\tau i} - \mathbf{p}_{sj} = 0 \tag{4.26}$$

where $\mathbf{k}^{s}_{ij\tau s}$ denotes the fundamental nuclei of secant stiffness matrix obtained using secant material matrix in (4.21). Therefore, the equilibrium equation, neglecting

dynamic forces, is given as

$$\mathbf{F}_{int}\left(\mathbf{u}\right) - \mathbf{F}_{ext} \tag{4.27}$$

where $\mathbf{F}_{int}\left(\mathbf{u}\right)$ is the internal force vector that depends on the displacement vector, and $\mathbf{F}_{ext}$ is the external force vector. The current work makes use of Newton-Raphson scheme for the implicit analysis of nonlinear problems. It involves the parametrization of the external load by a factor λ_n at a pseudo-time instant t_n. Consequently, Eq. 4.27 holds as follows:

$$\mathbf{F}_{int}\left(\mathbf{u}\right) - \lambda_n \mathbf{F}_{ext} = 0 \tag{4.28}$$

The implicit integration scheme uses an iterative process to find the converged solution $\boldsymbol{u}_{n+1}$, starting from the known solution $\boldsymbol{u}_n$. Considering the Taylor series expansion truncated at the linear term [125], the internal force $\mathbf{F}_{int}\left(\mathbf{u}_{n+1}\right)$ states:

$$\mathbf{F}_{int}\left(\mathbf{u}_{n+1}^{k+1}\right) = \mathbf{F}_{int}\left(\mathbf{u}_{n+1}^{k}\right) + \frac{\partial \mathbf{F}_{int}\left(\mathbf{u}_{n+1}^{k}\right)}{\partial \mathbf{u}_{n+1}^{k}} \Delta\mathbf{u}, \quad \Delta\mathbf{u} = \left(\mathbf{u}_{n+1}^{k+1} - \mathbf{u}_{n+1}^{k}\right) \tag{4.29}$$

where k is the iteration index for the load increment $[n, n+1]$, and Δu is the incremental displacement. Consequently, the tangent stiffness matrix $\mathbf{K}_T$ can be defined as follows:

$$\mathbf{K}_T = \frac{\partial \mathbf{F}_{int}\left(\boldsymbol{u}_{n+1}^{k}\right)}{\partial \boldsymbol{u}_{n+1}^{k}} \tag{4.30}$$

The tangent stiffness matrix $\mathbf{K}_T$ is obtained by taking partial derivative of current internal forces with respect to current solution. The compact form of Eq. (4.29) in CUF notation can be written as:

$$\mathbf{k}_T^{\tau s i j} \Delta\mathbf{u}_{\tau i} = \boldsymbol{\phi}_{sj} \tag{4.31}$$

with $\mathbf{k}_T^{\tau s i j}$ as FN of the tangent stiffness matrix and $\boldsymbol{\phi}_{sj}$ residual nodal vector of unbalanced forces. A new tangent matrix has to be computed at each iteration. Since current work is limited to physically nonlinear problems, formulation of tangent stiffness nucleus is reduced to obtaining material tangent matrix. The tangent fundamental nucleus for CUF are thus obtained as follows:

$$\mathbf{k}_T^{ij\tau s} = \int_V \mathbf{B}_{sj}^T \mathbf{C}^d \mathbf{B}_{\tau i} dV \tag{4.32}$$

where $\mathbf{C}^d$ is the damaged material matrix introduced in Section 2.1.

The effectiveness of an incremental solution methods relies on robust and realistic termination criteria. A loose convergence criteria can lead to inaccurate results whereas tight convergence criteria can yield very high computational cost due to increased number of additional iterations. The following displacement-based convergence criteria is employed:

$$\frac{||\Delta \mathbf{u}^k_{n+1}||}{||\mathbf{u}_{n+1}||} \leq \text{tolerance} \tag{4.33}$$

Chapter 5

Coupling of PD sub-domains with CUF-based finite elements

This chapter presents two procedures implemented for coupling higher-order 1D and 2D CUF-based finite elements with 3D PD sub-regions. In fact, the non-local nature of PD has made the latter a powerful tool for dealing with discontinuities and, consequently, crack propagation analysis. Nevertheless, this non-local nature can represent a major shortcoming when dealing with large and complex structures since the fact that every point of a PD grid interacts with all points within its neighbourhood leads to an exponential increase in computational costs. Thus, researchers are pushing towards the coupling of PD with a numerical method based on classical continuum mechanics, such as FEM. In this way, the advantages of both methods can be exploited, for example, by introducing a PD grid in small regions where the crack is likely to develop and modelling the remaining domain with FEM discretization. Two methods are here presented. The first one is based on the adoption of Lagrange multipliers at the interface surface between PD and FEM domains. Furthermore, a second method, based on the continuity of the displacement field at the interface, is hereinafter described.

5.1 Lagrange multipliers method

In this section, the coupling approach based on the use of Lagrange multipliers is presented. This method has already been tested within the CUF framework for

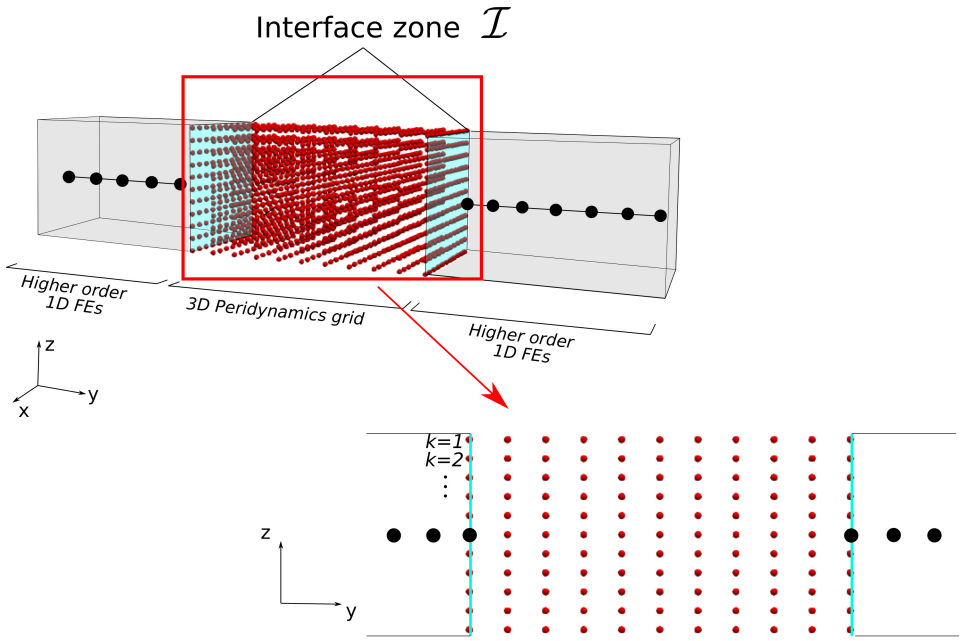

Fig. 5.1 Refined 1D finite elements based on classical elasticity are integrated with a 3D peridynamic region through Lagrange multipliers. Within the interface zone $\mathscr{I}$, the Lagrangian Π_k for each particle $k \in \mathscr{I}$ is included in the coupled (singular) FE-PD system to ensure displacement continuity.

coupling of combining variable kinematic models, whereas here is adopted to couple FEM and PD domains. Figure 5.1 illustrates a rectangular cross-section solid beam within a Cartesian reference system. A segment of the solid body is represented using 3D peridynamics (peridynamic particles are depicted as red dots), while the remaining portion of the domain is discretized using high-order 1D elements. In the absence of any interface relationship, the peridynamic region and the finite elements can be treated independently. Equations (4.25) and (3.22) are combined in a weak sense to form the following system of linear algebraic equations:

$$\mathbf{K}\boldsymbol{U} = \mathbf{F}, \text{ i.e. } \begin{bmatrix} \mathbf{K}^{PD} & \mathbf{0} \\ \mathbf{0} & \mathbf{K}^{FE} \end{bmatrix} \begin{Bmatrix} \mathbf{U}^{PD} \\ \mathbf{U}^{FE} \end{Bmatrix} = \begin{Bmatrix} \mathbf{F}^{PD} \\ \mathbf{F}^{FE} \end{Bmatrix} \tag{5.1}$$

It should be observed that the global stiffness matrix $\mathbf{K}$ as described in Eq. (5.1) is singular, having a quantity of zero eigenvalues equivalent to 6 times the number of independent solid domains (for instance, 6×3 as depicted in Fig. 5.1). In the presence of an interface (contact) region, indicated by $\mathscr{I}$, between the peridynamic domain and the high order FEs, Lagrange multipliers are employed to fulfill the

congruence conditions on $\mathscr{I}$ and resolve the singularity of $\mathbf{K}$. To achieve this, let's focus on a single peridynamic particle k among the $N_{\mathscr{I}}$ particles situated on $\mathscr{I}$. The functional (Lagrangian) to be incorporated into the original problem described in Eq. (5.1) is as follows:

$$\Pi_k = \boldsymbol{\lambda}_k^T \left(\mathbf{u}_k^{PD} - \mathbf{u}^{FE}(x_k, y_k, z_k) \right) \tag{5.2}$$

where $\mathbf{u}_k^{PD}$ is the displacement vector of PD particle k and $\mathbf{u}^{FE}(x_k, y_k, z_k)$ is the displacement field of the FE counterpart. $\boldsymbol{\lambda}_k$ is the three-component vector containing the Lagrange multipliers; they represent the forces to be applied to the system in order to satisfy continuity between the peridynamic particle and the FE approximation at k. After subtituting Eq. (4.15) into Eq. (5.2), one has

$$\Pi_k = \boldsymbol{\lambda}_k^T \left(\mathbf{u}_k^{PD} - \mathbf{u}_{\tau i}^{FE} F_\tau(x_k, z_k) N_i(y_k) \right), \quad \tau = 1, ..., M, \quad i = 1, ..., p+1 \tag{5.3}$$

Equation (5.3) is, thus, expanded over τ and i to obtain, in a matrix form, the following expression:

$$\Pi_k = \boldsymbol{\lambda}_k^T \mathbf{B}_k \mathbf{U} \tag{5.4}$$

where $\mathbf{B}_k$ is the coupling matrix of particle k and its fundamental kernel is written as:

$$\mathbf{B}_k^{\tau i} = \left(\delta_k - F_\tau(x_k, z_k) N_i(y_k) \right) \mathbf{I} \tag{5.5}$$

where $\mathbf{I}$ is the 3×3 identity matrix and δ_k is 1 for PD particle k and null otherwise.

Once the Lagrangian for each particle $k \in \mathscr{I}$ is determined and the total functional $\Pi = \sum_{k=1}^{N_{\mathscr{I}}} \Pi_k$ is computed, the solution to the coupled problem involves finding $\mathbf{U}$ and $\boldsymbol{\lambda}$ (a vector of Lagrange multipliers with $3 \times N_{\mathscr{I}}$ components) from the following linear system:

$$\begin{cases} \mathbf{K}\mathbf{U} + \dfrac{\partial \Pi}{\partial \mathbf{U}} = \mathbf{F} \\ \dfrac{\partial \Pi}{\partial \boldsymbol{\lambda}} = 0 \end{cases} \tag{5.6}$$

or, equivalently,

$$\begin{bmatrix} \mathbf{K} & \mathbf{B}^T \\ \mathbf{B} & \mathbf{0} \end{bmatrix} \begin{Bmatrix} \mathbf{U} \\ \boldsymbol{\lambda} \end{Bmatrix} = \begin{Bmatrix} \mathbf{F} \\ \mathbf{0} \end{Bmatrix} \tag{5.7}$$

where $\mathbf{B}$ is the final coupling matrix obtained through the assembly of $\mathbf{B}_k$ matrices. Equation (5.7) can be resolved once geometrical and boundary conditions are applied, for instance, through the utilization of a penalty method.

5.2 Smeared coupling method

The main advantage of the method based on the use of Lagrange multipliers lies in the possibility of having a straightforward implementation and in its practical meaning because multipliers represent the forces to be applied to satisfy continuity. However, this coupling approach may lead to minor errors at domains interface, because PD and local FEM converge to two different soluitions in the case of non-null horizon. For this reason, a second coupling method has been proposed in this work, which is based on the continuity of the displacement field at the interface [31, 137]. From now on, we will refer to this approach as the smeared coupling method since, in this case, there is no surface representing the interface domain but a region whose length depends on the horizon radius.

5.2.1 1D coupling of FEs and PD nodes

Let us consider a 1D body that has been discretized into two regions: one using 1D Finite Elements (FEs) and the other using equispaced PD nodes. This configuration is illustrated in Fig. 5.2. Each PD node represents a portion of the 1D body of length Δx and is positioned at the center of this portion. Consequently, the PD node closest to the interface is located at a distance of $\Delta x/2$ from the interface itself, as depicted in Figure 5.2a. On the contrary, the closest FEM node is precisely situated at the interface. For simplicity, we assume that the length $\Delta\ell$ of the FEs remains constant. It is important to note that the length $\Delta\ell$ of the FEs and the PD spacing Δx are not necessarily equal to each other.

To account for the forces at the interface, fictitious nodes are introduced beyond the interface itself. This includes adding a fictitious FEM node in the PD region and introducing fictitious PD nodes in the FEM region. The fictitious FEM node is positioned at a distance of $\Delta\ell$ from the interface, as depicted in Figure 5.2b. Its displacement is determined by interpolating the displacements of the real PD nodes surrounding it. Since the fictitious FEM node is located in the PD region and does

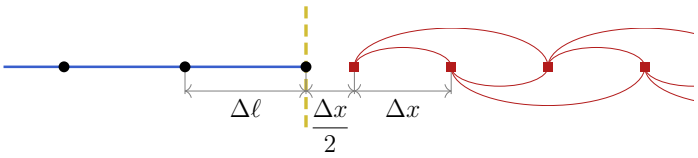

(a) The initial geometry consists of real FEs represented by blue lines, each with a length of $\Delta\ell$, and real PD nodes depicted as red squares, uniformly spaced with a spacing of Δx. The bonds between the FEs and PD nodes are represented by a red line, indicating a distance of $\delta = 2\Delta x$, and the interface between the FEM and PD regions is depicted as a yellow dashed line.

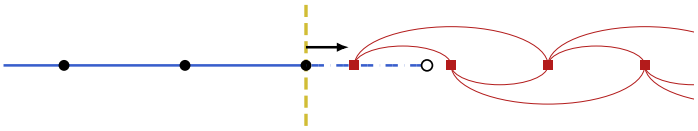

(b) To address the force interaction between the FEM and PD regions at the interface, a fictitious FE is introduced within the PD region. This fictitious FE is responsible for providing the force acting on the real FEM node located at the interface. The displacement of the fictitious FEM node is determined by interpolating the displacements of the real PD nodes surrounding it. The fictitious FEM node is represented by an empty circle in the diagram.

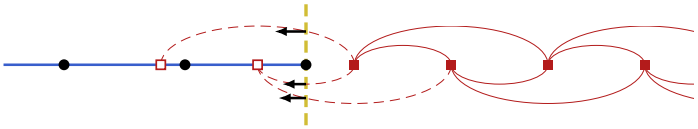

(c) Fictitious PD nodes are introduced in the FEM region to provide forces to the real PD nodes near the interface. The forces are transmitted through fictitious bonds (red dashed lines). The displacements of the fictitious PD nodes are determined by interpolating the displacements of the real FEM nodes.

Fig. 5.2 Coupling between 1D FEs and peridynamic nodes: the described interpolations ensure the continuity of the displacement field at the interface.

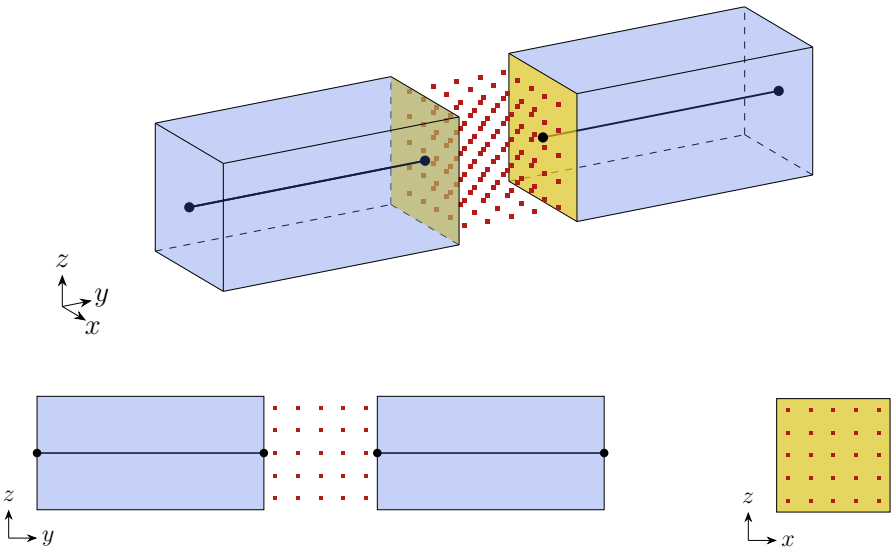

Fig. 5.3 Coupling of high order 1D FEs (blue region) with 3D peridynamic nodes (red squares). The yellow surfaces are the interfaces between FEM and peridynamic regions.

not experience any FEM forces, it is not influenced by the force of the fictitious FE. However, this force is applied to the real FEM node at the interface. It is important to note that the force of the fictitious FE depends on the displacements of the real PD nodes due to the displacement interpolation. Additionally, in order to complete the neighborhoods of the real PD nodes near the interface, fictitious PD nodes are introduced in the FEM region, as shown in Figure 5.2c. The displacements of the fictitious PD nodes can be determined through interpolation using the displacements of the real FEM nodes. The forces exerted by the fictitious bonds, specifically the bonds crossing the interface, are only applied to the real PD nodes since the fictitious PD nodes are situated in the FEM region. It is worth noting that the forces of the fictitious bonds depend on the displacements of the real FEM nodes due to the displacement interpolation.

For a linear displacement field, the force exerted on the FEM node at the interface via the fictitious FE (as depicted in Figure 5.2b) is equal to the sum of the forces applied to the real PD nodes through the fictitious bonds (as shown in Figure 5.2c) [138]. The principles of this smeared coupling method can be extended to couple a 3D peridynamic grid with high-order 1D elements. An example of such coupling is illustrated in Figure 5.3.

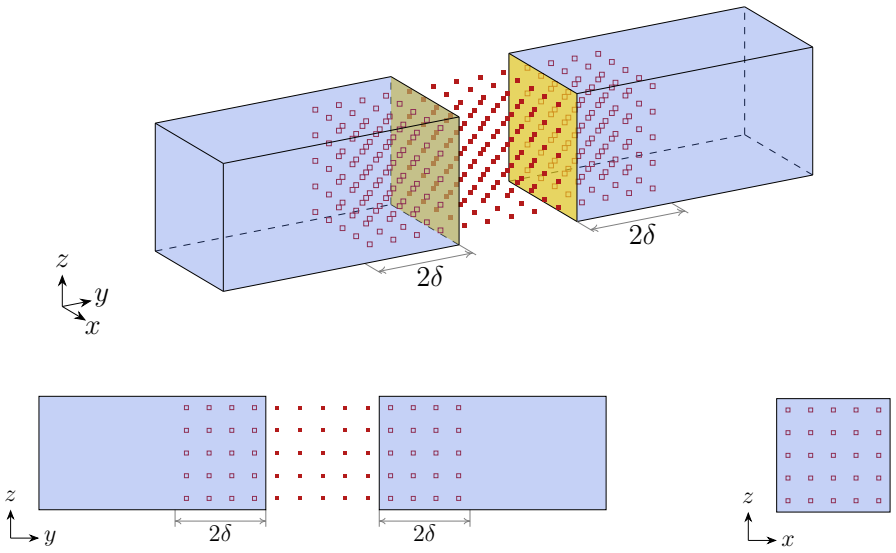

Fig. 5.4 Coupling of FEs (blue region) with 3D peridynamic nodes (red solid squares): additional fictitious peridynamic nodes (red empty squares) are introduced within the finite elements up to a distance of 2δ from the interfaces (yellow surfaces).

5.2.2 Interpolation of PD nodal displacements with FEM

In state-based Peridynamics, the interaction range between nodes extends to a distance of 2δ from each node [139]. To ensure accurate interaction between the FEs and PD nodes, fictitious PD nodes are incorporated within the FEs up to a distance of 2δ from the interfaces [140], as depicted in Figure 5.4 The displacements of these fictitious PD nodes can be determined by interpolating the displacements of the FE nodes, allowing for accurate force transfer and interaction between the FEs and PD nodes.

Let us consider, for instance, a fictitious PD node p with a position vector $\mathbf{x}_p = \{x_p, y_p, z_p\}^\top$. Since its position is known, it is straightforward to determine within which FE node p lies. Hence, the FE shape functions N_i and the expansion functions F_τ of that element are used to compute the displacement of node p:

$$\mathbf{u}^{f\text{-}PD}(x_p, y_p, z_p) = \sum_i \sum_\tau N_i(y_p) F_\tau(x_p, z_p) \mathbf{u}_{\tau i}^{FE}, \tag{5.8}$$

where $f\text{-}PD$ stands for fictitious peridynamic nodes. By repeating Equation 5.8 for each fictitious PD node, we obtain the following system of equations:

$$\mathbf{U}^{f\text{-}PD} = \mathbf{I}^{f\text{-}PD}\mathbf{U}^{FE}, \tag{5.9}$$

where $\mathbf{U}_f^{PD}$ is the peridynamic displacement vector of the fictitious peridynamic nodes, $\mathbf{I}^{f\text{-}PD}$ is the fictitious PD interpolation matrix and $\mathbf{U}^{FE}$ is the vector of the FE nodal unknowns. Note that the dimensions of $\mathbf{I}^{f\text{-}PD}$ are $3N^{f\text{-}PD} \times 3N^{FE}$, where $N^{f\text{-}PD}$ is the number of fictitious PD nodes and $3N^{FE}$ is the number of the FE nodal unknowns.

5.2.3 Interpolation of FE nodal displacements with PD

To initiate our analysis, let us consider a simplified case where the sections of the FE nodes are perpendicular to the FEs. As illustrated in Figure 5.5, we introduce fictitious FE nodes strategically positioned so that their associated sections align with the plane of the real nodes nearest to the interface. For each real PD node, denoted as q, residing on the section of a fictitious FE node, the following equation can be formulated:

$$\mathbf{u}^{PD}(x_q, y_q, z_q) = \sum_i \sum_\tau N_i(y_q) F_\tau(x_q, z_q) \mathbf{u}_{\tau i}^{f\text{-}FE}, \tag{5.10}$$

where $\mathbf{u}_{\tau i}^{f\text{-}FE}$ contains the generalized degrees of freedom associated to the fictitious FE node. Equation 5.10 can be written in a matrix form as:

$$\mathbf{U}^{PD} = \mathbf{I}^{fs\text{-}PD}\mathbf{U}^{fs\text{-}FE}, \tag{5.11}$$

where $\mathbf{U}^{PD}$ is the peridynamic displacement vector, $\mathbf{I}^{fs\text{-}PD}$ is the interpolation matrix and $\mathbf{U}^{fs\text{-}FE}$ is the vector of the degrees of freedom of the section associated to a fictitious FE node.

However, we want to express the latter degrees of freedom ($\mathbf{U}^{fs\text{-}FE}$) as functions of the displacements of the real PD nodes ($\mathbf{U}^{PD}$) by inverting the matrix $\mathbf{I}^{fs\text{-}PD}$. Note that, in general, $\mathbf{I}^{fs\text{-}PD}$ is not a square matrix and therefore is not invertible. Thus, we use the relationship of each degree of freedom of the fictitious FE node with the shape function N_i and expansion function F_τ. These functions can be used as weights to compute, for each FE degree of freedom, the weighted average of the

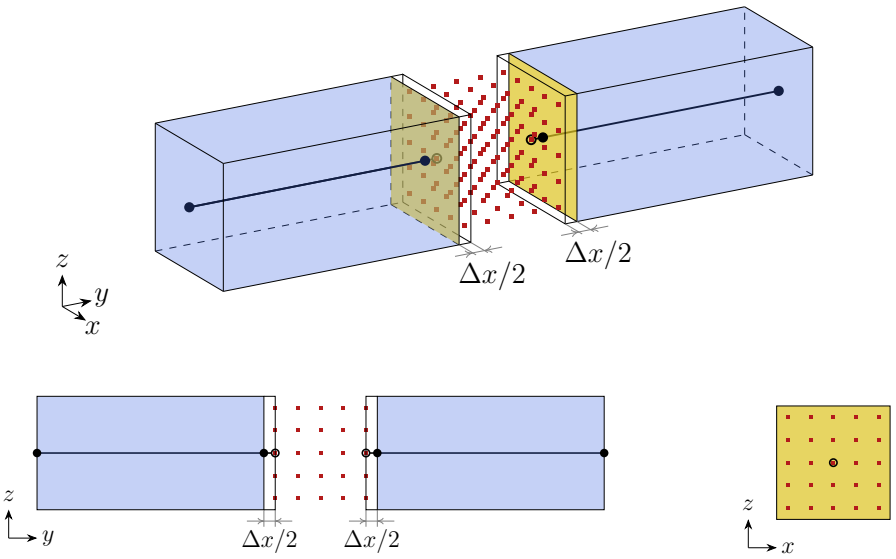

Fig. 5.5 In the coupling of FEs within the blue region and 3D peridynamic nodes denoted by red squares, fictitious FEs are introduced so that their sections, illustrated as empty circles, align with the plane defined by the nearest real peridynamic nodes to the interfaces, depicted by yellow surfaces.

displacements of all the real PD nodes lying on the section of the fictitious FE node:

$$\mathbf{u}_{\tau i}^{AV} = \frac{\sum_q |N_i(y_q) F_\tau(x_q, z_q)| \mathbf{u}^{PD}(x_q, y_q, z_q)}{\sum_q |N_i(y_q) F_\tau(x_q, z_q)|}, \tag{5.12}$$

or

$$\mathbf{U}^{AV} = \mathbf{A}\,\mathbf{U}^{PD}, \tag{5.13}$$

where $\mathbf{u}_{\tau i}^{AV}$ is the generic averaged displacement of the fictitious section and $\mathbf{U}^{AV}$ is the vector containing them. Note that $\mathbf{U}^{AV}$ has the same dimension of $\mathbf{U}^{fs\text{-}FE}$, so that $\left[\mathbf{A}\,\mathbf{I}^{fs\text{-}PD}\right]$ is a square matrix. This allows us to express the degrees of freedom of the fictitious FE node as functions of the displacements of the real PD nodes:

$$\begin{aligned} \mathbf{U}^{fs\text{-}FE} &= \left[\mathbf{A}\,\mathbf{I}^{fs\text{-}PD}\right]^{-1} \mathbf{U}^{AV} \\ &= \left[\mathbf{A}\,\mathbf{I}^{fs\text{-}PD}\right]^{-1} \mathbf{A}\,\mathbf{U}^{PD}. \end{aligned} \tag{5.14}$$

If this procedure is repeated for all the fictitious FE nodes, then the following matrix can be assembled:

$$\mathbf{U}^{f\text{-}FE} = \mathbf{I}^{f\text{-}FE}\mathbf{U}^{PD}, \tag{5.15}$$

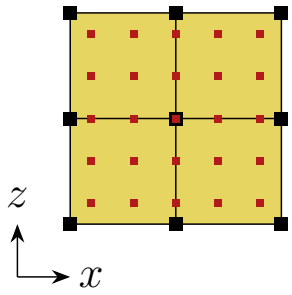

Fig. 5.6 Example of a FE node with multiple FE sections where some fictitious FE nodes are part of more-than-one section and some real PD nodes are located in more-than-one section.

where $\mathbf{U}^{f\text{-}FE}$ is the vector of the degrees of freedom of the fictitious FE nodes and $\mathbf{I}^{f\text{-}FE}$ is the fictitious FE interpolation matrix. Note that the dimensions of $\mathbf{I}^{f\text{-}FE}$ are $3N^{f\text{-}FE} \times 3N^{PD}$, where $3N^{f\text{-}FE}$ is the number of the FE nodal unknowns and N^{PD} is the number of real PD nodes.

5.2.4 Interfaces parallel to FEs

Let us consider another scenario where an interface aligns parallel to the y-axis, corresponding to the bar's axis, as depicted in Fig. 5.7. Extending this example to more intricate situations involving interfaces perpendicular to both the x and z axes is relatively straightforward. Following the approach outlined in Section 5.2.2, we introduce fictitious PD nodes within the finite elements (FEs) to envelop the interfaces with a PD layer of thickness 2δ, as illustrated in Fig. 5.8. The equation 5.8 remains applicable and can be utilized to construct the fictitious PD interpolation matrix $\mathbf{I}^{f\text{-}PD}$.

On the contrary, within the PD region, fictitious FE sections are incorporated to align with the nearest plane of actual PD nodes, as depicted in Fig.5.9. It's noteworthy that this geometry gives rise to a novel type of fictitious FEs: in proximity to the interface edges, certain fictitious FEs possess only one edge aligned with a row of real PD nodes. The remaining edges of these elements are situated on the external surface of real FEs. Consequently, there are no corresponding sections for these newly introduced elements as those utilized in Section5.2.3 to interpolate the displacements of the fictitious FE nodes.

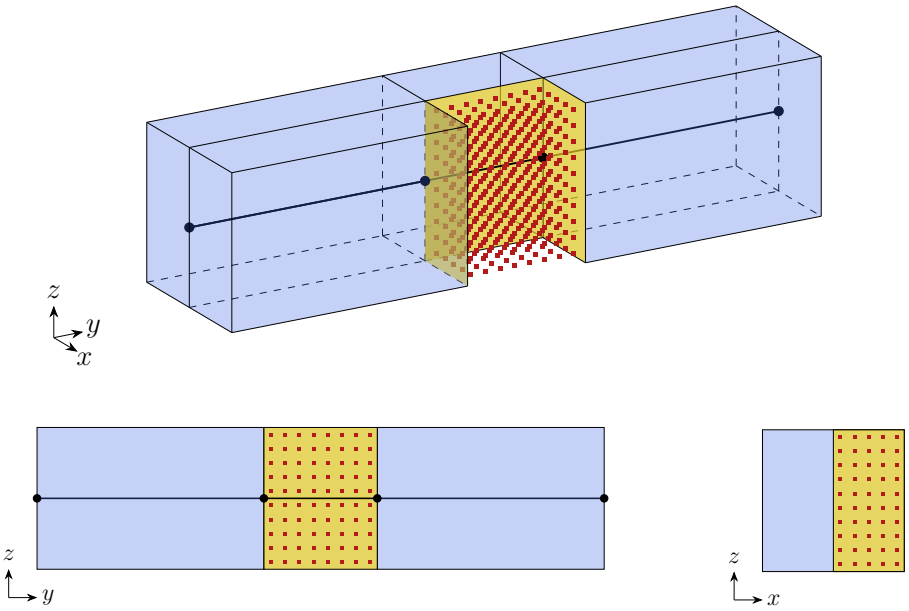

Fig. 5.7 Coupling of high order 1D FEs (blue region) with 3D peridynamic nodes (red squares) when one of the interfaces (yellow surfaces) is parallel to the axis of the bar.

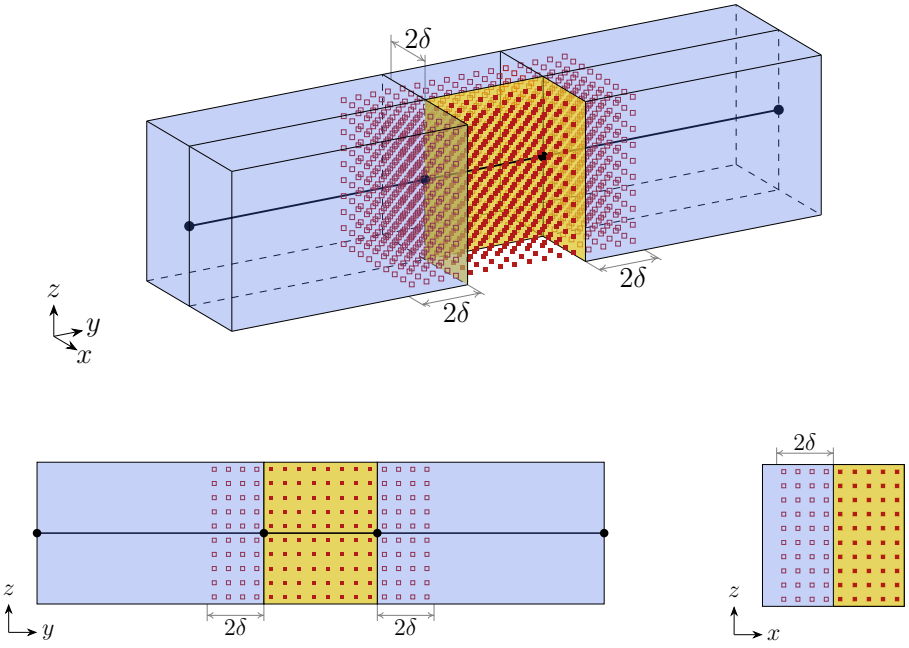

Fig. 5.8 Coupling of FEs (blue region) with 3D peridynamic nodes (red solid squares): within the finite elements, fictitious PD nodes (red empty squares) are added up to a distance of 2δ from all interfaces (yellow surfaces), including those that align parallel to the axis of the bar.

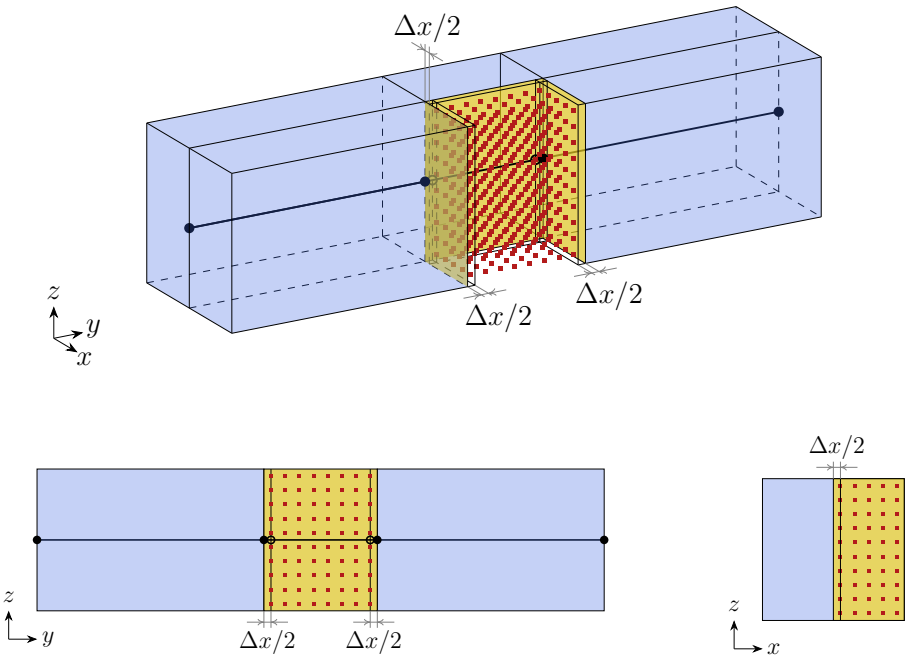

Fig. 5.9 Coupling of FEs (blue region) with 3D peridynamic nodes (red squares):fictitious finite elements are introduced such that their sections align with the plane of the nearest real PD nodes to the interfaces (yellow surfaces). Additionally, a new type of elements arises near the edges between the interfaces.

In this instance, the interpolation of displacements for the fictitious FE nodes positioned along the PD node row is facilitated by the involvement of two fictitious FE sections, as elaborated in Section 5.2.3. It's worth noting that the row of PD nodes contributes to both interpolations of the two fictitious FE sections. Similarly, as the fictitious FE nodes positioned along that edge are shared between the two fictitious FE sections, their displacements are determined as the averages of the interpolations derived from the two sections. As for the remaining fictitious FE nodes situated along the external surfaces of real FEs, their interpolation is simply achieved through the FE shape functions N_i and the expansion functions F_τ of those elements:

$$\mathbf{u}^{fe\text{-}FE}(x_p, y_p, z_p) = \sum_i \sum_\tau N_i(y_p) F_\tau(x_p, z_p) \mathbf{u}_{\tau i}^{FE}, \tag{5.16}$$

where $\mathbf{u}^{fe\text{-}FE}$ is the vector of the degrees of freedom of the fictitious FE nodes on one of these edges. Equation 5.16 is employed during the assembling of the fictitious FE interpolation matrix $\mathbf{I}^{f\text{-}FE}$.

5.2.5 3D coupling of FEs and PD nodes

This section is dedicated to the assembly of the stiffness matrix of the complete system of (both FE and PD) equations. We assemble the global FE stiffness matrix $\mathbf{K}^{gl-FE}$ following the methodology outlined in Chapter 4 by considering both real and fictitious elements. The real FE stiffness matrix $\mathbf{K}^{FE}$ is then derived by removing all rows and columns in $\mathbf{K}^{gl-FE}$ associated with fictitious FE degrees of freedom. On the other hand, the fictitious FE stiffness matrix $\mathbf{K}^{f-FE}$ is generated by eliminating the rows corresponding to fictitious FE degrees of freedom and the columns corresponding to real FE degrees of freedom. It's important to note that the rows associated with fictitious degrees of freedom are not used as they pertain to fictitious FE forces. These fictitious FE nodes exist within the peridynamic region and are not subject to any FE forces, as elucidated in Section 5.2.1.

Similarly, as detailed in Section 3.1, we construct the global PD stiffness matrix $\mathbf{K}^{gl-PD}$ by considering both real and fictitious PD nodes. Since the fictitious PD nodes reside within FEs, they are not subject to fictitious PD forces. Consequently, the corresponding rows of $\mathbf{K}^{gl-PD}$ are eliminated. We then derive the real PD stiffness matrix $\mathbf{K}^{PD}$ and the fictitious PD stiffness matrix $\mathbf{K}^{f-PD}$ by eliminating the columns corresponding to the fictitious and real degrees of freedom, respectively.

Thus, the system of equations can be written in the following matrix form:

$$\begin{bmatrix} \mathbf{K}^{FE} & \mathbf{K}^{f-FE}\mathbf{I}^{f-FE} \\ \mathbf{K}^{f-PD}\mathbf{I}^{f-PD} & \mathbf{K}^{PD} \end{bmatrix} \begin{bmatrix} \mathbf{U}^{FE} \\ \mathbf{U}^{PD} \end{bmatrix} = \begin{bmatrix} \mathbf{F}^{FE} \\ \mathbf{F}^{PD} \end{bmatrix}, \tag{5.17}$$

or

$$\mathbf{KU} = \mathbf{F}, \tag{5.18}$$

where $\mathbf{K}$ is the stiffness matrix of the entire system, which is no more singular and positive semidefinite, $\mathbf{U}$ is the displacement vector and $\mathbf{F}$ is the force vector.

Chapter 6

Global-local analysis

This chapter introduces a global/local approach adopted for the analysis of three-dimensional stress states of composite laminated structures. It consists of a two-step procedure. In particular, the first step makes use of finite element modelling based on classical 2D plate elements by using commercial FE software, whereas a refined layer-wise model based on CUF is employed to extract the 3D stress and strain fields in some critical regions that may have arbitrary dimensions. This approach allows for dealing with large local areas, increasing the static solution's accuracy and possibly embedding this technique in more complex procedures, such as the least-weight design of large heterogeneous complex assemblies and stiffness optimization. Furthermore, the proposed method is extended to deal with localized progressive failure analysis using coupled FEM-PD models within the local refined domain.

6.1 Two-step procedure for composite laminates

The global/local strategy adopted in this work consists of two steps that can be summarized in the following way:

1. **A global analysis on a composite laminate is conducted**. The commercial software Nastran [141] is used to perform the analysis of the total structure. This step is recalled as global analysis. Classical CQUAD4 elements are adopted in combination with PCOMP properties for the geometrical and material descriptions, respectively. CQUAD4 elements make use of First Shear

order Deformation theory (FSDT) [142], according to which the displacement field is given as follows:

$$\begin{aligned} u_1(x,y,z) &= u(x,y) + z\varphi_x \\ u_2(x,y,z) &= v(x,y) + z\varphi_y \\ u_3(x,y,z) &= w(x,y) \end{aligned} \tag{6.1}$$

where u, v, w, φ_x and φ_y are five unknown displacement functions of the mid-plane of the plate. The key contribution of this study is the expansion of the CUF-based global/local analysis approach to include a patch-wise (PW) formulation. This novel approach enables the selection of a group of global elements for local analysis, providing more accurate results than the traditional element-wise (EW) approach, where only a single CQUAD element is locally refined at a time. Notably, prior research [68, 143] has only explored the EW approach within the CUF framework.

2. **A local analysis on the domain elements is performed**. The refined local analysis is conducted using high order 2D plate CUF-based elements. The 3D displacement field $\mathbf{u}(x,y,z)$ is thus defined as a 1D through-the-thickness expansion function of the primary unknowns, evaluated via the finite element method. The relation can be written as follows:

$$\mathbf{u}(x,y,z) = F_\tau(z) N_i(x,y) \mathbf{q}_{\tau i} \tag{6.2}$$

where F_τ is the expansion function, N_i the shape function and $\mathbf{q}_{\tau i}$ the nodal unknowns vector. Index τ represents the number of terms in the thickness expansion, while the subscript i denotes the number of structural finite element nodes. This research adopts 2D sixteen-nodes cubic elements (Q16) as shape functions for the in-plane modeling. Cubic Lagrange polynomials are employed as F_τ function (LE). This work adopts the four-node cubic Lagrange expansion function (LD3) over the thickness, where LD stands for Lagrange Displacement-based (see Fig. 6.1).

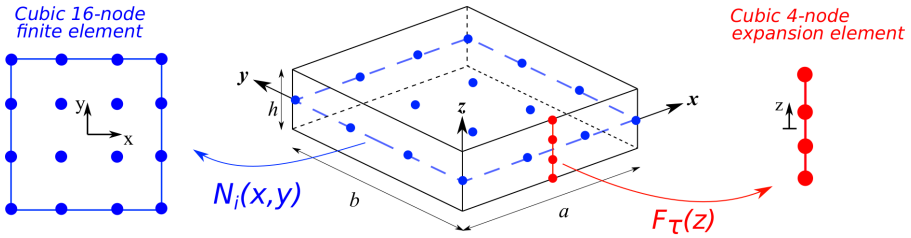

Fig. 6.1 Graphical representation of the cubic interpolation for in-plane and thickness domains.

6.1.1 Local displacement-based model

The CUF model used for the analysis of the local domain is a displacement-based formulation, meaning that pure displacement Degrees of Freedom (DOFs) at each node are considered. Nevertheless, the commercial software provides translational displacements (u_x^0, u_y^0, u_z^0) and rotations $(\theta_x^0, \theta_y^0, \theta_z^0)$ at each node of the global model. Thus, a suitable procedure must be implemented to transform the global model's rotations into pure displacement DOFs. The chosen strategy is the same adopted in previous works [68, 143], where a Reissner-Mindlin displacement field [35, 144] is employed for the computation of translational displacements at the local model boundaries. The Reissner-Mindlin displacement field which operates is written as follows:

$$\begin{aligned}
\boxed{u_x}(x,y,z) &= \textcircled{u_x^0}(x,y) + z\,\textcircled{\theta_y^0}(x,y) - y\,\textcircled{\theta_z^0}(x,y) \\
\boxed{u_y}(x,y,z) &= \textcircled{u_y^0}(x,y) - z\,\textcircled{\theta_x^0}(x,y) + x\,\textcircled{\theta_y^0}(x,y) \\
\boxed{u_z}(x,y,z) &= \textcircled{u_z^0}(x,y) - x\,\textcircled{\theta_y^0}(x,y) + y\,\textcircled{\theta_x^0}(x,y)
\end{aligned} \tag{6.3}$$

where the circled quantities u_x^0, u_y^0, u_z^0 and $\theta_x^0, \theta_y^0, \theta_z^0$ are displacements and rotations of the global model, whereas the boxed ones u_x, u_y, u_z are the pure translational displacement DOFs in the refined model . The graphical representation of these transformation is shown in Fig. 6.2.

6.1.2 Patch-wise formulation

A common procedure for EW and PW formulations consists of the computation of displacements in all interface nodes using global rotations, which are then employed as boundary conditions for the local model. Nevertheless, in the precedent

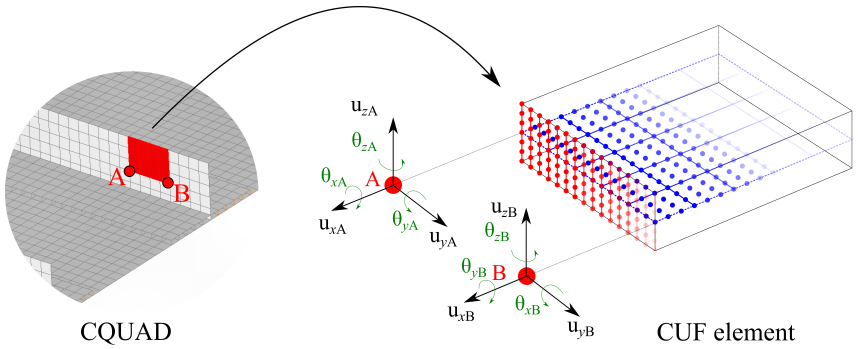

Fig. 6.2 Graphical representation of the procedure to transform rotational DOFs of the global model into pure displacement for local one. The evaluated displacements, i.e. the boxed u_x, u_y, u_z of Eq. 6.3 are used as boundary condition of the local element. Two LD3 are used for thickness modeling in the local domain.

EW formulation, displacements and rotations only from a single chosen CQUAD element were adopted as boundary conditions. On the other hand, in the present PW formulation, displacements and rotations from all the involved global nodes are considered and used to construct the boundary condition set. An example of the procedure is illustrated in Fig. 6.3., which also reports the EW approach. On the right, a local region identified by a 2×2 patch of elements is considered. The two areas have the same geometrical dimensions. Let us consider a point located at the quarter $(L/4, 0)$ of the edge described by global nodes 1 and 2. Concerning the EW approach, displacements and rotations evaluated in the point x_{EW} result from the interpolation within the single element CQUAD, referred to as 1_{EW}, which describes the entire region. On the other hand, for the PW model, boundary conditions in point x_{PW} are obtained through interpolation within element 1_{PW}. The refinement of the global mesh, without altering the geometrical dimensions of the local region, will facilitate the provision of more precise boundary conditions, resulting in a more accurate assessment of stress components.

6.2 PD-based progressive failure analysis via global-local method

The two-step global/local analysis can be seen as a free-standing way to obtain a more accurate solution regarding the stress state in specific regions of the structure. However, the features of the proposed approach can be exploited to build a framework

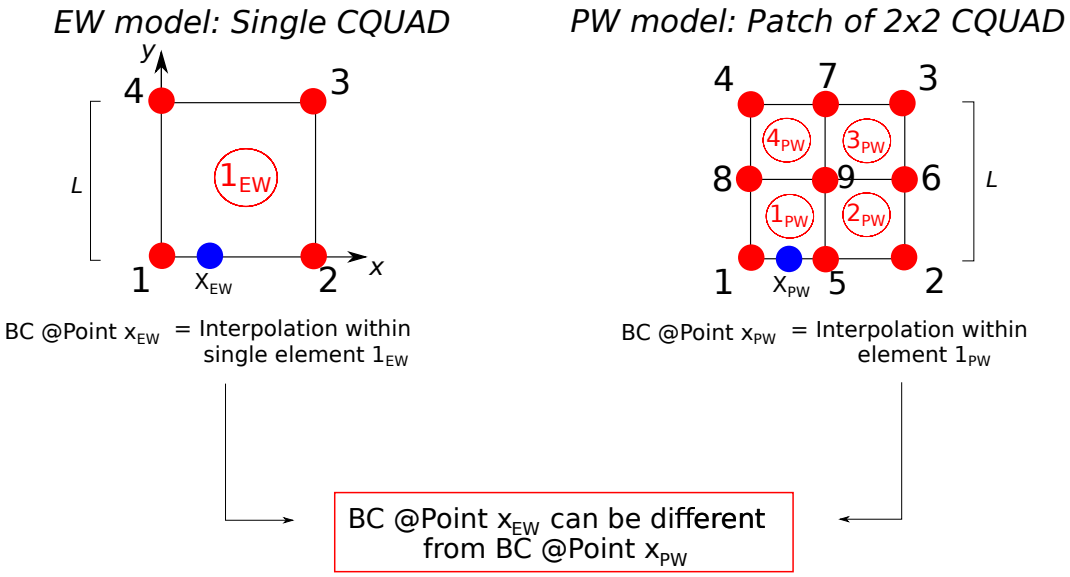

Fig. 6.3 Differences between element-wise and patch-wise formulation in terms of boundary conditions evaluation.

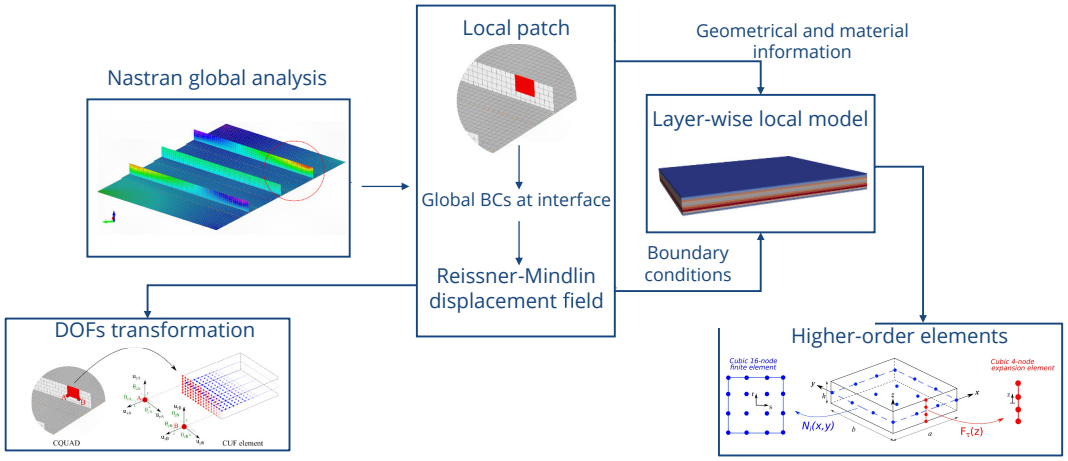

Fig. 6.4 General procedure for the proposed two-step global approach. The first step is represented by the global analysis of a structure using 2D plate finite elements. The middle rectangle shows the operations acting as interface between the global and local models. The rectangle on the right represents the refined local model to be analyzed. The output of this procedure are the strain and stress states in the chosen patch of elements.

for progressive failure analysis in some localized zones, where, for example, a crack is present or more likely to nucleate and propagate. This thesis proposes a framework for PD-based localized progressive failure analysis. This approach consists of the following steps:

1. Structural investigation of the full structure by using low-order theories within the FEM commercial software;
2. Choice of the local region where a crack can arise or propagate, and extraction of the displacement information at the boundaries of this region;
3. Building of the local model by using the coupled FEM-PD approach presented in Section 5.1. Nevertheless, 2D higher-order CUF-based finite elements are coupled with 3D PD domains here. The displacement retrieved at the global scale is imposed as boundary conditions for the local investigation. A single step of the PD-based progressive failure analysis (see Section 3.2) is performed;
4. If any bond is broken within the peridynamic grid, a damage parameter d is computed in order to transfer the information from the local to the global scale;
5. Upon update of the stiffness of global elements undergoing damage at the local scale, the structural analysis is performed.

Thus, this framework comprehends three modelling strategies on two different scales, as shown in Fig. 6.5. The main challenge is represented by the transfer of information on damage status from the local to the global scale. In this work, a scalar parameter has been computed for this purpose:

$$d_k = \frac{Brk}{Init(\delta)} \frac{\delta}{L_c} \tag{6.4}$$

This parameter is computed in the PD domain for each region related to each global element k and then used as a reduction factor for its stiffness. Brk indicates the number of broken bonds within the element k, whereas the index $Init(\delta)$ is the maximum number of bonds for a single particle in the PD region. The characteristic length L_c is calculated as the diagonal of the domain related to the global element k. The entire algorithm is graphically displayed in Fig. 6.6.

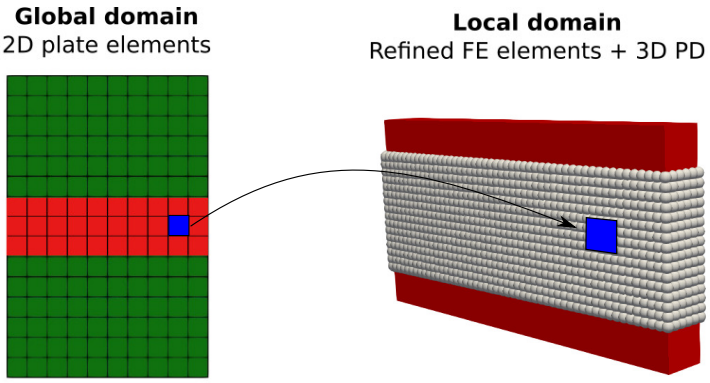

Fig. 6.5 Representation of the three modelling strategies at global and local scales. Low-order 2D theories are used for the global domain. Then, a patch of elements (highlighted in red) are chosen as local zones. The local domain is built by using coupled higher-order 2D FEM and 3D PD particles.

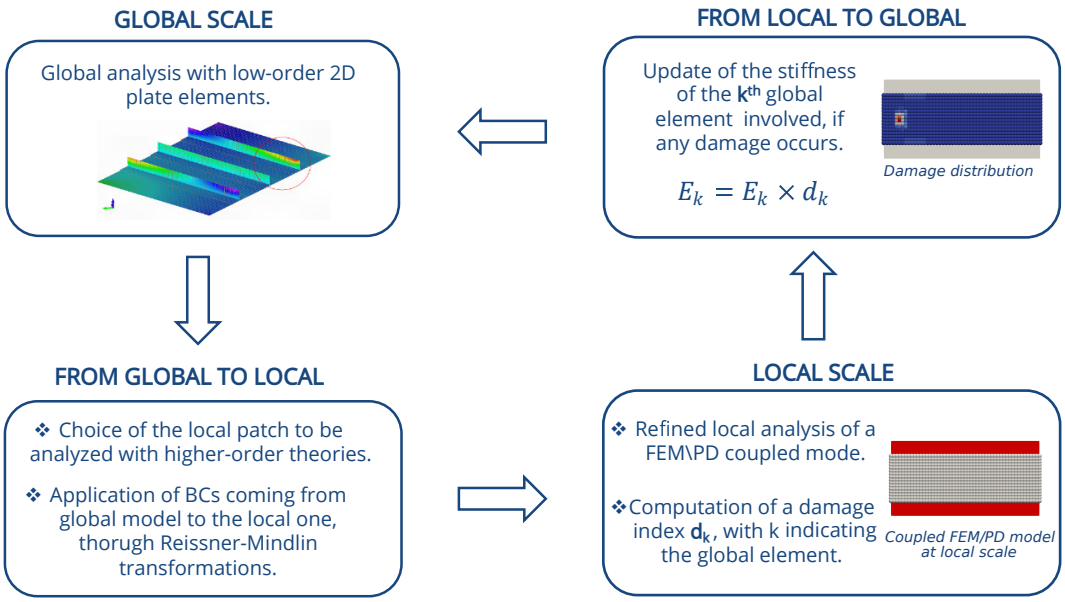

Fig. 6.6 Graphical representation of the implemented algorithm for localized progressive failure analysis.

Chapter 7

Numerical results on damage analysis

This chapter proposes a selection of numerical examples obtained by adopting the formulations and techniques presented in previous chapters. First, progressive failure analyses are performed using the continuum Hashin-based orthotropic model in fibre-reinforced composite laminates. Then, outcomes from static and progressive failure analyses performed by using coupled FEM-PD models are presented. Finally, numerical examples which make use of the global/local approach are proposed for stress evaluation in composite structures, with a supplementary model where a global/local method is adopted for localized progressive failure analysis through coupled FEM-PD models.

7.1 Continuum damage modelling

7.1.1 Single element verification

This section demonstrates the verification process for the proposed orthotropic damage model, focusing on a single component subjected to uniaxial loading. The discretization consists of a 2-node linear finite element (B2) along the y-direction and a single L4 for the cross-section. The adopted material is IM7/8552 carbon fiber reinforced polymer (CFRP), and its corresponding properties are listed in Table 7.1, in accordance with [111]. Tables 7.2 and 7.3 provide details regarding the strength and fracture energies of the material. It is assumed that the interlaminar properties match those of the matrix. The representation of the single element used to validate

Table 7.1 Material properties of IM7/8552 carbon fiber reinforced polymer.

E_{11} [GPa]	E_{22} [GPa]	E_{33} [GPa]	G_{12} [GPa]	G_{13} [GPa]	G_{23} [GPa]	ν_{12} [-]	ν_{13} [-]	ν_{23} [-]
165.00	9.00	9.00	5.60	5.60	2.80	0.34	0.34	0.5

Table 7.2 Longitudinal, transverse, interlaminar and shear strength of CFRP for the single element.

X_T [MPa]	X_C [MPa]	Y_T [MPa]	Y_C [MPa]	Z_T [MPa]	Z_C [MPa]	S_L [MPa]	S_T [MPa]	S_I [MPa]
2560.00	1690.00	73.00	250.00	73.00	250.00	90.00	90.00	90.00

the implementation of the damage model can be observed in Fig. 7.1.
The first numerical evaluation consists of a longitudinal tension resulting in fiber failure along the longitudinal direction. Figure 7.2 presents the stress-strain relationship for this scenario, comparing the current 3D damage model within a CUF framework with the second-generation COmposite DAMage (CODAM2), which has been implemented by using CUF [111] and LS-DYNA [145]. The tensile matrix failure mode is explored by applying tension along the y-direction and setting the fibers in the x-direction. The corresponding stress-strain behavior is depicted in Fig. 7.3. Moreover, the subsequent numerical investigation focuses on a quasi-isotropic laminate with a ply sequence of $[90/45/0\text{-}45]_{2s}$ under uniaxial load. Along the y-direction, a B2 element is employed, with each ply comprising an L4 element. Figure 7.4 displays the stress-strain curve for the quasi-isotropic configuration, whereas Fig. 7.5 provides a comparison of damage evolution in specific layers with the findings of Reiner et al. [145].
Based on the obtained results, the following observations can be made:

1. The incorporation of the Hashin damage model into a 1D CUF framework yields consistent results with the references, with peak stresses aligning with the longitudinal and transverse strengths.

2. The damage model manages to handle different laminations, demonstrating good agreement with the reference data, as depicted in Fig. 7.4. Minor

Table 7.3 Fracture energies of CFRP for the single element.

G_{ft} [MPa·mm]	G_{fc} [MPa·mm]	G_{mt} [MPa·mm]	G_{mc} [MPa·mm]	G_{it} [MPa·mm]	G_{ic} [MPa·mm]
120.00	80.00	2.60	4.20	2.60	4.20

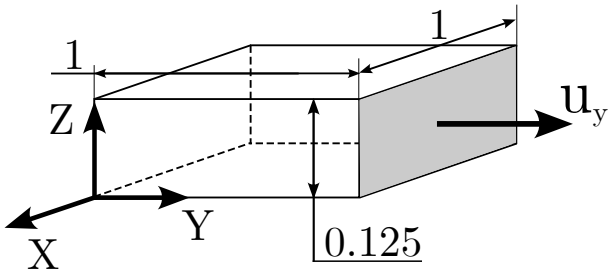

Fig. 7.1 Geometry and dimensions in mm of the single element.

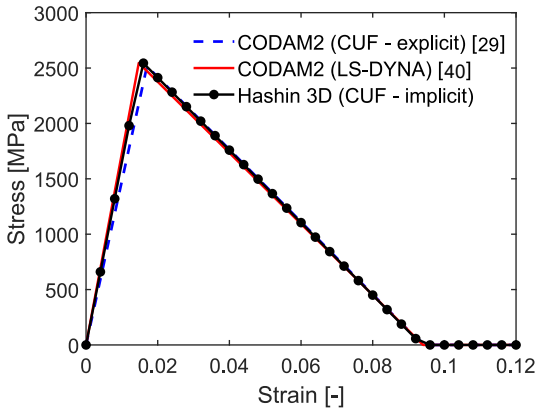

Fig. 7.2 Stress-strain of the single element under uniaxial longitudinal load.

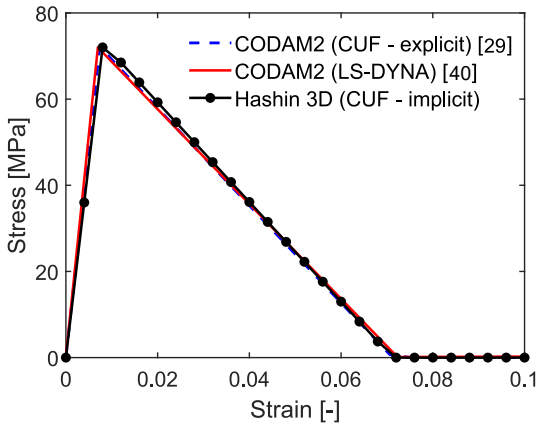

Fig. 7.3 Stress-strain of the single element under uniaxial transversal load.

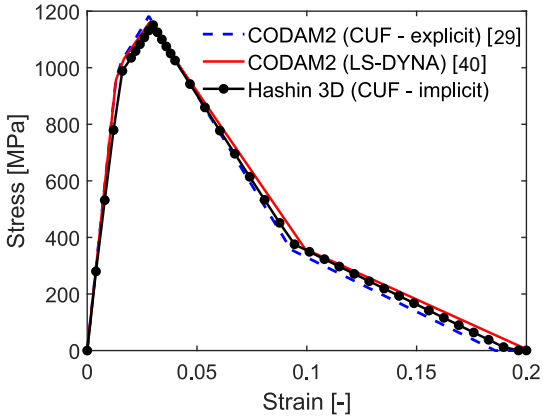

Fig. 7.4 Stress-strain of the single element with a ply sequence of $[90/45/0\text{-}45]_{2s}$ under uniaxial load.

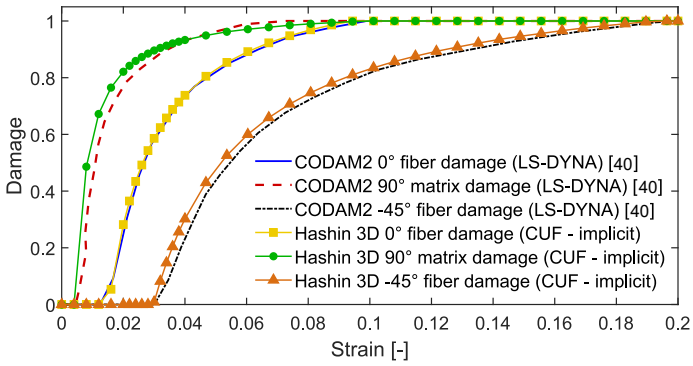

Fig. 7.5 Comparative analysis of fiber and matrix damage evolutions in CUF with CODAM2 framework for the quasi-isotropic single element.

inconsistencies with the CODAM2 can be detected in the softening path; however, the peak force and the displacement at the peak remain consistent.

7.1.2 Compact tension test

This case focuses on the damage analysis of a pultruded glass fiber reinforced polymer (GFRP) compact tension (CT) specimen. The material properties are summarized in Table 7.4, derived from the work of [146, 147]. The specimen has a thickness of 10 mm, with the strengths and fracture energies of the pultruded GFRP provided in Tables 7.5 and 7.6, respectively. The fibers are oriented along the z-direction, whereas the in-plane transversal direction aligns with the x-direction. The lower pin is clamped, and the numerical investigation includes a convergence analysis concerning the order of the adopted beam element, namely 2-node linear (B2), 3-node quadratic (B3), and 4-node cubic (B4) finite elements, considering various configurations. Detailed geometry information and an illustration of the adopted cross-section discretization are provided in Figure 7.6.
Figure 7.7 shows the force-displacement curves for the CUF results, making a comparison with both the experimental tests [148] and 3D Abaqus model [107], where 8-node brick solid finite elements (C3D8) are used. Figure 7.7a illustrates the convergence analysis on the number of elements over the cross-section. Figure 7.7b explicitly considers the effect of mesh size and discretization order, exploring the differences between lower and higher-order kinematic theories in the load-displacement curve. Table 7.7 provides a comparison of the maximum reaction and vertical displacement at peak obtained using CUF with experimental and 3D Abaqus results. Additionally, the table includes the number of degrees of freedom (DOF) for the numerical simulations. Figure 7.8 illustrates the evolution of the tensile matrix damage in the narrow band of the specimen for various applied vertical displacements. Furthermore, in accordance with the findings of Arruda et al. [106], the current damage framework successfully captures the evolution of compressive matrix damage in the specimen, as depicted in Fig. 7.9. Additionally, Fig. 7.10 presents the final distributions of shear damage. In the domain of continuum damage mechanics, the selection of finite elements can give rise to inherent mesh sensitivity, which can carry significant consequences [149]. As highlighted in [150], mesh sensitivity occurs when modifying the type or distortion of finite elements within a fixed mesh, potentially resulting in variations in the solution based on the

Table 7.4 Material properties of the GFRP material for the CT test in the material reference system.

E_{11} [GPa]	E_{22} [GPa]	E_{33} [GPa]	G_{12} [GPa]	G_{13} [GPa]	G_{23} [GPa]	ν_{12} [-]	ν_{13} [-]	ν_{23} [-]
30.00	12.00	12.00	3.00	3.00	2.50	0.24	0.24	0.30

Table 7.5 Longitudinal, transverse, interlaminar and shear strength of the GFRP material for the CT test.

X_T [MPa]	X_C [MPa]	Y_T [MPa]	Y_C [MPa]	Z_T [MPa]	Z_C [MPa]	S_L [MPa]	S_T [MPa]	S_I [MPa]
323.00	426.00	71.00	71.00	71.00	71.00	67.00	64.00	64.00

Table 7.6 Fracture energies of the pultruded GFRP for the CT test.

G_{ft} [MPa·mm]	G_{fc} [MPa·mm]	G_{mt} [MPa·mm]	G_{mc} [MPa·mm]	G_{it} [MPa·mm]	G_{ic} [MPa·mm]
100.00	100.00	20.00	20.00	20.00	20.00

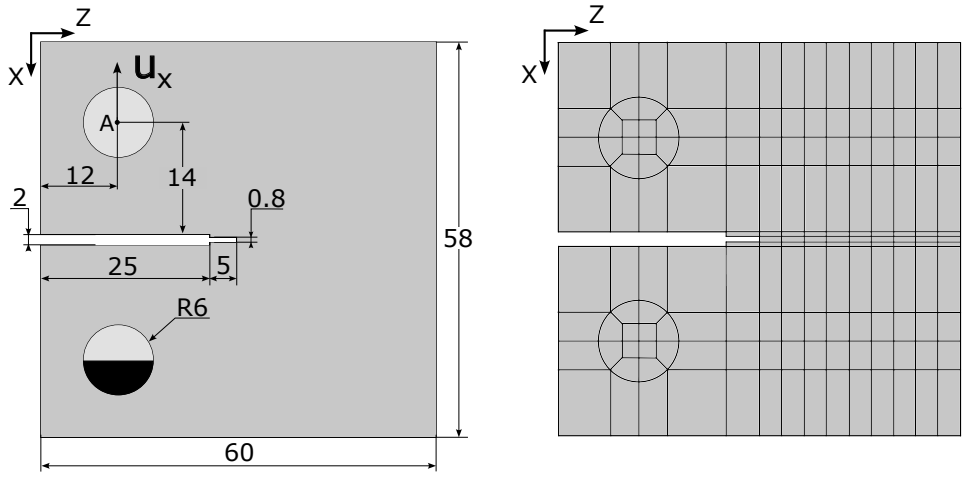

Fig. 7.6 Dimensions of the specimen for the compact tension case in mm, along with an illustration of the cross-section discretization utilizing biquadratic L9 elements.

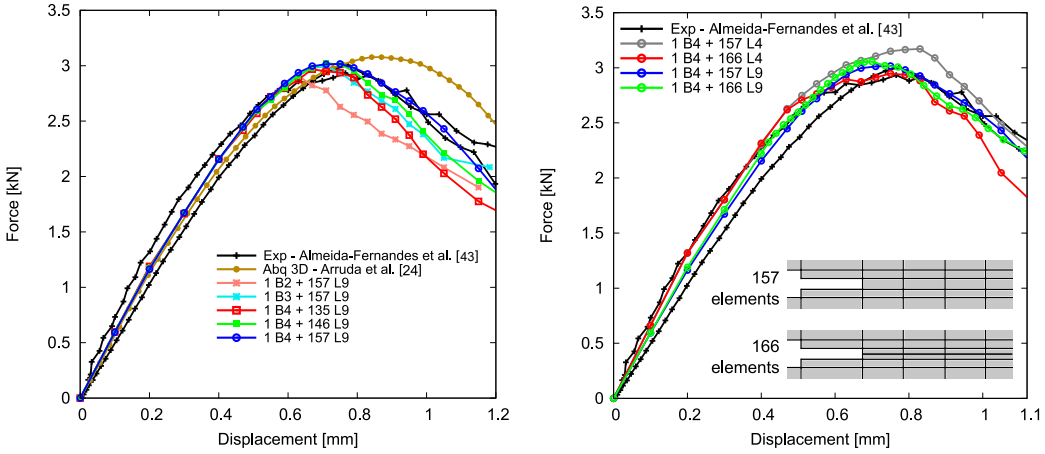

(a) (b)

Fig. 7.7 Convergence analysis of vertical load-displacement in the cross-section (a) and the narrow band (b) for the CT test. Additionally, the discretizations of the cross-section in the notch are depicted.

Table 7.7 Assessing the maximum reaction and vertical displacement within CUF framework and comparison with experimental data and 3D Abaqus outcomes, alongside the DOFs of each model for the compact tension case.

Case	Total DOF	Peak load [kN]	Vertical displacement at peak [mm]
Reference solutions			
Exp 1 - Almeida-Fernandes et al. [148]	-	2.933	0.763
Exp 2 - Almeida-Fernandes et al. [148]	-	3.009	0.776
3D Abaqus - Arruda et al.[107]	66900*	3.075	0.834
Present 1D CUF models			
1D CUF 1 B2 + 157 L9	4818**	2.906	0.629
1D CUF 1 B3 + 157 L9	6885**	3.000	0.689
1D CUF 1 B4 + 135 L9	7848**	3.022	0.710
1D CUF 1 B4 + 146 L9	8400**	3.025	0.730
1D CUF 1 B4 + 157 L9	8952**	3.025	0.730
1D CUF 1 B4 + 157 L4	3420**	3.179	0.810
1D CUF 1 B4 + 166 L4	3540**	2.959	0.770
1D CUF 1 B4 + 166 L9	9408**	3.056	0.700

*Symmetric along y-direction
**Full structure

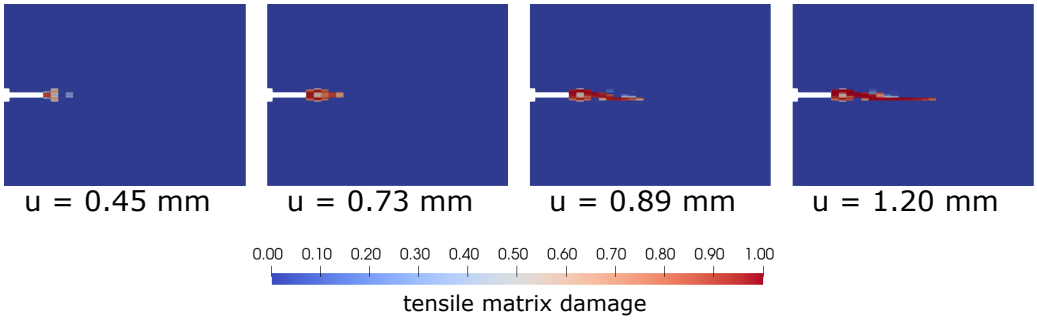

Fig. 7.8 Progression of tensile matrix damage in the narrow band for the case with 1 B4 + 157 L9 for the compact tension case.

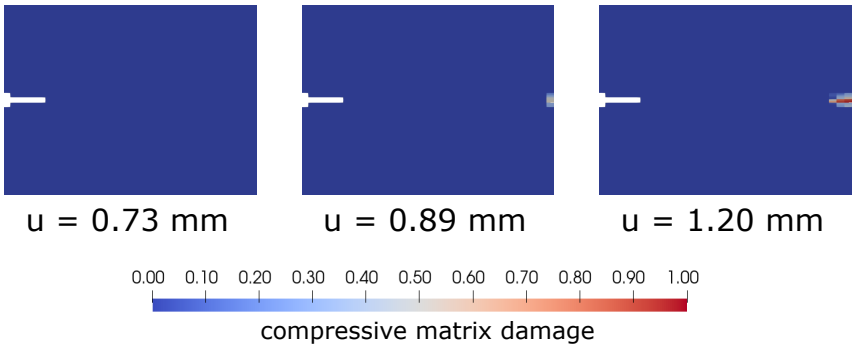

Fig. 7.9 Progression of compressive matrix damage in the narrow band for the case with 1 B4 + 157 L9 for the compact tension case.

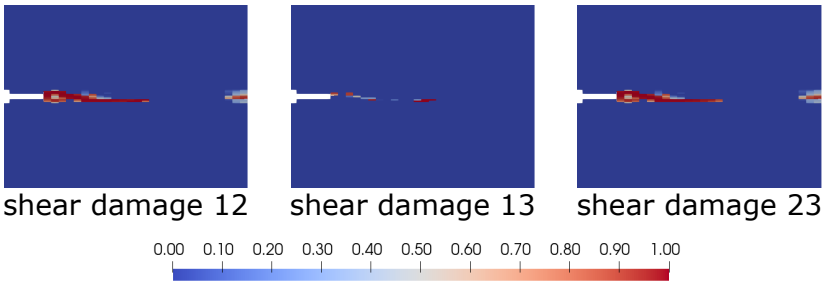

Fig. 7.10 The ultimate distribution of shear damage within the narrow band in the scenario featuring 1 B4 + 157 L9 elements for the compact tension case.

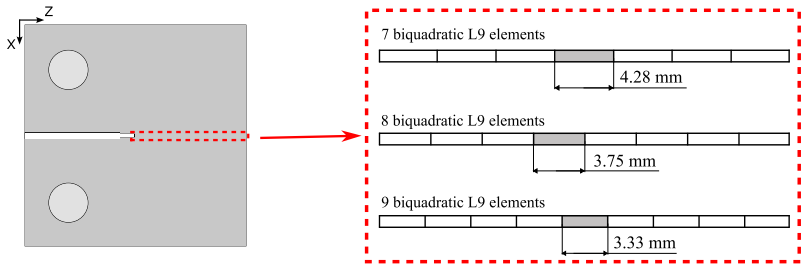

Fig. 7.11 Number of expansion sets within the narrow band for the CT coupon, considering the width of a single element.

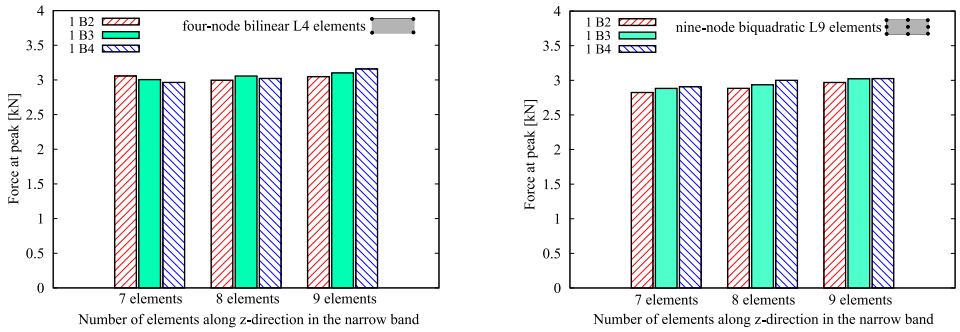

(a) (b)

Fig. 7.12 Sensitivity analysis of FEM mesh and structural theory for the cross-section of the CT with (a) 4-node L4 elements and (b) 9-node L9 elements..

chosen type or distortion of finite elements. In 1D CUF, sensitivity assessment should take into account: (i) the finite element mesh along the y-direction, incorporating linear, quadratic, and cubic finite elements, specifically 2-node B2, 3-node B3, and 4-node B4; and (ii) across the cross-section, where the selection is between 4-node bilinear L4 expansions and 9-node biquadratic L9 expansions. Consequently, in CUF, mesh sensitivity pertains to the influence of FEM elements operating along the y-direction, while sensitivity of structural theory can be contemplated for the cross-section. To explore mesh sensitivity within the narrow band where damage occurs, three different sets of expansions - 7, 8, and 9 elements - are employed along the z-direction, with the width of each element depicted in Fig. 7.11. Figure 7.12a illustrates the variation in peak load using 4-node bilinear elements for the cross-section as the number of beam elements increases, resulting in decreased width; the same histogram is depicted in Fig. 7.12b with 9-node biquadratic elements for the cross-section. The sensitivity of the structural theory is further investigated by varying the order of the elements over the cross-section while fixing both the size of the elements in the narrow band and the FEM discretization. Table 7.8 presents the

Table 7.8 Forecasted maximum load for each element mesh size within the narrow band, altering the structural theory and type of FEM element for the compact tension case.

Structural theory	FEM element	Peak load [kN]		
		7 elements	8 elements	9 elements
Bilinear L4	B2	3.057	3.005	2.964
	B3	2.996	3.056	3.021
	B4	3.097	3.161	3.179
Biquadratic L9	B2	2.824	2.883	2.907
	B3	2.884	2.936	3.000
	B4	2.969	3.022	3.025

Table 7.9 Percentage difference between the peaks achieved with L4 and L9 for various element sizes in the narrow section, as the order of the FEM element varies along the y-direction.

FEM element	Percentage variation		
	7 elements	8 elements	9 elements
B2	7.9%	4.1%	1.9%
B3	3.8%	4.0%	0.7%
B4	4.2%	4.5%	4.9%

forecasted peak load, while Table 7.9 outlines the percentage deviation among the structural theories for each FEM discretization. When considering the biquadratic L9 as the structural theory, one can examine the impact of mesh size within the narrow band. The diminishing trend of the percentage variation is depicted in Fig. 7.13 as the order of FEM discretization increases.
By observing the results and assuming the case of 1 B4 + 157 L9 as CUF reference, the following observations can be made:

1. The convergence analysis indicates that employing cubic elements for the thickness yields satisfactory agreement with experimental curves, even with a coarser cross-section discretization. Additionally, the CUF framework demonstrates superior cost-effectiveness compared to 3D Abaqus while maintaining significant accuracy in peak detection and softening path determination.

2. Figure 7.7a illustrates that CUF results exhibit a softening branch behavior more closely aligned with experimental observations compared to 3D Abaqus. The current approach utilizes the cubic root of the Gauss point volume associated with each element as the characteristic length, in contrast to the square

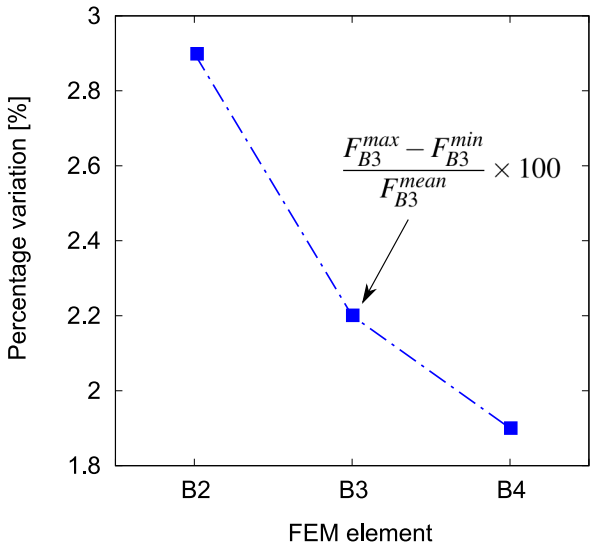

Fig. 7.13 Percentage variation of peak load for L9 structural theory with various FEM elements.

root of the numerically calculated surface area employed in Arruda et al. [107]. Moreover, the current implementation incorporates higher order kinematic theories compared to the Abaqus framework.

3. Comparison of the maximum reaction in Table 7.7 reveals that the reference CUF maximum force exceeds mean experimental values by 1.82%, demonstrating greater accuracy than 3D Abaqus. However, the vertical displacement at peak in CUF outcomes is 2.5% smaller than mean experimental displacements. Furthermore, the number of degrees of freedom (DOF) utilized within the CUF framework is significantly lower than that in the study by Arruda et al. [107], resulting in reduced computational costs.

4. Analysis of the shear damage distribution indicates occurrences of both fiber and interlaminar damages, albeit their significance is minor compared to matrix damage evolution. The 3D damage model facilitates extraction of damage evolution in the transversal out-of-plane y-direction, a capability previous 2D damage models lacked.

5. Sensitivity analysis reveals that slight differences in peak detection can arise when employing quadratic or cubic FEM elements along the y-direction, with a biquadratic discretization of the cross-section, as depicted in Fig. 7.12b.

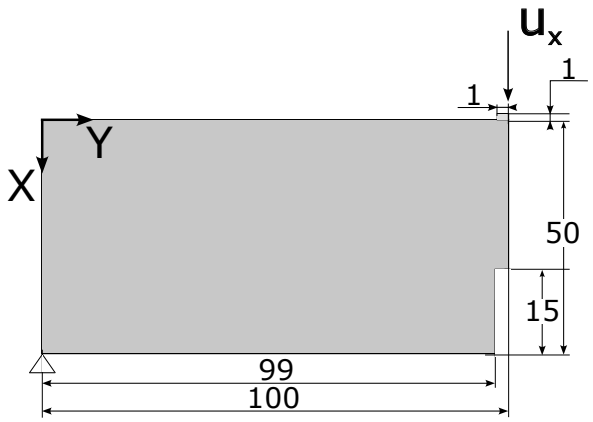

Fig. 7.14 Dimensions in mm of the specimen for the three-point bending case, along with boundary conditions.

6. Structural theory sensitivity analysis indicates minor sensitivity when utilizing 4-node B4 elements for FEM discretization, which remains relatively constant across different mesh sizes in the narrow band. Conversely, for cases employing B2 and B3, reducing the size of narrow section elements leads to a significant decrease in structural theory sensitivity, as shown in Table 7.9. However, Fig. 7.13 illustrates that employing higher-order elements substantially reduces the mesh-size dependency for predicting peak load..

7.1.3 Three-point bending beam

This investigation aims to analyze the damage evolution in a three-point bending GFRP beam with a notch at the midspan. To mitigate analysis costs, the numerical simulation focuses solely on a quarter of the beam, with the corresponding geometry depicted in Fig. 7.14. FE models with B2, B3, and B4 finite elements operate along the y-direction of the beam, whereas the cross-section discretization comprises biquadratic L9 expansion elements, as illustrated in Fig. 7.15. Table 7.10 lists the adopted material properties, based on [106, 107], with fibers oriented along the x-direction, and Tables 7.11 and 7.12 detail the damage properties. The beam is simply-supported, with a steel support applying vertical displacement, following the methodology employed in [107].

Five analysis cases are investigated, employing various discretizations for both axial and cross-sectional domains. Table 7.13 outlines the number of FEM elements and their respective discretization for section A-A (see Fig. 7.15). Figure 7.16

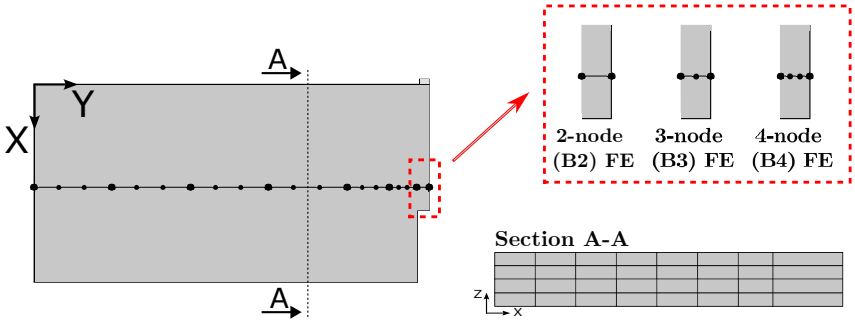

Fig. 7.15 Finite element mesh along the y-direction for the three-point bending case, featuring magnification in the narrow section, alongside an illustrative example of in-plane discretization for section A-A.

Table 7.10 Material characteristics of the GFRP material utilized in the three-point bending beam and the steel support expressed in the material reference system.

E_{11} [GPa]	E_{22} [GPa]	E_{33} [GPa]	G_{12} [GPa]	G_{13} [GPa]	G_{23} [GPa]	ν_{12} [-]	ν_{13} [-]	ν_{23} [-]
30.00	11.38	11.38	3.00	3.00	3.00	0.24	0.24	0.4

Table 7.11 Longitudinal, transverse, interlaminar and shear strength of the GFRP material for the three-point bending case.

X_T [MPa]	X_C [MPa]	Y_T [MPa]	Y_C [MPa]	Z_T [MPa]	Z_C [MPa]	S_L [MPa]	S_T [MPa]	S_I [MPa]
323.00	426.00	37.00	80.00	37.00	80.00	33.00	33.00	33.00

Table 7.12 Fracture energies of the pultruded GFRP for the three-point bending case.

G_{ft} [MPa·mm]	G_{fc} [MPa·mm]	G_{mt} [MPa·mm]	G_{mc} [MPa·mm]	G_{it} [MPa·mm]	G_{ic} [MPa·mm]
130.00	130.00	3.84	3.84	3.84	3.84

Table 7.13 FEM and cross-section discretizations for five distinct analysis scenarios concerning the three-point bending case.

	FEM discretization	Cross-section discretization (A-A)
Case A	7 B4	150 L9
Case B	6 B4+1 B3	64 L9
Case C	6 B4+1 B2	32 L9
Case D	6 B4+1 B2	24 L9
Case E	6 B4+1 B2	16 L9

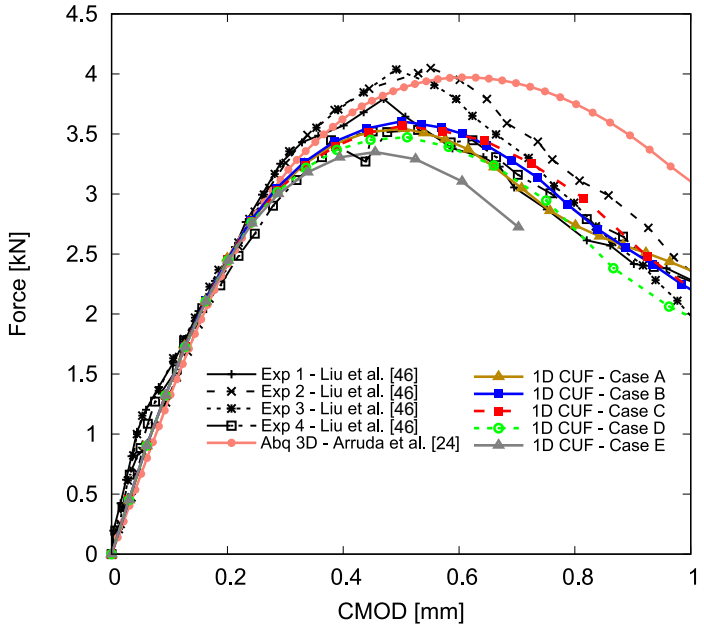

Fig. 7.16 Vertical load versus CMOD for the three-point bending case.

presents vertical reaction-crack mouth opening displacement (CMOD) curves of CUF results, an Abaqus 3D employing C3D8 elements [107], and experimental data [151]. Furthermore, a detailed comparison of maximum reaction force, CMOD, and numerical DOF is presented in Table 7.14. Finally, Fig. 7.17 depicts the evolution of the tensile matrix damage during the analysis, while Fig. 7.18 showcases the ultimate distribution of some representative damage modes. 7.18.
Assuming case C as the CUF reference, the results suggest that:

1. Examination of Fig. 7.16 highlights that implementing the Hashin damage model within the CUF framework yields results more closely aligned with experimental data compared to the user-subroutine UMAT in Abaqus. Both CUF and 3D Abaqus accurately predict the pre-peak branch of the force-

Table 7.14 Assessment of the maximum reaction and CMOD within CUF and their comparison with experimental data and 3D Abaqus results, along with the total DOFs of each model for the three-point bending case.

Case	Total DOF	Peak load [kN]	CMOD at peak [mm]
Reference solutions			
Exp 1 - Liu et al. [151]	-	3.800	0.474
Exp 2 - Liu et al. [151]	-	4.040	0.556
Exp 3 - Liu et al. [151]	-	4.030	0.498
Exp 4 - Liu et al. [151]	-	3.530	0.458
3D Abaqus - Arruda et al. [107]	381270	3.971	0.623
Present 1D CUF models			
1D CUF Case A	36735	3.605	0.500
1D CUF Case B	15504	3.544	0.504
1D CUF Case C	7803	3.567	0.503
1D CUF Case D	6069	3.472	0.511
1D CUF Case E	4335	3.348	0.455

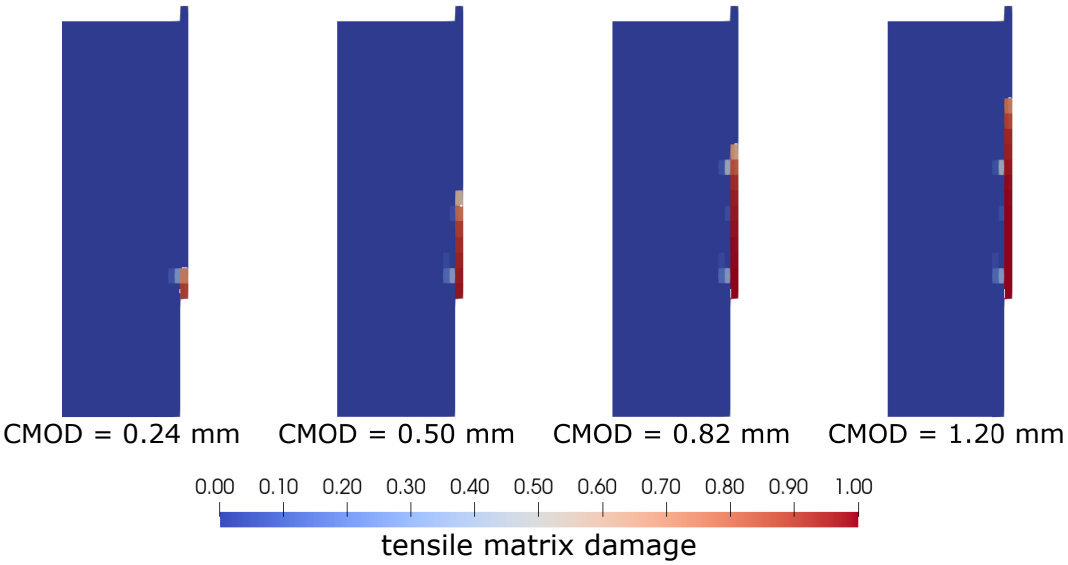

Fig. 7.17 Progression of tensile matrix damage within the notch for case C of the three-point bending case.

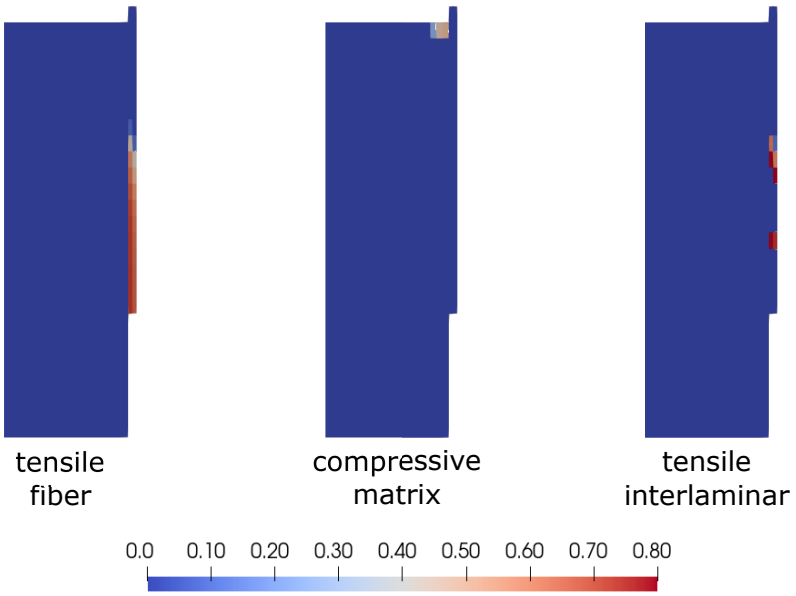

Fig. 7.18 The ultimate distribution of tensile fiber, compressive matrix and tensile interlaminar damage for case C of the three-point bending beam.

CMOD plot, with only CUF capable of forecasting the subsequent softening. Moreover, similar observations to those made in the preceding section can be drawn regarding the disparities between CUF and 3D Abaqus outcomes.

2. The utilization of CUF facilitates a notable reduction in computational costs, given its significantly lower number of DOF compared to Abaqus, as indicated in Table 7.14. Furthermore, the maximum reaction obtained using CUF is 3.5% lower than the mean experimental peak, while the CMOD at peak for CUF results is 2.2% larger than the mean reference [151].

3. Fig. 7.18 vividly illustrates the occurrence of fiber, matrix, and interlaminar damages. Additionally, the current model captures certain three-dimensional effects that eluded previous 2D models [106].

7.2 Static and progressive failure analysis through coupled FEM-PD models

7.2.1 Comparison of coupling methods by static analysis of square cross-section beam

The first case study considers a 3D isotropic beam under traction load. Geometrical and modelling features are shown in Fig. 7.19. The bar has a square cross-section, with side equal to 10 mm, whereas the beam's axial length equals 100 mm. The material has an elastic modulus $E = 10$ GPa and Poisson's ratio $\nu = 0.2$. The central segment of the isotropic bar is simulated using a 3D peridynamic grid. A grid spacing of $\Delta x = 1$ mm and an m-ratio of 3 are employed, yielding a horizon radius of $\delta = 3$ mm. A state-based formulation is utilized. The remaining sections of the beam are represented by B2 FEs, with one element allocated to each region. Thus, within the Carrera Unified Formulation (CUF), the kinematics associated to the FE spans from classical beam models to higher-order Lagrange expansions (LE). Specifically, Taylor expansions of different orders N (TEN) are adopted. For example, the notation TE1 refers to the use of first-order polynomials as an expansion function. Additionally, nine-node quadratic Lagrange elements (LE9) are utilized. In this assessment, the aim is to compare the two coupling approaches. This bar was previously studied in [152], where the coupling method employed Lagrange multipliers at the FEM-PD interface. The results of this investigation were found to be in good agreement with the full FEM solution. However, some discrepancies at the interface were observed. The solutions obtained from the smeared coupling method are compared with those obtained using the Lagrange multipliers approach.

The initial result is illustrated in Fig. 7.20, showing the deformed shape of the bar under uniaxial displacement. In this scenario, a single LE9 element is employed for cross-section discretization. Figure 7.21 demonstrates the consistency of solutions when 3D PD is coupled with different FE models. Notably, the discretization of the cross-section does not impact the longitudinal displacement evaluated at the central point of the section along the bar length. Comparison between the two coupling methods is presented in Fig. 7.22. This comparison reveals distortions in displacement at interface regions when the Lagrange multipliers method is utilized (refer to Fig. 7.22b). Conversely, as depicted in Fig. 7.22c, these discrepancies

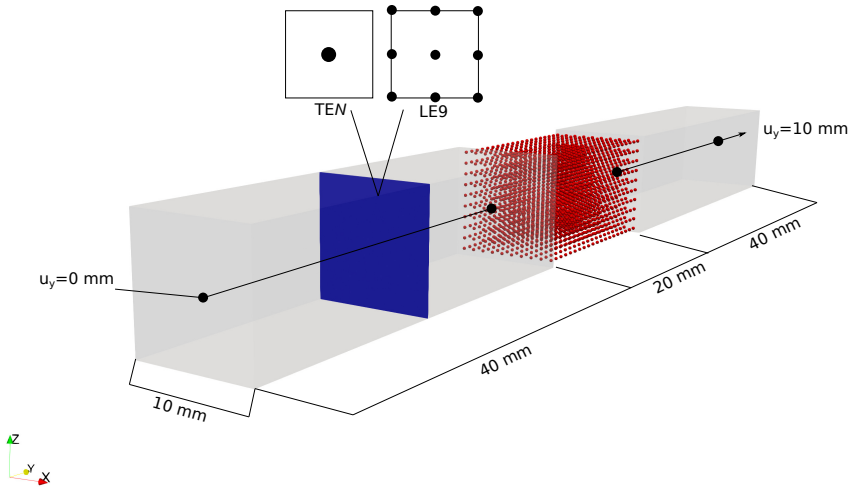

Fig. 7.19 Geometrical and modelling properties.

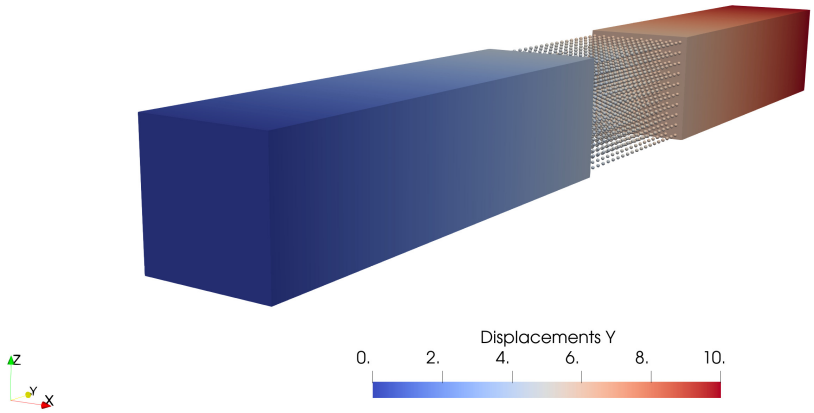

Fig. 7.20 Deformed shape of the beam. The one-dimensional FEs adopt here a quadratic (L9) kinematics. The Lagrange multipliers coupling method is employed.

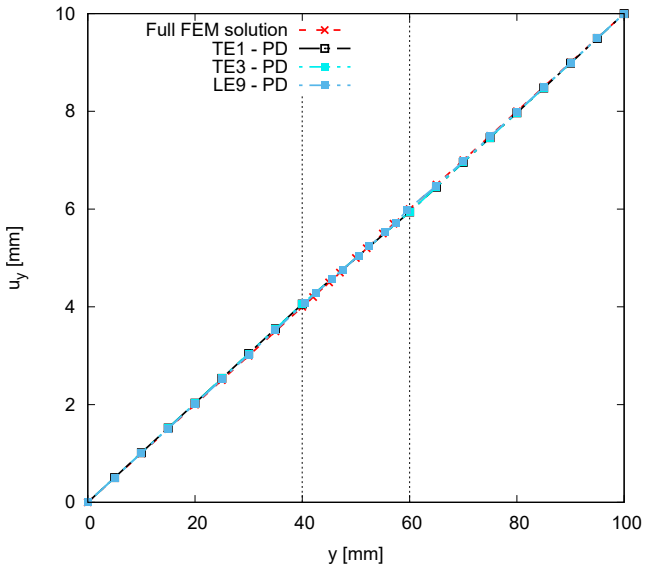

Fig. 7.21 Influence of various 1D-CUF models for FEM regions on the longitudinal displacement.

are nearly eradicated when the smeared method is employed, particularly at the interfaces. Specifically, a relative error exceeding 5% is computed at the FEM-PD interfaces with the Lagrange multipliers method. In contrast, the smeared coupling technique significantly reduces the error, resulting in a maximum relative error of 0.69%.

7.2.2 Static analysis of a C-shaped beam

The second case study involves a C-section beam subjected to bending and torsion, as detailed in Fig. 7.23. The beam is made of the same isotropic material of the previous case, with an elastic modulus of $E = 200$ GPa and a Poisson ratio of $\nu = 0.2$. In this analysis, the smeared coupling approach is utilized. The primary objective of this case study is to emphasize the three-dimensional nature of the proposed coupling model, which applies to both coupling approaches. High-order LE elements are essential for accurately depicting the behavior of the beam under bending and torsion. It has been extensively demonstrated that classical low-order beam theories encounter significant challenges in reproducing these three-dimensional phenomena. In this case study, the axial FEM discretization comprises 10 four-node cubic elements (B4). Differently from the previous case, the entire cross-section is not modeled using 3D PD. Instead, the PD region is embedded within the finite element domain. This

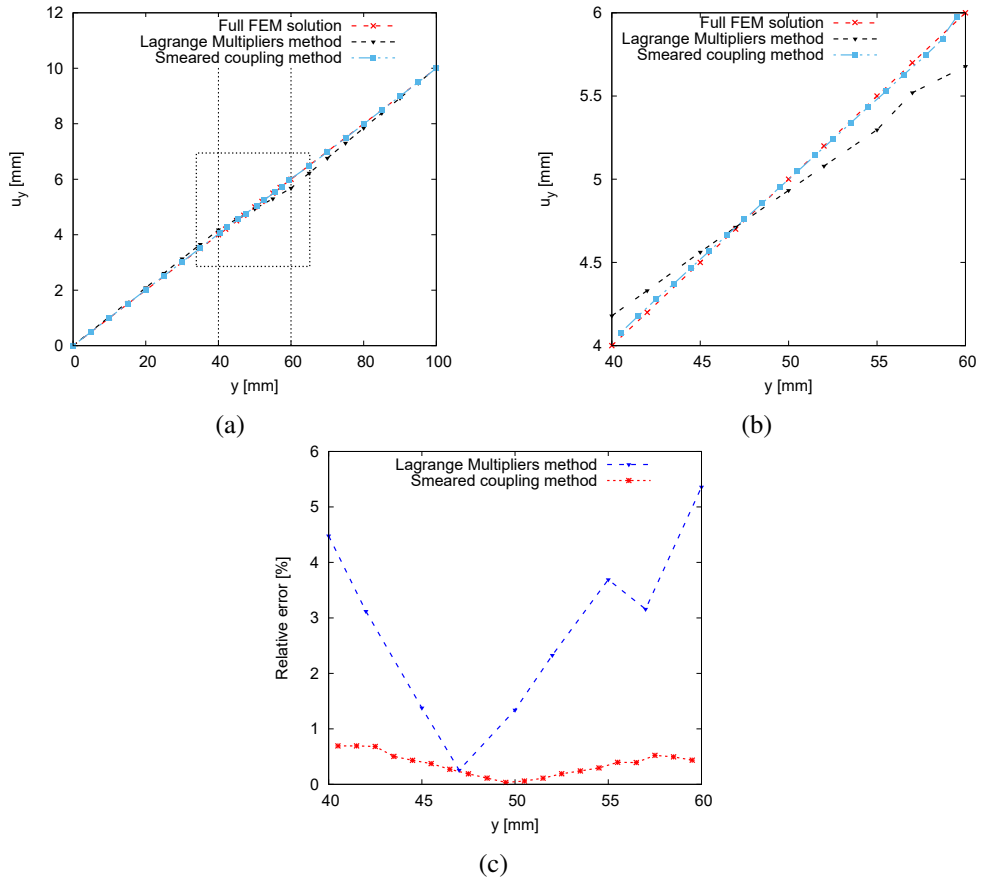

Fig. 7.22 Longitudinal displacement of the bar under tensile loading along a) its entire length and b) the peridynamic region. When employing the Lagrange multipliers coupling approach at the FE-PD interfaces, distortions occur. However, tthese distortions are rectified when employing the smeared coupling method. A comparison of the errors relative to the full finite element solution obtained with both methods is illustrated in (c).

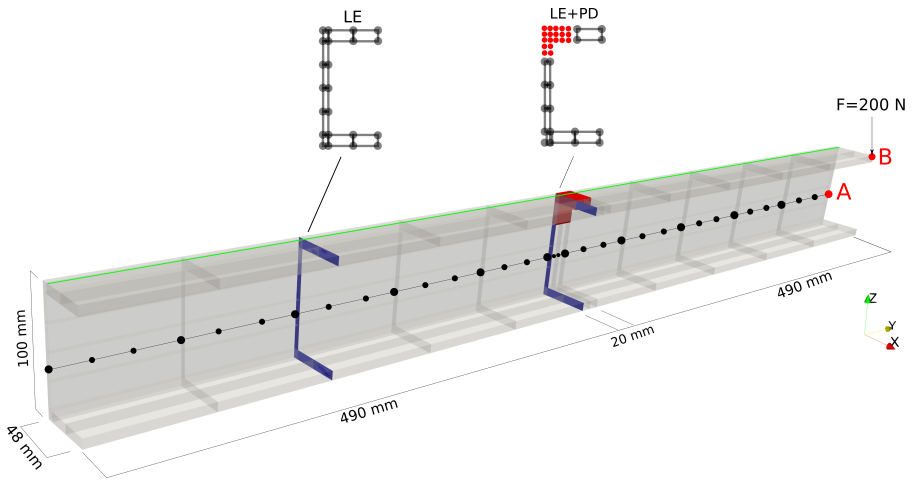

Fig. 7.23 Geometrical and modelling properties of C-shaped section beam.

Model	FE dof's	PD dof's	-u_z [mm] Point A	-u_z [mm] Point B
TE1	333	-	0.1713	0.1732
TE4	1665	-	0.1959	0.2658
TE8	4995	-	0.2646	0.5252
L9	9657	-	0.2403	0.5436
L9-PD	9432	20040	0.2344	0.5337

Table 7.15 Transverse displacements at the midpoint of the free-end section (Point A) and at the load application point (Point B).

is achieved by adjusting the cross-section of the 1D FEs along the axial direction, resulting in a disconnected region wherever PD is employed, specifically $490 \leq y \leq 510$ mm (refer to Fig. 7.23). A grid spacing of $\Delta x = 1$ mm and horizon radius $\delta = 3$ mm are selected. The deformed shape of the C-section beam for both the full FEM (Fig. 7.24 (a)) and the coupled PD-FEM model (Fig. 7.24 (b)) is depicted in Fig. 7.24. Additionally, a closer view of the deformed state is provided in Fig. 7.25. It can be observed that the three-dimensional PD domain aligns perfectly with the FEM regions. These considerations validate the use of high-order Lagrange elements capable of capturing 3D-like phenomena. Table 7.15 compares the vertical displacements at points A and B (refer to Fig. 7.23) obtained from the smeared coupled FE-PD model with those from reference solutions obtained using CUF-based TE and LE refined models. Displacements at two different points are evaluated to further illustrate the capability of the refined CUF models to capture both the bending and torsional behavior of the investigated beam. A notable observation is the challenge faced by low-order theories in accurately computing displacements at both investigated points. The model employing LE9 elements for cross-section discretization achieves an optimal solution, consistent with findings from recent works (e.g., [153]). Furthermore, the smeared coupling model yields transverse displacements comparable to those obtained with fully refined models, with errors of 1% and 2% detected at points A and B, respectively. Finally, the vertical displacement along the beam span is presented in Fig. 7.26, with the green line indicating the path followed. Results from the current coupled model are compared with a full FEM solution. The displacement evolution along the beam span is accurately captured by the FEM-PD model. Additionally, it is important to highlight the coupled solution's ability to maintain smooth transitions at domain interfaces, as evident from the continuous variation between FEM (red dots) and PD (green dots) displacements. However, residual errors that remain visible in Fig. 7.26 stem from

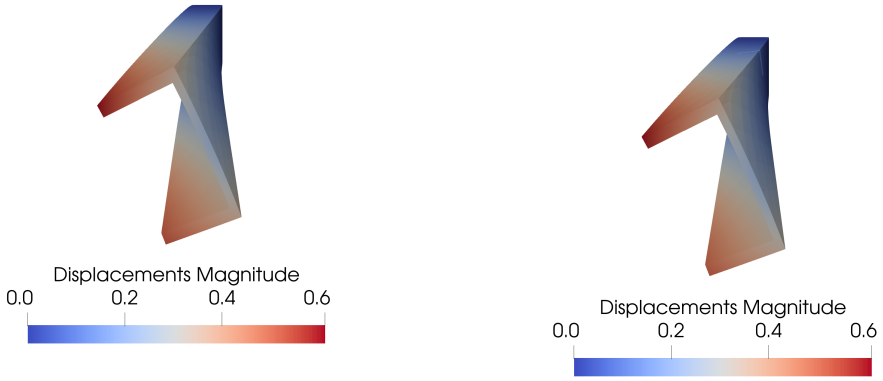

(a) Full FEM model

(b) FE-PD coupled model

Fig. 7.24 Deformed configuration of the C-section beam for FEM and FE-PD coupled model.

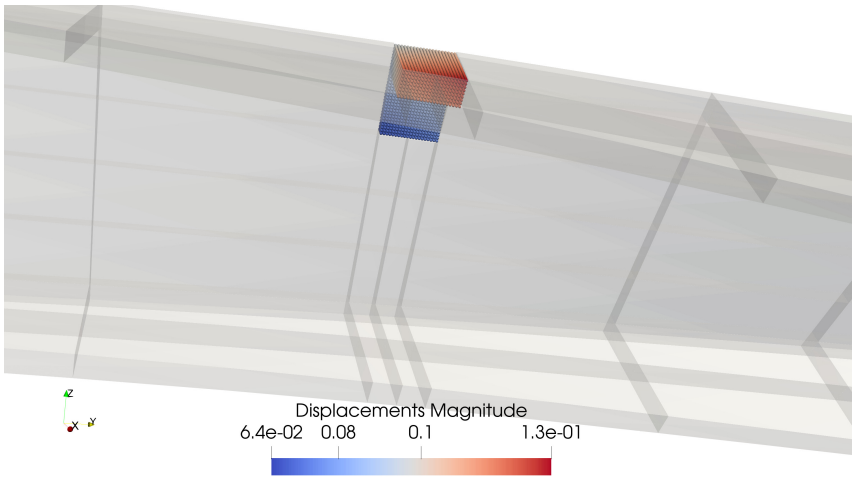

Fig. 7.25 Close view of the deformed PD region for the examined case, demonstrating a significatn consistency between the two formulations.

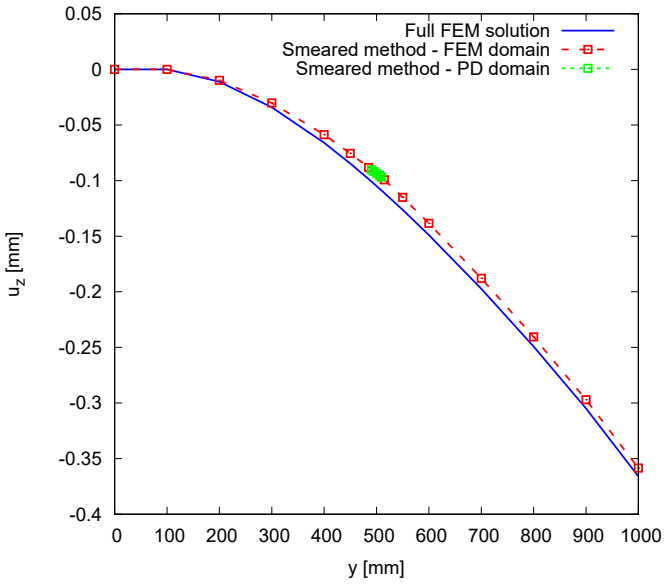

Fig. 7.26 Displacement in z-direction along its span (indicated by the green line in Fig. 7.23). A full FEM solution (solid blue line) serves as reference, whereas the displacement in the FEM and PD domains is denoted by red and green dots, respectively.

the inherent differences between the local and nonlocal solutions of Peridynamics and CUF when the displacement field is a superlinear function [138]. Furthermore, the absence of corrections for the peridynamic surface effect may further contribute to the discrepancies between the results obtained with the full FEM approach and the CUF-PD coupling.

7.2.3 Static analysis of a reinforced aeronautical panel

A stiffened panel is examined as an additional example to highlight the capability of the proposed method to incorporate PD domains into complex structures. Figure 7.27 provides an overview of the geometric and modeling characteristics. The material properties remain consistent with those adopted in Section 7.2.1. The structure consists of two stringers and one panel, each independently modeled using high-order four-node beam elements in a component-wise manner [154]. One of the main novelties introduced in this numerical case is the opportunity to explore a structure featuring two distinct peridynamics domains. Specifically, two separate square regions, one for each stringer, are modelled using 3D peridynamics. The PD domain is discretized in a meshless manner with a grid spacing of $\Delta x = 1$ mm and a horizon radius $\delta = 3$ mm. Table 7.16 presents the vertical displacement and

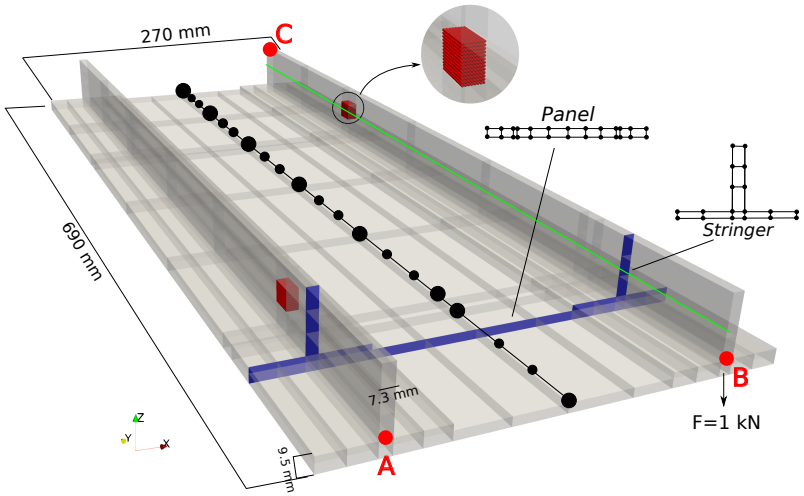

Fig. 7.27 Geometric and modeling characteristics of the analyzed reinforced panel. Two separate peridynamic regions are incorporated, each corresponding to a stringer.

Model	FE dof's	PD dof's	$-u_z$ [mm] @Point A	$-u_z$ [mm] @Point B	σ_{yy} [MPa] @ Point C
TE1	225	-	29.532	29.368	71.274
TE4	1125	-	31.471	27.513	89.505
TE8	3378	-	40.765	18.396	114.42
L9	10659	-	44.942	14.153	126.916
L9-PD	10641	15480	45.346	14.719	126.847

Table 7.16 Vertical displacements and longitudinal stress σ_{yy} are assessed at specific points of interest within the structure for both the reference solutions and the current FE-PD coupled model.

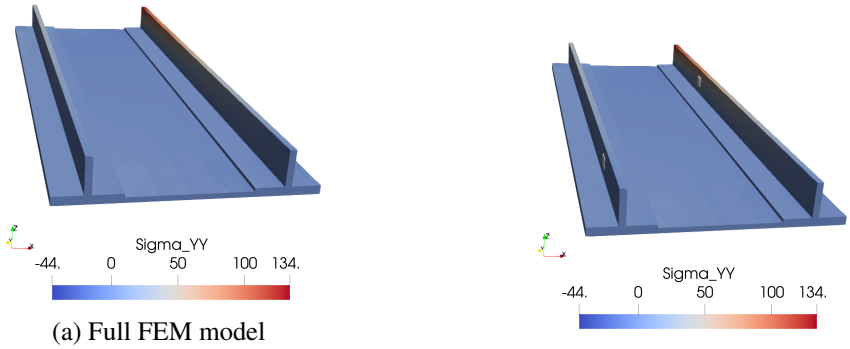

(a) Full FEM model

(b) Coupled FE-PD model

Fig. 7.28 Distribution of longitudinal stress σ_{yy} in the reinforced panel from a full FEM analysis and from a coupled FE-PD model.

the longitudinal stress σ_{yy} values at specific points (see Fig. 7.27) for both the current coupled model and reference solutions obtained through full FEM analysis. These findings once again underscore the effectiveness of the proposed coupling model in accurately capturing three-dimensional phenomena. Moreover, it's worth highlighting the precise prediction of axial stress at point C within the structure. Figure 7.28 also illustrates the complete axial stress distribution within the structure, comparing the FEM solution (Fig. 7.28a) with the coupled model (Fig. 7.28b). It's noteworthy that the presence of the PD domain embedded within the structure does not disrupt the stress distribution, indicating the potential utility of FEM-PD coupled models for fracture mechanics applications (as discussed in [41]).

Vertical deflection along the green line in Fig. 7.27 is depicted in Fig. 7.29. The solution derived from a complete FEM analysis is illustrated by a solid blue line, while red and green dots represent deflections in the FEM and PD domains, respectively. The coupled model perfectly aligns with the FEM solution along the beam span and across the peridynamic region, with no indication of distortion at either the FE-PD interfaces. As observed in the previous scenario, residual errors arise from the distinct formulations of peridynamics and CUF theories.

7.2.4 Progressive failure analysis of a pre-cracked beam under uniaxial load

The first case study focusing on crack propagation involves a pre-cracked beam subjected to uniaxial tension, as depicted in Fig. 7.30. The beam is 200 mm long

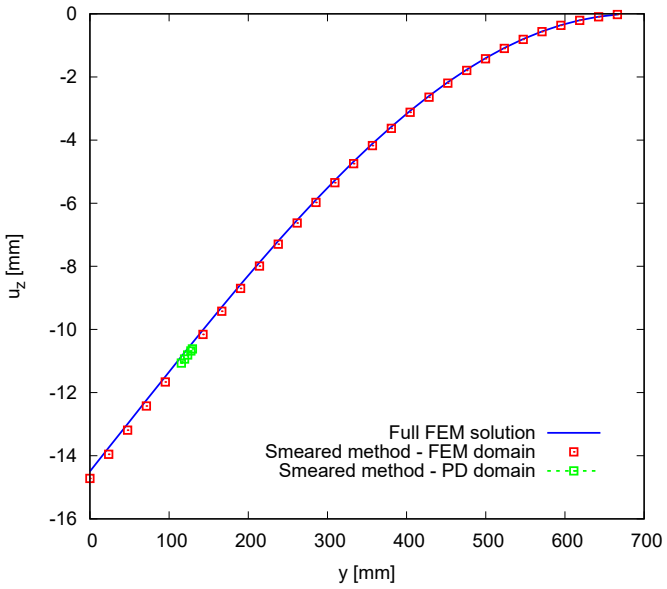

Fig. 7.29 Vertical displacements along the span of the structure, as indicated by the green line in Fig. 7.27. A FEM solution (solid blue line) serves as a reference, while the displacement in the FEM and PD domains is represented by red and green dots, respectively.

and has a rectangular cross-section with sides measuring 40 mm and 100 mm. Steel plates, each 5 mm thick, are placed at both ends to facilitate load application and boundary conditions. A crack, 4 mm wide, is positioned at the bar's center. The plate located at $y = 0$ is clamped, while the end plate undergoes axial displacement. The bar is made of a homogeneous isotropic material with Young modulus E = 32 GPa. The Poisson's coefficient is $\nu = 0.25$ in the peridynamic domain. The value of the critical energy release rate G_0 is $60\,N/m^2$. The peridynamics grid occupies the central region of the bar, spanning from $y = 60$ mm to $y = 140$ mm. The remaining sections are modeled using CUF-based finite elements. Along the longitudinal axis, four two-node linear finite elements (B2) are utilized, two for the steel plates and two for the bar. The cross-section employs a single L9 element for discretization, a choice validated for similar traction problems in previous research [155]. Nevertheless, TE models are also employed to assess the influence of 1D theory on model accuracy. In the reference study, progressive failure within the structure is explored using cohesive and bulk elements. In this work, the assumption that the crack initiates and propagates solely within the peridynamics domain is made. In Fig. 7.30, a crack is simulated by removing PD nodes, just for explicative reasons. However, in the current model, the crack is formed by removing bonds between the two edges of the open surface, as depicted in Fig. 7.31. Consequently, the particles involved

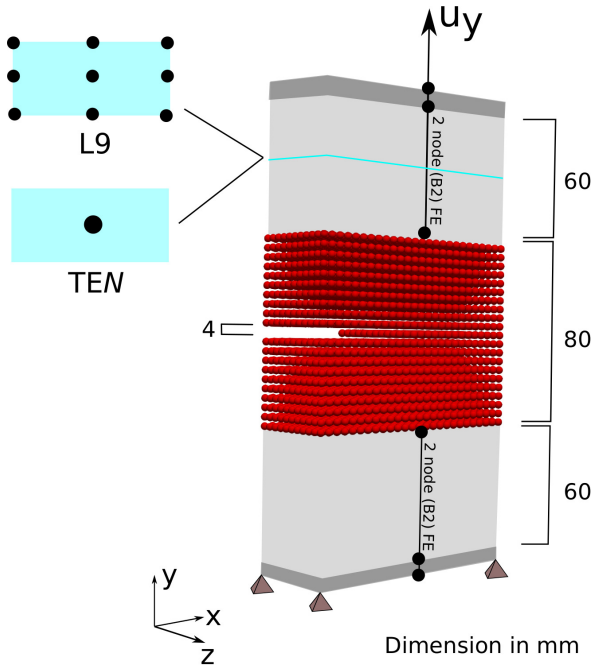

Fig. 7.30 Geometry and boundary conditions of the traction bar.

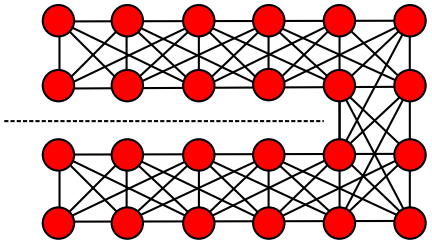

Fig. 7.31 Visual representation of crack opening by removing the affected bonds.

will possess fewer initial bonds compared to their neighbours, resulting in reduced stiffness and creating a plausible zone for crack initiation. As outlined in Section 3.2, a series of sequentially linear analyses were conducted by incrementally applying displacement and updating the scalar functions μ based on the bond stretch criterion. The progression of the crack pattern is depicted in Fig. 7.32, where the damage index φ for each particle is presented at four distinct simulation stages. The evolution of φ indicates the crack propagating parallel to the pre-existing crack, consistent with experimental observations and numerical simulations. Figure 7.33a displays the curves of CMOD versus forces for various cases. The numerical reference curve is sourced from [156], where the authors incorporated a model comprising cohesive elements and plasticity. The other curves are derived from the FEM-PD coupling

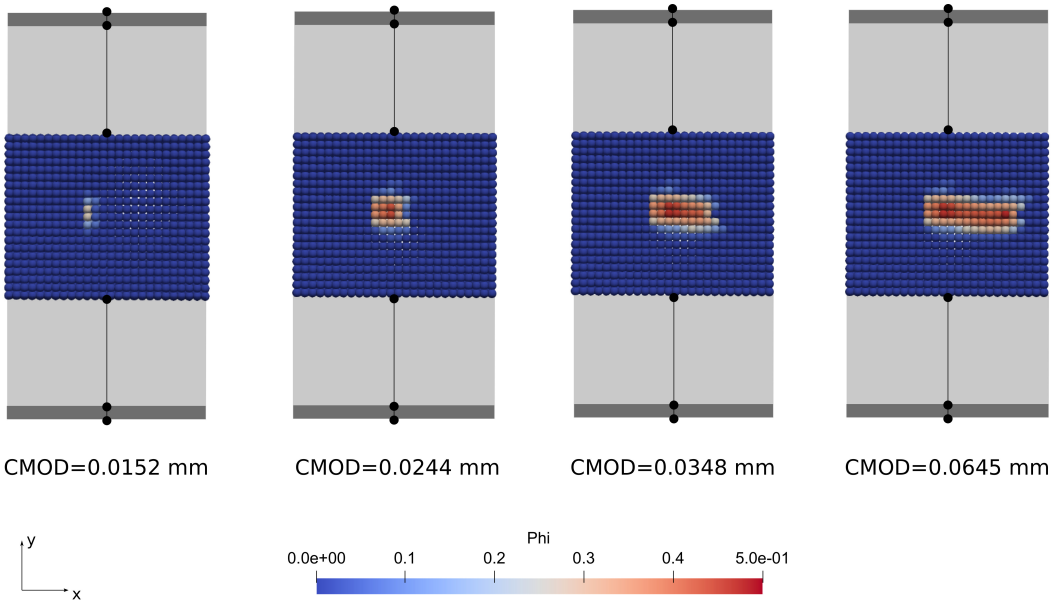

Fig. 7.32 Progression of the damage index φ, providing insights into the propagation of cracks.

Case	$\Delta x\,[mm]$	Horizon $\delta\,[mm]$	FEM DOFs	PD DOFs	Peak load [N]	CMOD [mm]
Numerical Reference	-	-	30672	-	5700	0.017
L9 - 3D PD	2	6	162	131733	7191	0.0193
L9 - 3D PD	2	8	162	131733	5544	0.014
L9 - 3D PD	4	12	162	18018	5986	0.0156
L9 - 3D PD	4	16	162	18018	5020	0.015

Table 7.17 Significant parameters for both the reference and simulation scenarios, varying grid spacing Δx, and horizon radius δ.

method utilizing Lagrange multipliers. The influence of grid spacing Δx and horizon radius δ on CMOD and peak load was examined, with the corresponding curves presented in Fig. 7.33a. A summary of the peak loads and their corresponding CMODs is provided in Table 7.17. The initial observation highlights a significant dependency of the peak load on the peridynamics parameters. When comparing two simulations with a fixed grid spacing Δx while adjusting the horizon radius, a notable variation in the failure load value emerges, whereas the CMOD calculated at this stage exhibits minimal differences. Specifically, increasing δ results in a reduction of the peak load. However, more detailed convergence analyses, as those outlined in [157], were not conducted as they lie beyond the scope of this study. The simulations closest to the numerical reference are those with $\Delta x = 2$ mm and $\delta = 4\Delta x = 8$ mm, and $\Delta x = 4$ mm and $\delta = 3\Delta x = 12$ mm. Both sets of failure

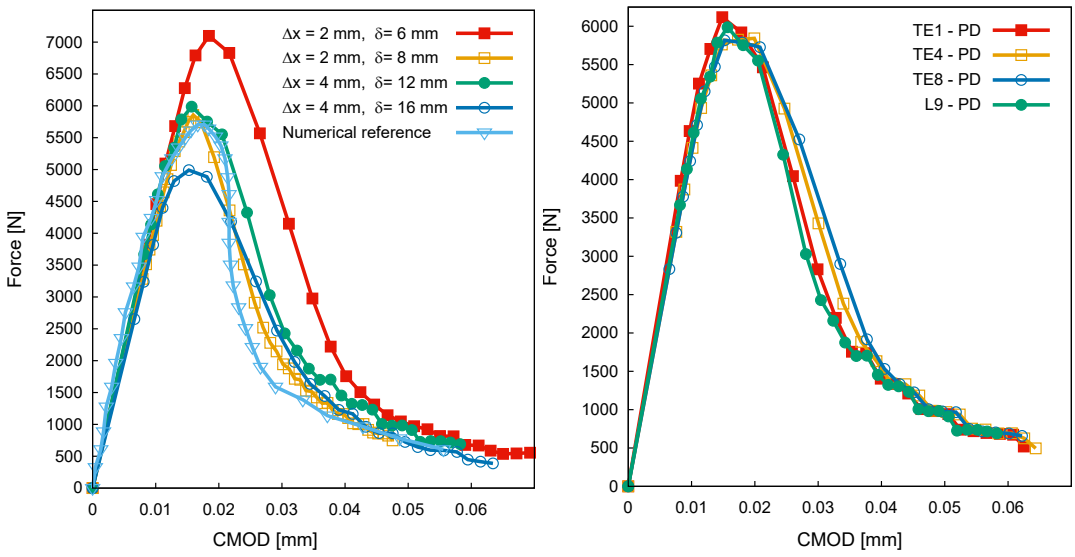

(a) (b)

Fig. 7.33 CMOD-force curves: (a) Influence of grid spacing Δx and horizon radius δ on the current L9-PD model, along with a comparison to numerical findings [156]; (b) Assessment of various 1D-CUF models for FEM regions, maintaining a constant grid spacing ($\Delta x = 4$ mm) and horizon radius ($\delta = 12$ mm)

load and CMOD values from these simulations are comparable. Nonetheless, there is an almost order of magnitude difference (18k versus 131k) in the number of peridynamics DOFs between them. This discrepancy demonstrates that halving the grid spacing leads to a significant increase in the number of DOFs. Practically, this implies that a full 3D peridynamic domain could quickly escalate to an impractical number of DOFs, making the problem computationally expensive to solve. Another interesting observation can be made regarding the choice of theory and its relative order used to discretize the FEM region. The CMOD-force curves for different FEM discretizations are depicted in Fig. 7.33b, with fixed grid spacing Δx and

Case	FEM DOFs	PD DOFs	Peak load		CMOD	
			Value [N]	Diff [%]	Value [mm]	Diff [%]
TE1 - 3D PD	54	18018	6176	3.1	0.0152	−2.5
TE4 - 3D PD	270	18018	5981	0.0	0.0161	3.2
TE8 - 3D PD	648	18018	5980	0.0	0.0162	3.8
L9 - 3D PD	162	18018	5986	-	0.0156	-

Table 7.18 Significant parameters for simulation cases featuring different 1D-CUF models for FEM regions. Additionally, the percentage difference of TE models compared to the L9-PD model is presented.

horizon radius δ values of 4 mm and 12 mm, respectively. Table 7.18 presents some key parameters of the simulation, including the failure load and the corresponding CMOD for each case. Additionally, the relative difference with the reference value of the L9-PD simulation is provided. It's noteworthy that these differences are negligible, ranging from a maximum of 3.8% for the CMOD value to practically zero difference for the failure load. These analyses indicate that the solution remains unaffected by the choice of theory for the FE model employed. This conclusion aligns with findings from [155], where simple linear static analyses were conducted.

7.2.5 Progressive failure analysis of a beam under torsion

The second case study involving progressive failure is the so-called Brokenshire test [158]. The whole setup of the test is given in Fig. 7.34. A notched beam is clamped at its extremities by two steel frames, with three loading arms of these frames supported and one loaded with a vertical force or displacement, inducing torsion on the notched beam. These boundary conditions induce a torsion on the notched beam. Unlike the previous symmetric problem, the boundary conditions and pre-existing crack pattern (45° angle) make this problem asymmetrical. Thus, the high tri-dimensionality makes it a hallenging test for the proposed coupled model. The bar is 400 mm long and has a square cross-section with a side length equal to 100 mm, whereas the steel plates have a length of 25 mm. The bar is made of a homogeneous isotropic material with Young modulus E = 35 GPa. The Poisson's coefficient is $\nu = 0.25$ in the peridynamic domain. The value of the critical energy release rate G_0 is $80\,N/m^2$. The peridynamics grid spans from the coordinate $y = 125$ mm to $y = 325$ mm in the central zone of the bar, while the remaining zones are modeled using finite elements. Along the longitudinal axis, two three-node quadratic (B3) elements are allocated for each steel plate, along with a total of four four-node cubic (B4) elements for the bar. The cross-section is discretized using six L9 elements. Sequential linear analysis are then performed. In Fig. 7.35, the value of the damage index φ for most interesting particles at four simulation steps is shown. The distribution of φ gives information about the propagation of the crack. The resulting crack front closely aligns with both experimental findings[159] and previous numerical simulations [156, 160–162]. Additionally, Fig. 7.36 presents a comparison of the damage distribution between a plasticity-damage model [162] and the current model. Notably, the crack pattern observed from the bottom of the beam

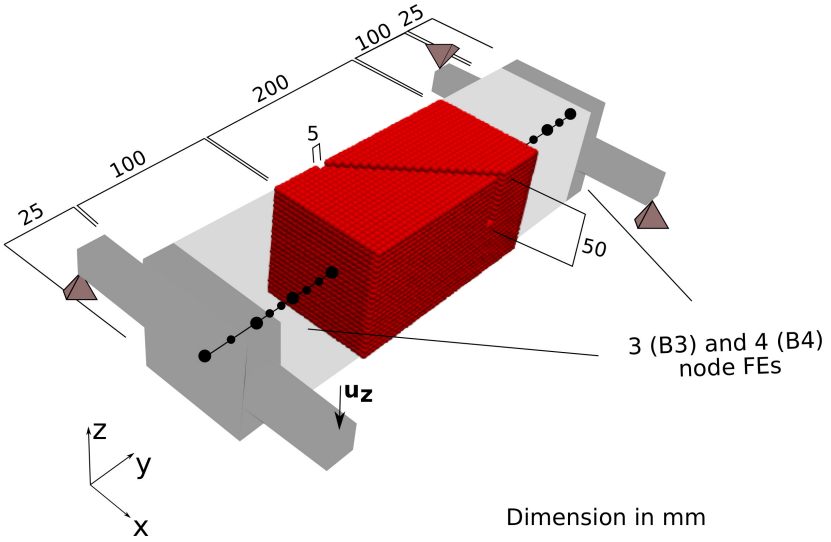

Fig. 7.34 Geometry and boundary conditions of the notched beam.

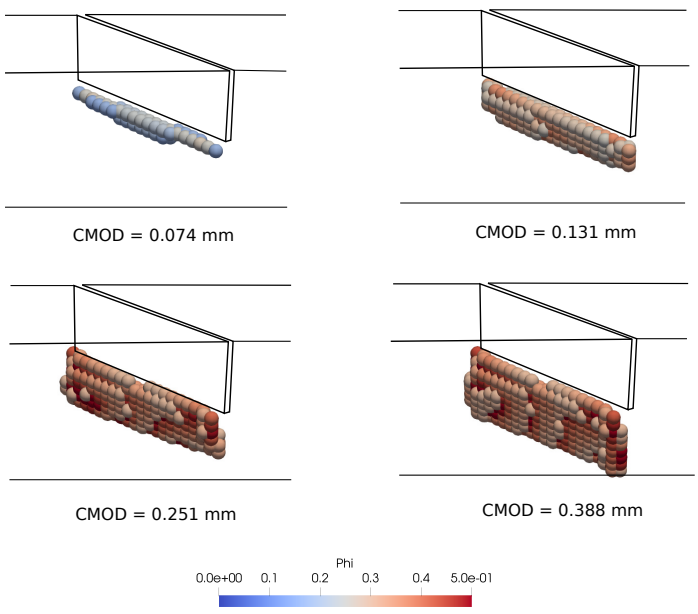

Fig. 7.35 The progression of the damage index φ, which provides insight into the propagation of cracks. For clarity, only the particles that have incurred damage are depicted.

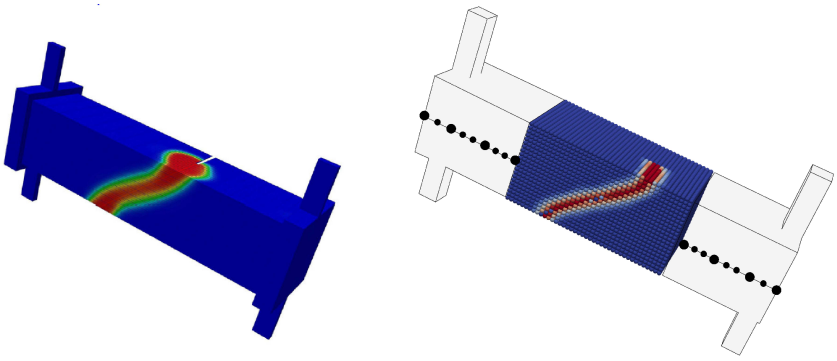

Fig. 7.36 Damage index distribution from a plasticity-damage model (left, adapted from [162]) and the present model (right).

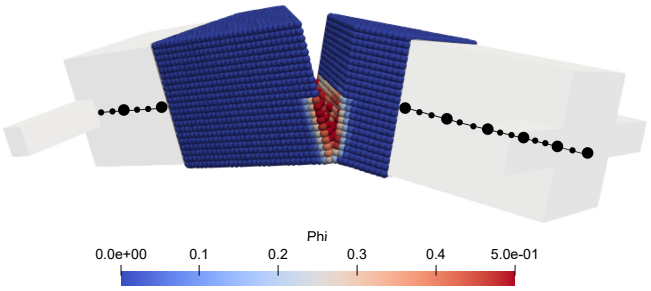

Fig. 7.37 Distribution of the damage index ϕ at the final step in the deformed configuration.

is accurately replicated. For a better understanding of the crack propagation in the Brokenshire test, Fig. 7.37 shows the deformed structure at the end of the simulation. In Fig. 7.38, the CMOD-force curves for various values of δ are depicted, with a fixed grid spacing Δx of 5 mm. The CMOD is computed between two points at the centre of the crack. The remaining curves represent the experimental results [159] and a numerical reference [163], respectively. The latter proposed a FEM-PD coupled model, where FEM nodes can be converted into PD nodes in order to track the crack. Thus, for this particular case, the number of PD DOFs in Table 7.19 indicates the total number of DOFs. A significant impact of the horizon radius on the peak load in this structure is evident. Similar to the previous case, an increase in the horizon radius δ results in a reduction of the failure load, while the corresponding CMOD remains unchanged. The simulation with $\delta = 5\Delta x$ yields a failure load comparable to that obtained in the numerical reference, which employed a higher number of DOFs and a more complex model. However, a noticeable difference from the experimental failure load remains.

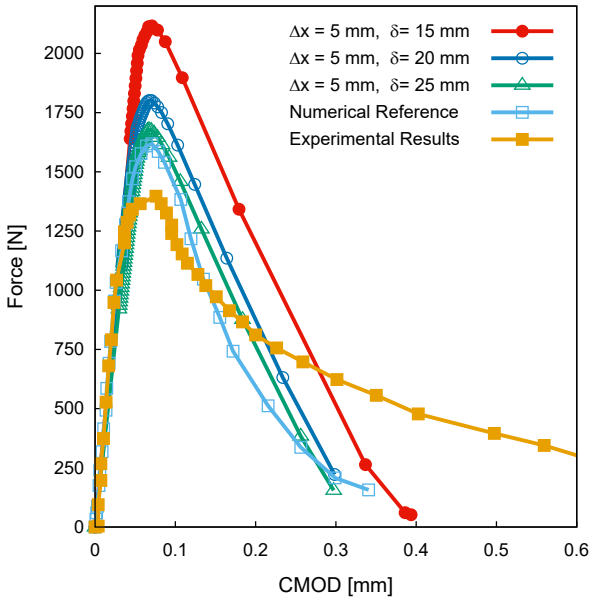

Fig. 7.38 CMOD-force curves considering various horizon radius δ for the notched beam under torsion.

Case	$\Delta x\,[mm]$	Horizon $\delta\,[mm]$	FEM DOFs	PD DOFs	Peak load [N]	CMOD [mm]
Experimental Results	-	-	-	-	1397	0.0075
Numerical Reference	2.5	7.5	-	939366	1618	0.007
1D FEM - 3D PD	5	15	774	54243	2117	0.0069
1D FEM - 3D PD	5	20	774	54243	1801	0.0067
1D FEM - 3D PD	5	25	774	54243	1678	0.0069

Table 7.19 Overview of essential parameters for both reference and simulation curves.

7.3 Global/local analysis

Numerical results obtained with the global/local approach proposed in this thesis are shown. Its capability is demonstrated by analyzing two-layer and ten-layer composite plates. For each example, the influence of the global and local meshes is investigated by performing convergence analyses, and the results are compared to those coming from refined layer-wise models. Furthermore, an analysis of a free-edge case is conducted, with the out-of-plane components of the stress tensor being evaluated using different patch dimensions and discretization. Finally, an aeronautical wing under bending load is considered. These analyses provides insight into the performance of the PW approach under varying conditions and further demonstrates its potential for accurate and efficient global/local analysis of complex structures. The stresses retrieved from the local refined analysis are reported in the global or material reference system (see Fig. 2.1).

7.3.1 Two-layer plate subjected to transversal pressure

The first case study is a two-layer plate subjected to transversal pressure, with $[90°/0°]$ stacking sequence. The plies are of equal thickness and are made of an orthotropic material, whose properties are enlisted in Table 7.20. Geometrical features and boundary conditions are shown in Fig. 7.39. A transversal pressure is applied on the surface of the laminate, with a magnitude equal to 10 kPa. All four edges are in clamped conditions.

This numerical case serves as an assessment of the proposed PW formulation. The model for the first step of the global/local analysis consists of 81 CQUAD4 elements. Then, two different regions are chosen for the local study, a single global element for case A (see Fig. 7.40(a)) and a 3×3 patch in case B (see Fig. 7.40(b)). Both regions are locally refined with high order finite elements, adopting a 5×5 grid of cubic Q16 in the plane and two LD3 for each layer through the thickness. The in-plane discretization of the local domain is represented by a grid built using Chebyshev nodes to minimize errors that occur at edges when using polynomial interpolation [164]. A comparison with the EW global/local approach and a full layer-wise model is provided. The latter is built with a total of 196 cubic Q16 elements for the in-plane mesh, while four-node cubic LD3 are adopted through the thickness of the plate, two for each layers. Strain and stress distributions are

E_{11}	E_{22}	E_{33}	ν_{12}	ν_{13}	ν_{23}	G_{12}	G_{13}	G_{23}
143.17	9.64	9.64	0.252	0.252	0.49	6.09	6.09	3.12

Table 7.20 Material properties in MPa.

evaluated in point Q $(\frac{a}{4}, \frac{b}{4})$, which corresponds to the centroid for both the single element and the 3×3 patch.

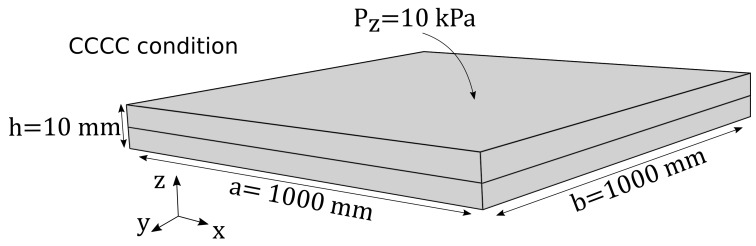

Fig. 7.39 Geometrical and modeling features of the investigated plate.

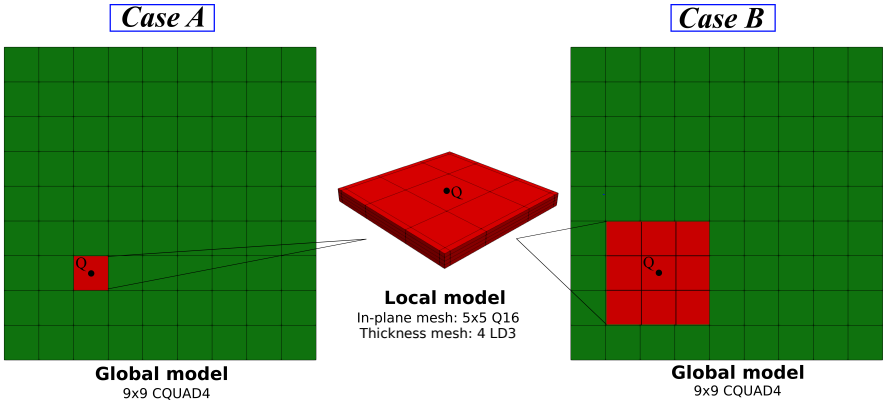

Fig. 7.40 Global and local models of the two-layer plate subjected to transverse pressure. Case A represents the EW approach, whereas a PW approach of a 3 x 3 elements region is recalled as Case B. Point Q represents the evaluation point of stress components.

Figure 7.41 shows the in-plane stress through the laminate thickness in point Q for the layer-wise model and the two cases of global/local analysis. Results obtained in cases A and B have a perfect match with those obtained through a refined model. Thus, in this specific case, it can be concluded that displacements and rotations extracted from the global model are sufficient as boundary conditions for the refined local analysis to retrieve the correct in-plane stress state of the laminate. Nevertheless, this consideration is not valid when out-of-plane stresses are evaluated (see Fig. 7.42). In fact, a slight discrepancy is witnessed for both σ_{xz} and σ_{yz} between case A and

the LW model. This error is mitigated when a larger global region is chosen to be locally analyzed, as in case B. As a result, a larger global area can help in providing a more accurate set of boundary conditions for the local model, thanks to the more significant number of global nodes involved. It is important to note that for each global/local approach considered (Case A or B), the transverse shear stresses fulfill the C_z^0 requirements [165], and they are null at the thickness edges. It should be underlined that the σ_{zz} component is not herein represented due to its very small value compared to other stress components.

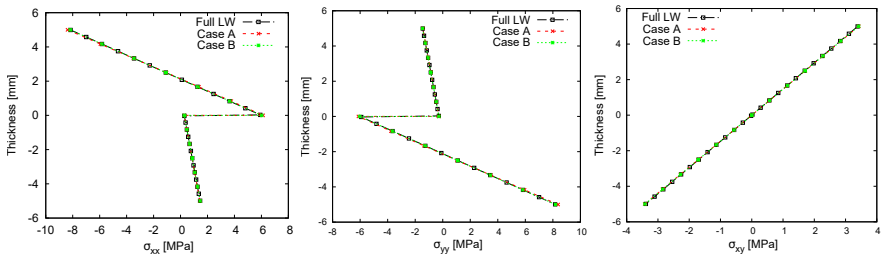

Fig. 7.41 Comparison of in-plane stresses distribution through the thickness of the laminate between a full LW model and two global/local approaches (see Case A and B in Fig. 7.40).

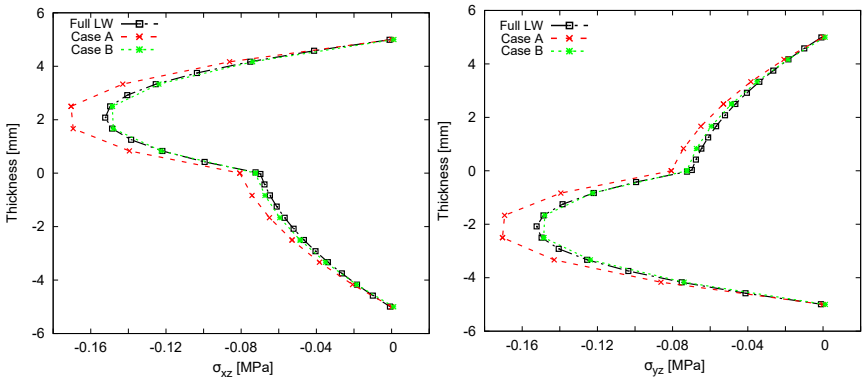

Fig. 7.42 Comparison of transverse shear stresses evolution through the thickness of the laminate between a full LW model and two global/local approaches (see Case A and B in Fig. 7.40).

Furthermore, a failure analysis is conducted. Failure Indices (FIs) are evaluated in point Q for each case using the Hashin 3D criterion [166]. The stress components obtained from the local analysis are used as input to evaluate the four Hashin-based FIs, namely fiber tension, fiber compression, matrix tension, and matrix compression. Results are shown in Fig. 7.43. Values obtained in cases A and B agree with the

X_T	X_C	Y_T	Y_C	XY	XZ	YZ
2586	1620	94.0	340.5	174.5	152.6	174.5

Table 7.21 Material allowables in MPa.

full LW model. It is noteworthy that no significant differences are observed between the two global/local analyses, despite the slight mismatch in the out-of-plane stress distribution (see Fig. 7.42). This is because the values of σ_{xz} and σ_{yz} are at least 100 times smaller than the in-plane stresses, resulting in a negligible influence of the out-of-plane stress values on the failure mechanism.

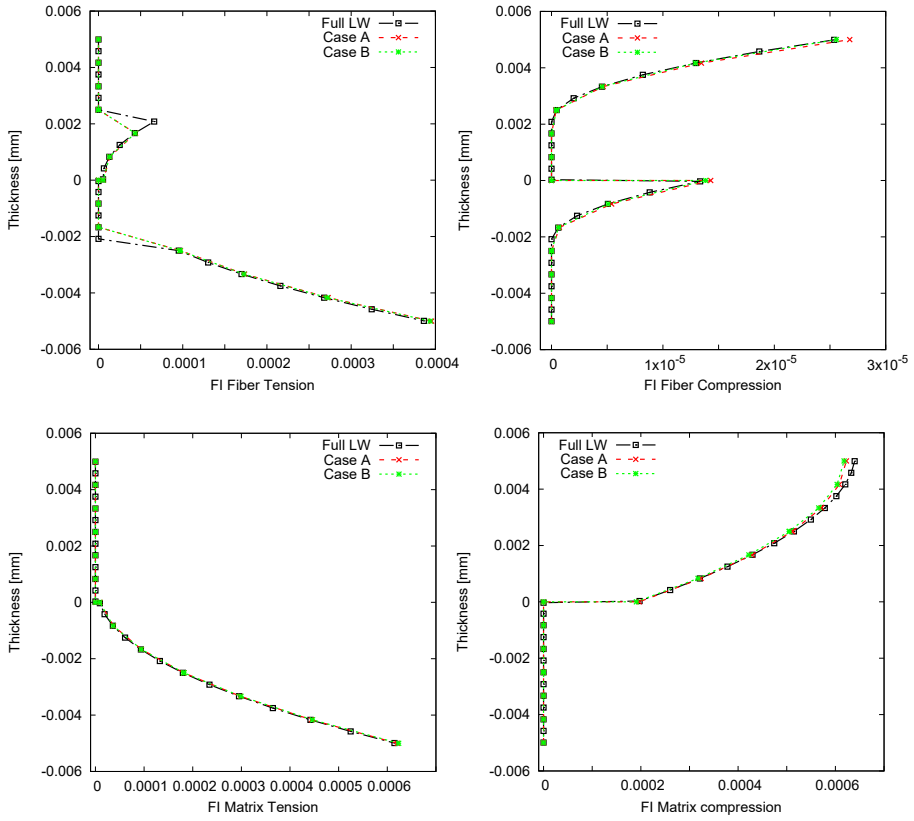

Fig. 7.43 Comparison of failure indices between a full LW model and two global/local approaches (see Case A and B in Fig. 7.40). Hashin 3D criterion has been applied for failure indices evaluation.

7.3.2 Ten-layer composite plate subjected to a localized transverse pressure

The second case study consists in a ten-layer composite plate. The material and geometric properties are the same as those used in the previous case. A symmetric stacking sequence $[90/45/45/0/90]_s$ is chosen. A transversal pressure is applied only on a central squared region, with a side dimension equal to 110 mm. The plate is simply supported.

Global mesh convergence

A preliminary convergence study is conducted on the mesh size of the global model. An illustrative overview of the three investigated cases is shown in Fig. 7.44. Briefly, we increase the refinement of the global model, mantaining the domain to be locally analyzed. Consequently, the local patch corresponds to a single global element for case A.1, a 2×2 patch for case B.1, and a 3×3 patch for case C.1 (see Fig. 7.44 for the details). The local model adopted is the same for all three cases, consisting of a 5×5 grid of Q16 elements for in-plane mesh and a total of ten LD3 through the thickness, one for each layer. Stresses are evaluated in point Q $(\frac{a}{4}, \frac{b}{4})$, and they are reported in the global reference system.

In-plane stress distributions are shown in Fig. 7.45. The convergence is reached with case B.1. It can be noticed that case A.1 already provides great overall accuracy. However, slight discrepancies can still be detected, such as σ_{xx} values in top and bottom layers or σ_{yy} behavior in $0°$- oriented layers. Through-the-thickness stress distributions are displayed in Fig. 7.46. Full layerwise solution for σ_{xz} is matched when cases B.1 and C.1 are considered. On the other hand, the σ_{yz} is well reproduced by each model.

Local mesh convergence

A second convergence study is performed on the mesh refinement of the local model. A 9×9 grid of four-node plate elements is adopted for the global model, and a 3×3 patch of global elements is chosen for the local analysis, whose centroid is located in point Q. Three different in-plane meshes are employed for the refined local models. Information about the considered cases is summarized in Fig. 7.47.

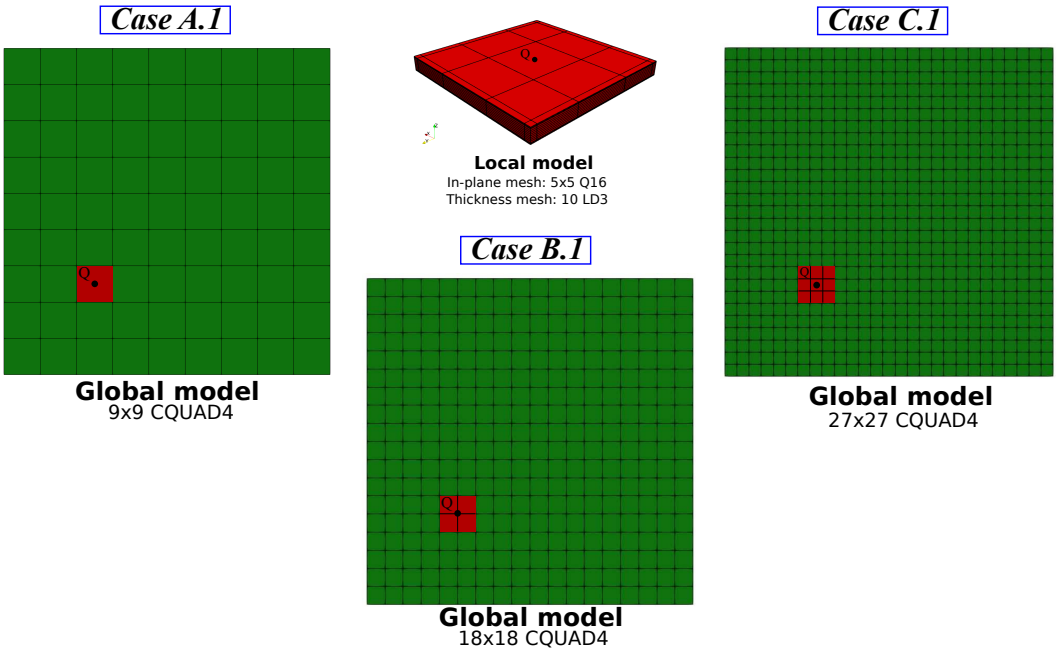

Fig. 7.44 Global and local models employed for global mesh convergence study. Patch of elements to be locally refined are highlighted in red. Point Q represents the evaluation point of stress components.

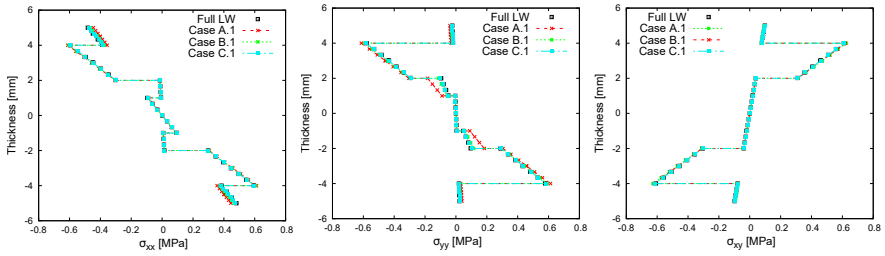

Fig. 7.45 Comparison of in-plane stresses evolution through the thickness of the laminate between a full LW model and three global/local models (see Case A.1, B.1 and C.1 in Fig. 7.44).

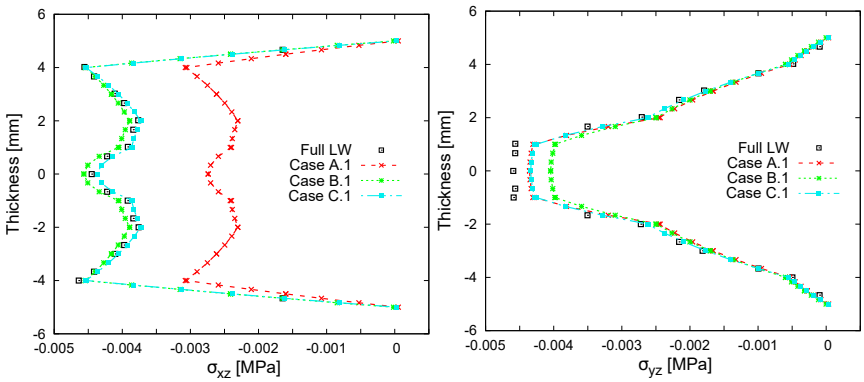

Fig. 7.46 Comparison of transverse shear stresses evolution through the thickness of the laminate between a full LW model and three global/local models (see Case A.1, B.1 and C.1 in Fig. 7.44).

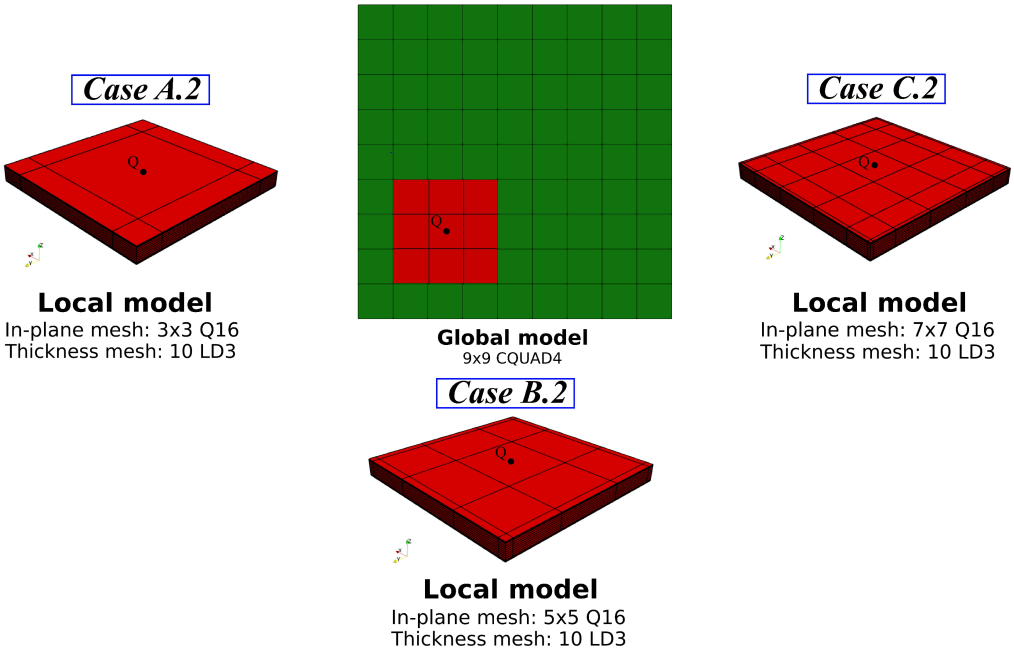

Fig. 7.47 Global and local models employed for local mesh convergence study. The patch of elements to be locally refined is highlighted in red. Point Q represents the evaluation point of stress components.

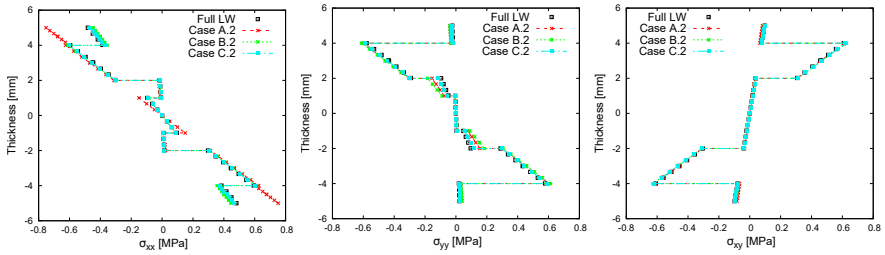

Fig. 7.48 Comparison of in-plane stresses distribution through the thickness of the laminate between a full LW model and three global/local models (see Case A.2, B.2 and C.2 in Fig. 7.47).

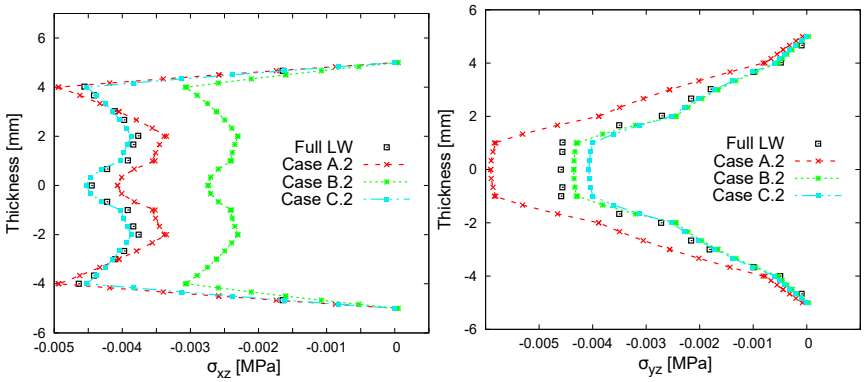

Fig. 7.49 Comparison of transverse shear stresses evolution through the thickness of the laminate between a full LW model and three global/local models (see Case A.2, B.2 and C.2 in Fig. 7.47).

Numerical results are shown in Fig. 7.48 for in-plane stresses and in Fig. 7.49 for the through-the-thickness components. A first important remark can be issued about the behavior of σ_{xx}. In fact, case A.2, representing the coarser local mesh, leads to significant differences in evaluating the normal stress at the top and bottom layers. On the other hand, cases B.2 and C.2 match the results obtained via the full LW model. As in the previous case study, transverse shear stress components are 100 times lower than in-plane ones. The global/local approach still correctly reproduce the behavior of transverse stress components retrieved with the LW model.

Centroid convergence

A final convergence study is performed considering the patch size as a parameter. In this case, mesh refinement for both the global and local models is fixed. A model with 324 CQUAD4 plate elements is adopted, while the local model is discretized

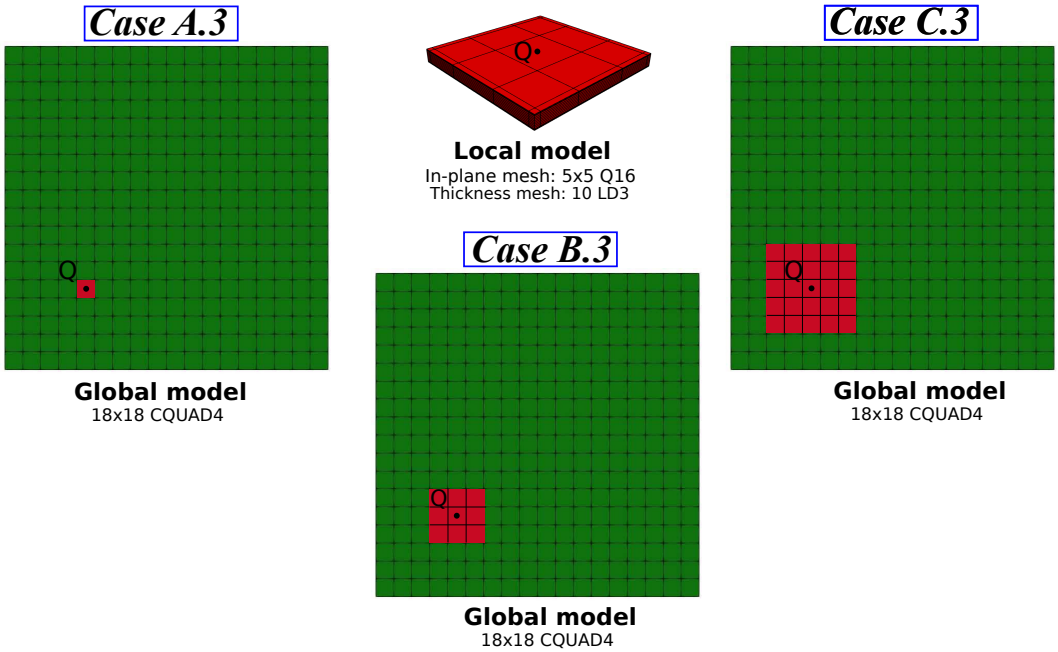

Fig. 7.50 Global and local model employed for patch size convergence study. Group of elements to be locally refined are highlighted in red.

with a 5×5 Q16 grid for the in-plane and ten LD3 through-the-thickness of the laminate. Thus, the only variable is the dimension of the patch to be locally analyzed. A single global element is considered in case A.3, whereas 3×3 and 5×5 patches of global elements are chosen for the local analysis in case B.3 and C.3, respectively. These regions have been chosen to have their centroids at the same coordinates. Figure 7.50 shows the three global/local models with red regions highlighting the different patches.

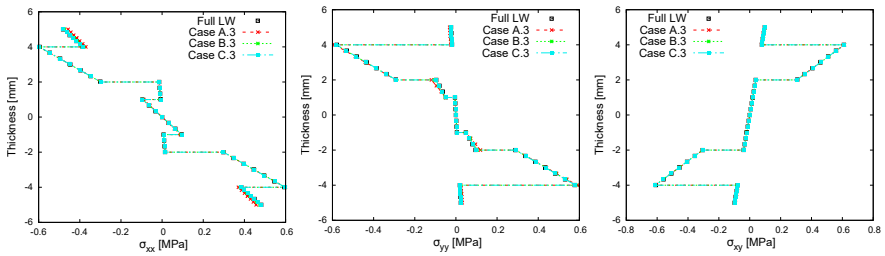

Fig. 7.51 Comparison of in-plane stresses evolution through the thickness of the laminate between a full LW model and three global/local models (see Case A.3, B.3 and C.3 in Fig. 7.50).

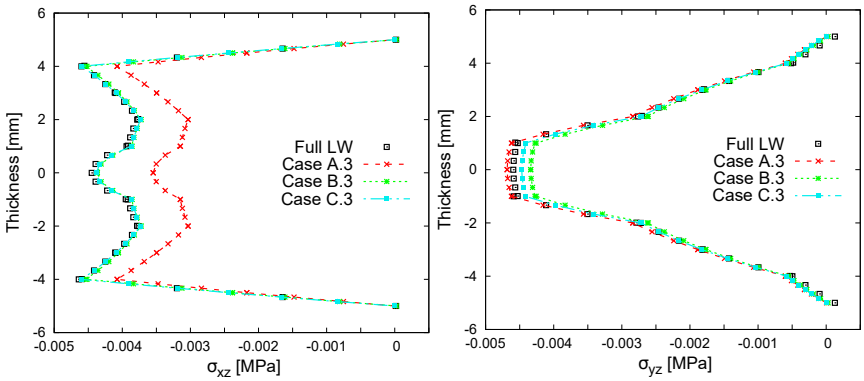

Fig. 7.52 Comparison of transverse shear stresses evolution through the thickness of the laminate between a full LW model and three global/local models (see Case A.3, B.3 and C.3 in Fig. 7.50).

Figures 7.51 and 7.52 depict the stress distributions for in-plane and out-of-plane components, respectively. It is evident that the single global element can provide sufficient information to obtain an accurate stress distribution for in-plane components and shear stress σ_{yz}. On the other hand, case B.3 global/local model is needed to correctly reproduce the σ_{xz} evolution through the thickness of the laminate.

7.3.3 Free-edge analysis

This case study shows the capability of this global/local approach to reproduce the free-edge effects which arise due to the mismatch of the mechanical properties of the plies at the interfaces. A composite plate from Lorriot et al. [167] is used as reference. The shape of the plate is a rectangle with sides equal to $a = 200$ mm and $b = 300$ mm (see Fig. 7.53). The mechanical properties of the orthotropic material are enlisted in Table 7.22. The stacking sequence of the plate is $[15_2/90/-15_2]_s$, and each ply has a thickness of 0.125 mm. The loading conditions adopted in the reference work are simulated by imposing a clamped condition at coordinate $y = 0$ and applying a traction force of 250 N on the opposite edge. The global mesh discretization consists of a total of 10 CQUADs along the x-direction and 15 elements along the y-direction. For this case, a single global element is chosen, meaning that an EW strategy is adopted.

Figure 7.53 displays the distribution of the transverse shear stress σ_{yz}, starting from the free-edge (at $x/h = 0$) towards the inner part of the plate. The black line

E_{11}	E_{22}	E_{33}	ν_{12}	ν_{13}	ν_{23}	G_{12}	G_{13}	G_{23}
159.0	8.4	8.4	0.33	0.33	0.33	4.1	4.1	4.1

Table 7.22 Material properties in GPa.

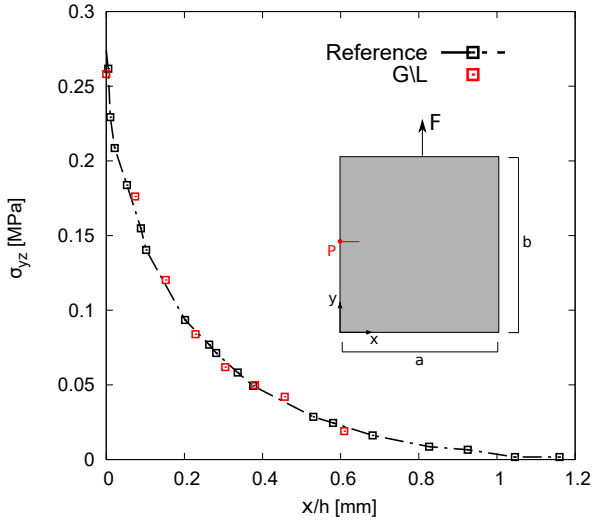

Fig. 7.53 Transverse shear stress along x at the plies interface 90/-15 for $y = b/2$. The horizontal axis starts at the free-edge (Point P) for $x/h = 0$ and goes towards the middle of the plate (along the red line). Reference solution is from [167].

represents the reference solution, whereas the red dots are the stress values estimated through the global/local approach in an EW manner. It is here important to remark that the shear stress value goes to zero for a ratio x/h equal to 1, revealing that the free-edge effects are confined in a very small region, with dimensions comparable to the plate thickness. For this reason, the EW approach is sufficient for accurately predicting the σ_{yz} at the free-edge and its evolution along the x-direction.

Nevertheless, the free-edge singularities can affect transverse stress values along a larger span length. In this situation, the importance of using a PW approach arises. As a further case, the composite beam investigated in [168] is considered. Geometry and loading conditions of the beam are shown in Fig. 7.54. The laminate has a stacking sequence $[45, -45]_s$, with each layer of equal thickness. A longitudinal strain $\varepsilon_{yy} = 0.01$ is applied to the structure.

Figure 7.55 shows the transverse shear stress at $y = l/2$ and at $z = h/4$, from the free-edge ($x/b = 0.5$) towards the centre of the plate, along the blue line. Solutions from four different test cases are compared with the approximated elasticity solutions of Pipes and Pagano [169]. Cases A and B use EW approaches with a fine and coarse

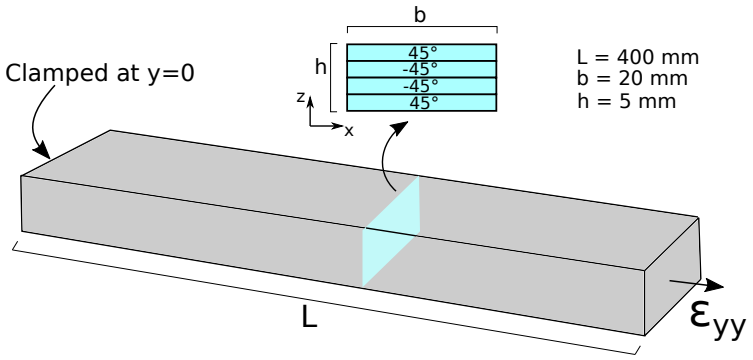

Fig. 7.54 Geometry and loading conditions of the laminated beam.

global mesh. For models C and D, a PW formulation with a 3×3 and a 5×5 patch is adopted in combination with the most refined global mesh. For all four cases, a 5×5 Q16 mesh is employed for the in-plane discretization of the local model, whereas 4 LD3 are adopted for the through-the-thickness mesh, one for each layer.

For the sake of completeness, the transverse shear stress evolution through the thickness of the plate is displayed in Fig. 7.56. The results obtained with the present G/L approach, with both EW and PW formulations, are compared with a reference solution [170], where a refined LW theory of structure based on Legendre polynomials is adopted.

The results suggest the following considerations:

- A PW formulation is needed to accurately describe the stress value at the free-edge and the evolution along the span length. In fact, EW models (cases A and B) show some discrepancies in reproducing the reference value for the transverse shear stress, which are correctly replicated when PW models are employed (cases C and D).

- In this particular case, the free-edge phenomenon affects the transverse stress in a relatively vast region. Thus, an EW approach is not suitable. In fact, model A is able to calculate σ_{yz} up to $x/b = 0.41$, where a value of zero stress is retrieved. A possible solution could consist of a coarser global mesh discretization, as in case B. However, even if the stress can be evaluated until $x/b = 0.25$, a discrepancy with the reference solution is still evident. Thus, using a PW model helps in both accuracy and solution field interval. Note that

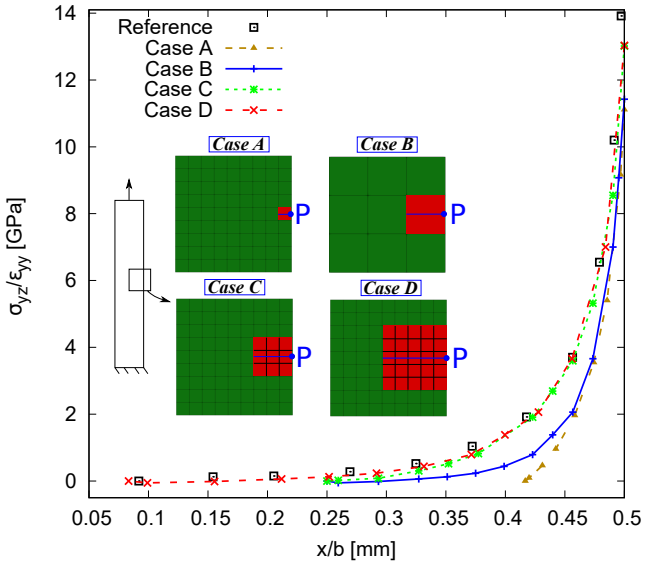

Fig. 7.55 Transverse shear stress along x at $z = h/4$ and $y = b/2$ for four different models, with the x-axis starting from point P at free-edge and moving towards the centre of the plate (blue line). Cases A and B uses EW formulation, whereas cases C and D adopt a PW formulation, with a 3×3 and 5×5 patch, respectively. Reference solution is taken from [169].

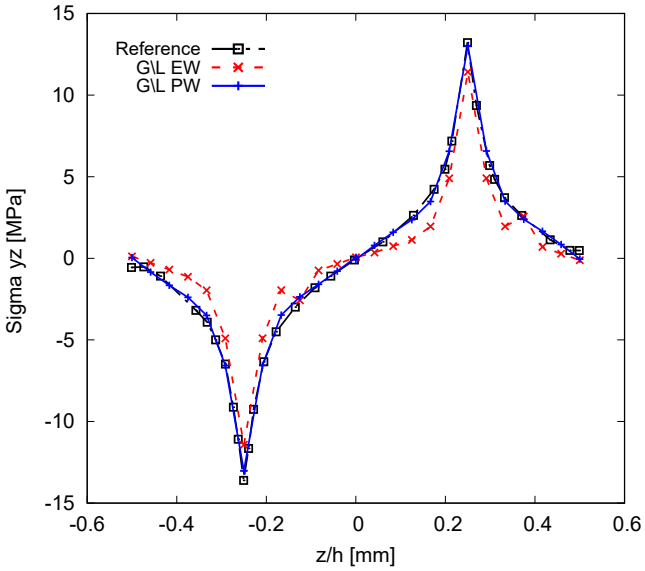

Fig. 7.56 Transverse shear stresses along z at $y = L/2$ and $x = b$. Reference solution [170] is obtained through a refined LW theory.

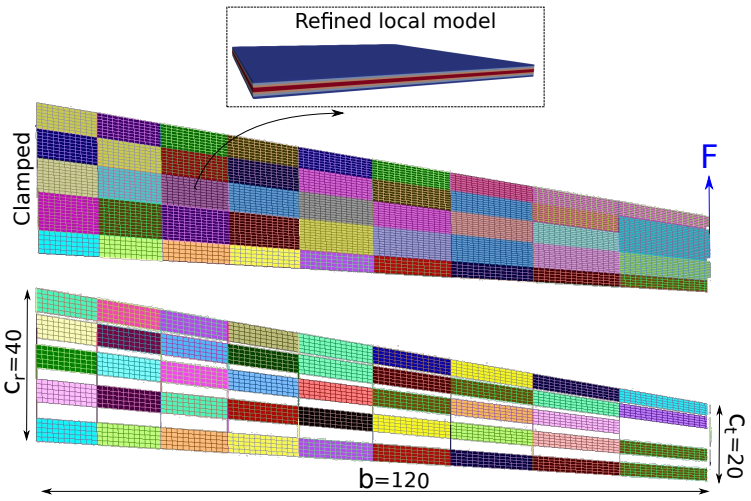

Fig. 7.57 Geometry and dimensions (in inches) of the wing. The panel chosen as local region is indicated and its local 3D representation is also shown.

E_{11}	E_{22}	E_{33}	ν_{12}	ν_{13}	ν_{23}	G_{12}	G_{13}	G_{23}
21.5	1.23	1.23	0.329	0.329	0.329	0.571	0.571	0.571

Table 7.23 Material properties in Msi.

the local region dimensions for cases B and C are the same, with a clear gain in accuracy provided by adopting a 3×3 patch.

7.3.4 Aeronautical composite wing under bending load

The last numerical example highlights the capability of the proposed approach to deal with complex structures. An aeronautical wing is considered. A graphical representation is shown in Fig. 7.57. Figure 7.57(a) depicts the wing and its upper skin, whereas Fig. 7.57(b) shows the inner core of the wing, more specifically spars and ribs. It should be noticed that each colour could represent a region with different properties, such as thickness and stacking sequence. The lower and upper skin structures are made of an orthotropic material, whose properties are provided in Table 7.23. The wing is clamped at one edge, whereas a vertical force of magnitude 15 lbf is applied at the opposite edge.

The global Nastran model is made of 14935 CQUAD4 elements. The selected region for the local analysis is illustrated in Fig. 7.57, and refers to a panel in the upper skin. A total of 121 global elements are then considered as local region. The

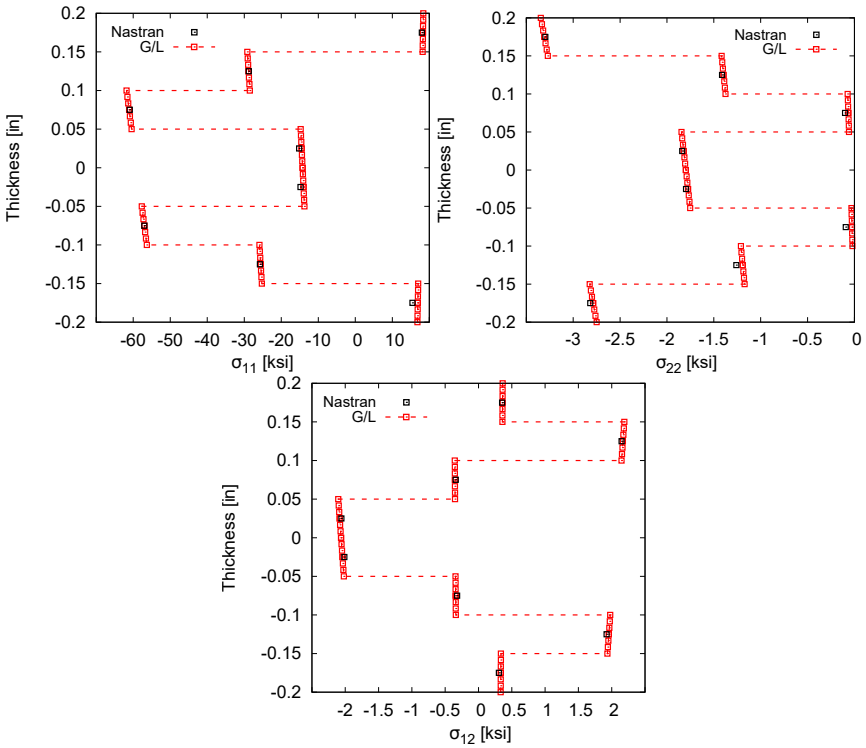

Fig. 7.58 Comparison of in-plane stresses evolution through the thickness of the wing panel between Nastran global simulation and G/L. The stresses are considered in the material reference system.

stacking sequence is $[90/45/0/-45]_s$ with respect to the leading edge. Finally, each ply has a thickness of 0.05 in. The refined region is discretized with a 5×5 grid of cubic Q16 elements, whereas a total of 16 LD3 element are adopted through the thickness, two for each layer.

The solution from the global/local analysis is compared with the results coming from the stress computation in Nastran at global scale. The evaluation is made in the central point of the investigated panel. Figure 7.58 shows the in-plane stresses distribution through the thickness of the wing panel, demonstrating an accurate match with the solution retrieved from the global analysis. For the sake of completeness, Fig. 7.59 illustrates the transverse stresses obtained with the proposed approach, expressed with respect to the global reference system.

Furthermore, a failure index evaluation is performed on the investigated panel. As previously done in Section 7.3.1, an Hashin-based criterion is adopted. The material allowables are presented in Table 7.24. The Hashin criterion is able to distinguish between four failure modes. Their distributions through the thickness

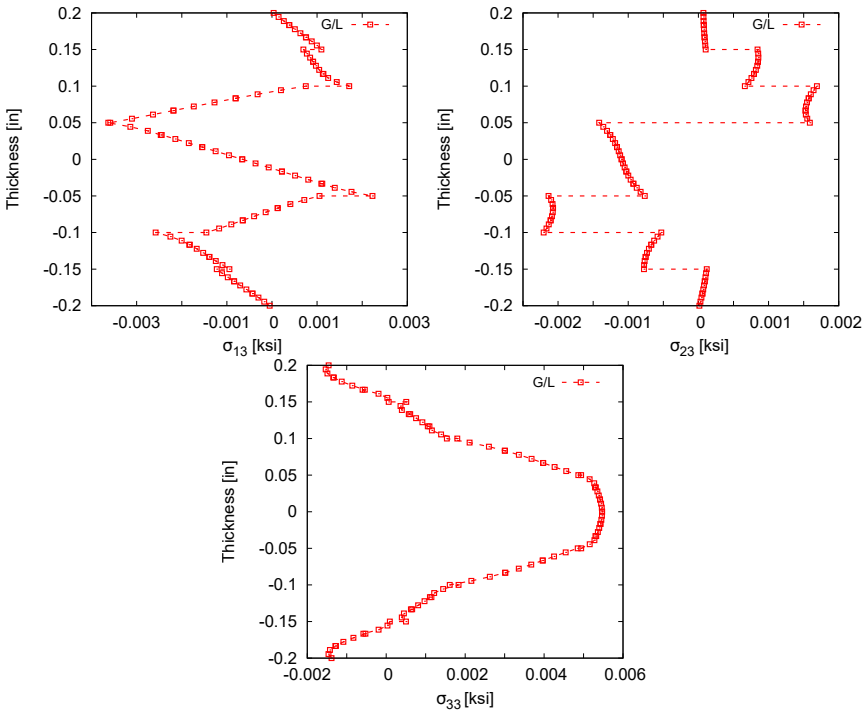

Fig. 7.59 Transverse stresses evolution through the thickness of the wing panel for the G/L model. The stresses are here considered in the local reference system.

X_T	X_C	Y_T	Y_C	XY	XZ	YZ
477.0	216.1	11.0	40.3	20.0	19.1	20.0

Table 7.24 Material allowable in ksi.

of the panel in its central point are depicted in Fig. 7.60. The outcome shows that the maximum value of failure index is found for the fiber compression mode in the layers with fiber oriented in the same direction as the leading edge, thus respecting the physics of the problem.

7.3.5 Localized progressive failure analysis in a pre-cracked plate

This case study consists of a notched plate subjected to a uniaxial traction load. The structure is made of an isotropic material, with Young modulus $E = 32$ GPa and Poisson ratio $\nu = 0.25$. As shown in previous sections, the reference solution is retrieved through progressive failure analysis of a coupled CUF/3D PD model. The reference model comprises two 2D CUF-based finite element domains and a 3D peridynamic region. Cubic Q16 elements are employed for in-plane discretization,

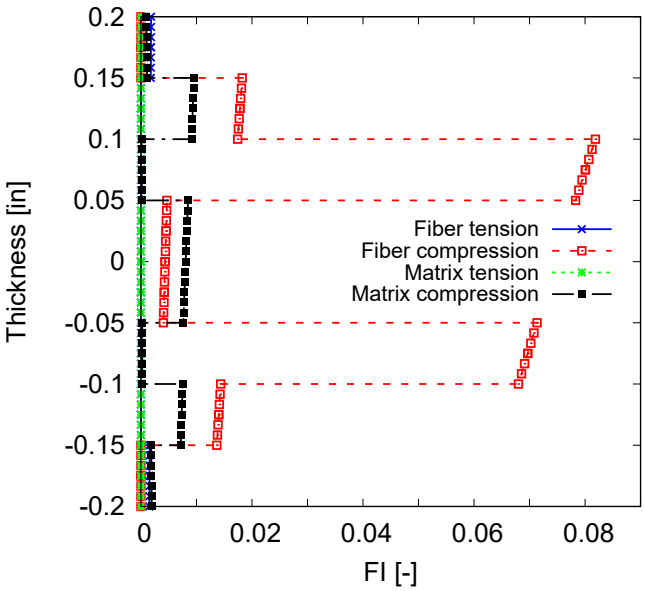

Fig. 7.60 Hashin-based failure indices in the investigated wing panel.

whereas linear interpolation is used for thickness expansion, see Fig. 7.61. A complete convergence investigation is carried out in order to tune the PD parameters to be adopted and to study the influence of mesh discretization at global and local scales.

Figure 7.62 displays the effect of the m-ratio value on the force-displacement curve. This value is expressed as $m = \frac{\delta}{\Delta x}$, with $\Delta x = 4\ mm$, resulting in three different values of horizon radius δ. A not negligible influence of the m-ratio on both peak load and related applied displacement is witnessed. These curves are compared with one obtained from a full FEM/PD model, where a m-ratio equal to 3 is chosen. Furthermore, Fig. 7.63 compares full and localized progressive failure analyses when the same PD parameters are employed. Notably, a reduction of the m-ratio (and, thus, a decrease in terms of horizon radius) leads to a closer match between the two different analyses. A summary of the outcomes displayed in Figs. 7.62 and 7.63 is provided in Table 7.25. A second convergence study is conducted on the dimension of the portion of the structure to be adopted as a local region while maintaining the global mesh discretization. Three different local regions are chosen. They are shown in Fig. 7.64. Figure 7.65 shows the load-displacement behavior when considering three different local regions. The curves are not affected by the different local domain dimensions, except for slight differences in the peak load. Results are also enlisted in Table 7.26. Finally, three different mesh discretizations

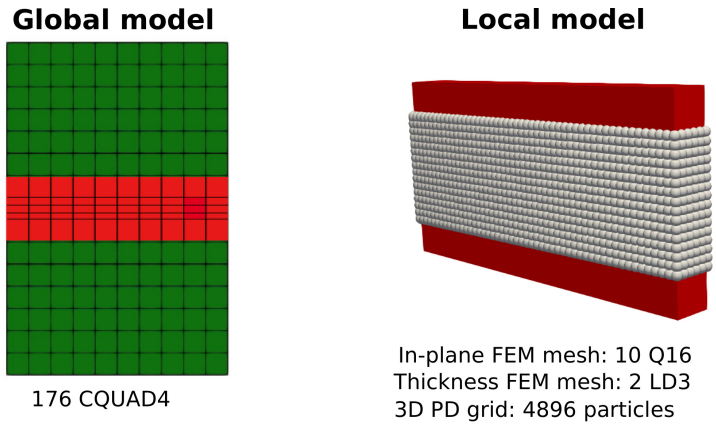

Fig. 7.61 Global and local models for the localized progressive failure analysis in a notched beam.

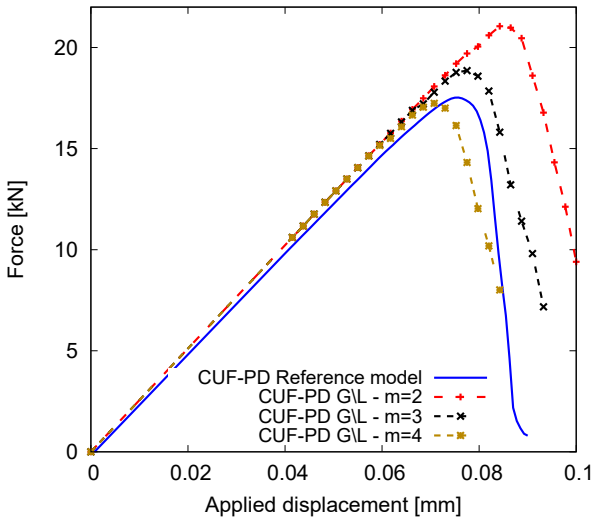

Fig. 7.62 Influence of PD parameter m-ratio over the force-displacement curve for localized progressive failure analysis. The outcomes are compared with those coming from a full FEM/PD model (solid blue line).

	m-ratio	Horizon δ [mm]	Peak load [kN]	u [mm]
Reference solutions				
CUF-PD Reference - Case 1	2	8	20.48	0.087
CUF-PD Reference - Case 2	3	12	17.52	0.076
CUF-PD Reference - Case 3	4	16	15.49	0.070
Present G/L approach				
CUF-PD G/L - Case 1	2	8	21.05	0.084
CUF-PD G/L - Case 2	3	12	18.59	0.079
CUF-PD G/L - Case 3	4	16	17.25	0.071

Table 7.25 Summary of key parameters for both reference and simulation cases with different grid spacing Δx and horizon radius δ.

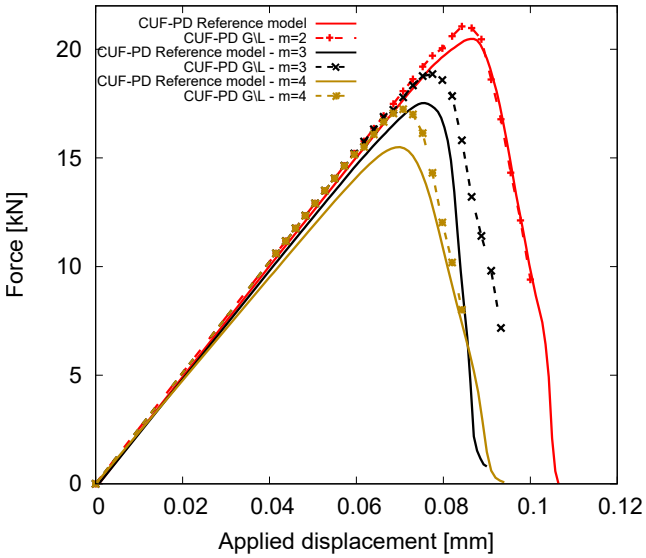

Fig. 7.63 Comparison of results of the localized progressive failure analyses with those from a full FEM/PD model with same m-ratio.

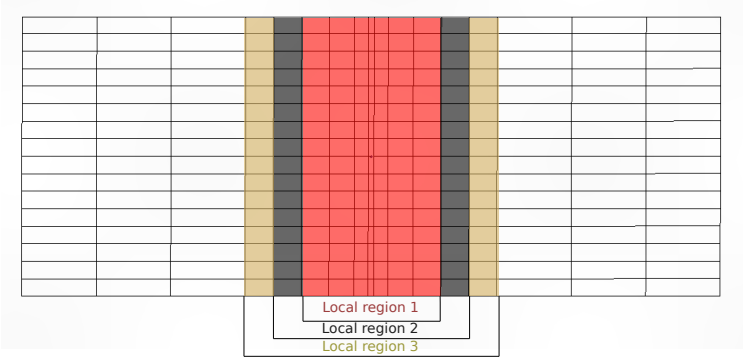

Fig. 7.64 Three different regions to be locally refined by using coupled FEM/PD models.

	Dimension [mm]	Peak load [kN]	u [mm]
CUF-PD Reference model	-	17.52	0.0076
CUF-PD G/L - Local region 1	100	18.55	0.0079
CUF-PD G/L - Local region 2	140	18.59	0.0079
CUF-PD G/L - Local region 3	180	18.82	0.077

Table 7.26 Summary of key parameters for both reference and simulation cases with different grid spacing Δx and horizon radius δ.

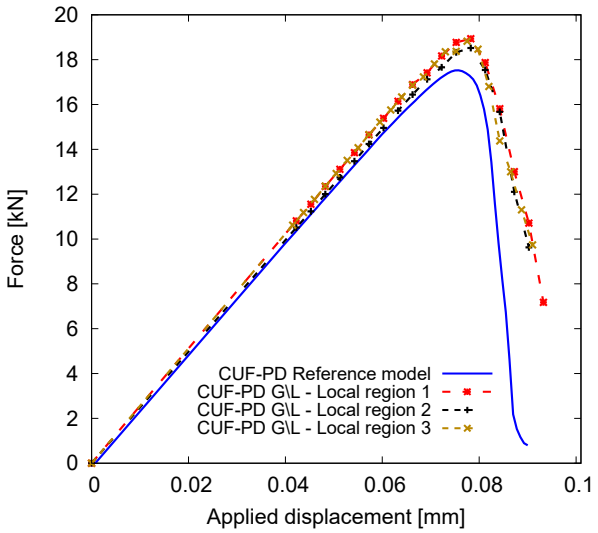

Fig. 7.65 Influence of local region dimensions over the force-displacement curve for localized progressive failure analysis. The outcomes are compared with those coming from a full FEM/PD model (solid blue line).

for the global domain are considered, while the dimensions of the local region to be refined are constant. Figure 7.66 demonstrates that this parameter does not really influence the local solution.

It should be underlined that the studies about how PD and FEM parameters, both at global and local scale, affect the problem solution are related to this specific simple case and thus not generalizable. Further investigations are needed to sustain these considerations in a more general way.

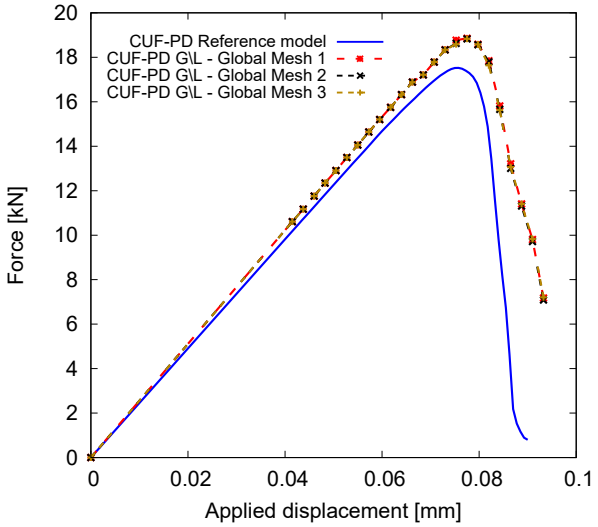

Fig. 7.66 Influence of global mesh discretization over the force-displacement curve for localized progressive failure analysis. The outcomes are compared with those coming from a full FEM/PD model (solid blue line).

Part II

Data-driven damage detection in multi-component structures

Chapter 8

Numerical techniques for damage detection

In this chapter, the numerical strategies and techniques employed in this work for damage detection purposes are presented. First, the component-wise formulation within the CUF framework is illustrated, and its advantages when dealing with damage modelling are explicated. Then, the necessity of using higher-order theories to build high-fidelity models to be adopted for damage mapping is made clear by presenting the results from two different cases.

8.1 Component-wise damage modelling

This section will highlight the advantages of a component-wise formulation for damage detection. CW models within the CUF framework are obtained using the Lagrange expansions element on cross-sectional subdomains of the multi-component structures in the case of beam formulations. In this research, CW formulation has been adopted to build a database for solving two different damage detection problems:

- Predicting the intensity and location of damage in randomly damaged metallic thin-walled structures by using an Artificial Neural Network (ANN) fed with dynamic parameters.

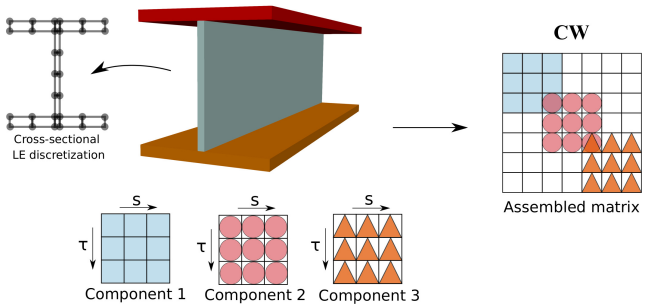

Fig. 8.1 Global matrix assembly using a CW formulation. Each colour denotes a distinct component.

- Prediction of damage severity and location by introducing into a CNN displacement and strain fields of randomly damaged composite laminates;

Figure 8.1 illustrates a CW modelling applied to an I-section beam, comprising three components: two flanges and the web. Each component can be represented by one or multiple LE elements. These LE elements are then assembled across the cross-section to derive the global stiffness matrix, as depicted in Fig. 8.1. One notable advantage of the CW formulation lies in its flexibility, enabling users to tailor the model's capabilities i) selecting a specific degree of accuracy for each component, and ii) determining the order of the structural model to be utilized. Consequently, this approach permits the introduction of varying levels of damage intensity for each component, facilitating a more localized distribution of damage within the structure, if required.

First, a basic isotropic damage modelling approach has been used. Thus, the Young moduli along all three directions are degraded by the same damage parameter d:

$$E_{ii}^{d} = (1-d) \times E_{ii}, \text{ with } 0 \leq d \leq 1 \tag{8.1}$$

where E_{ii}^{d} and E_{ii} represent the Young moduli for the damaged and pristine structure, respectively, whereas d denotes the damage index. This coefficient ranges from $d = 0$ to $d = 1$, representing the scenarios from an undamaged (pristine) component to a completely failed one. An example of damaged structures is illustrated in Fig. 8.2.

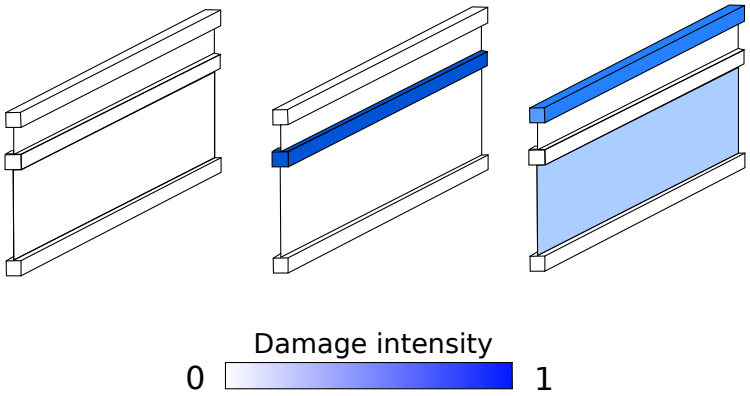

Fig. 8.2 Example of damage modelling in isotropic structures : Undamaged structure (left); one damaged component (centre); two damaged components with different intensities (right).

In the case of composite laminates, the aforementioned approach may oversimplify the situation since the properties can vary significantly between the longitudinal and transverse directions. To address this, orthotropic damage modeling has been incorporated. Within this framework, two parameters, namely d_1 and d_2, are utilized to account for stiffness degradation in each region. These parameters are employed to adjust the relative material matrix $\mathbf{C}$ according to the following modification, as described in [171].

$$\mathbf{C} = \frac{1}{\Delta}\begin{bmatrix} (1-R_2\nu_{23}\nu_{32})R_1E_{11} & (\nu_{21}+\nu_{23}\nu_{31})R_1R_2E_{11} & (\nu_{31}+R_2\nu_{21}\nu 32)R_1E_11 & 0 & 0 & 0 \\ & (1-R_1\nu_{31}\nu_{13})R_2E_{22} & (\nu_{32}+R_1\nu_{31}\nu 12)R_2E_{22} & 0 & 0 & 0 \\ & & (1-R_1R_2\nu_{21}\nu_{12})E_{33} & 0 & 0 & 0 \\ & & & \Delta R_1R_2G_{12} & 0 & 0 \\ & & & & \Delta G_{23} & 0 \\ & sym & & & & \Delta G_{13} \end{bmatrix} \tag{8.2}$$

where $R_i = (1-d_i)$, $i = 1,2$ are the reduction factors and $\Delta = 1 - R_2\nu_{23}\nu_{32} - R_1R_2\nu_{12}\nu_{21} - 2R_1R_2\nu_{31}\nu_{12}\nu_{23} - R_1\nu_{31}\nu_{13}$. Hence, the parameter d_1 is responsible for simulating damage along the longitudinal direction, while d_2 represents damage along the transverse direction, with both directions being defined within the material reference system. There are two potential approaches to incorporate damage into the analyzed structure. (see Fig. 8.3). The initial approach involves uniformly reducing

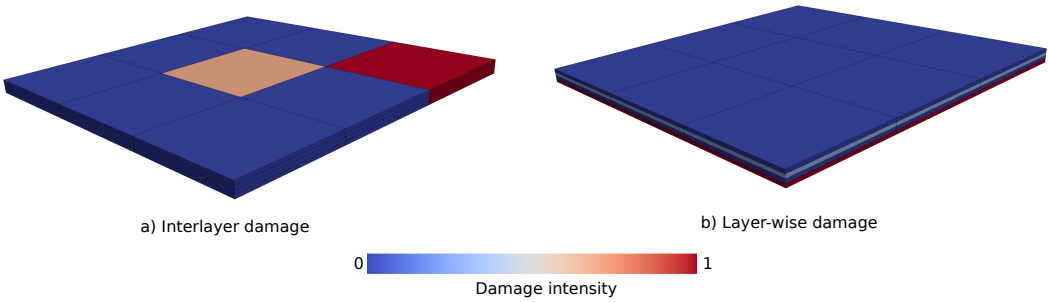

Fig. 8.3 Examples of component-wise damage modelling in composite laminates.

the stiffness across the entire thickness of a specific region within the composite section, which is further divided into four components. Alternatively, layer-wise damage modeling presents a second option, where each individual layer experiences a distinct level of intensity. It should be noted that these two methods can also be combined, allowing for a comprehensive analysis.

8.2 Need of higher-order theories for damage detection purposes

This segment explores the impact of damage localization and intensity on the structural response of a thin-walled isotropic beam and a composite laminate. Through the following examples, it will be demonstrated how crucial it is to employ accurate and component-specific models for effective damage detection.

8.2.1 Beam under bending and torsion

A cantilever I-section beam is considered the first numerical case study. The beam is made of an isotropic material, with Young Modulus $E = 200$ GPa and Poisson ratio $\nu = 0.2$. The geometrical features and boundary conditions are shown in Fig. 8.4. At first, a model assessment is carried out. The reference solution is obtained through commercial FE software using 3D brick elements. Different CUF-based TE and LE models are compared with the reference. In particular, the vertical displacement along the red line in Fig. 8.4 is considered. The outcome is displayed in Fig. 8.5. These findings underscore the importance of employing sufficiently enriched

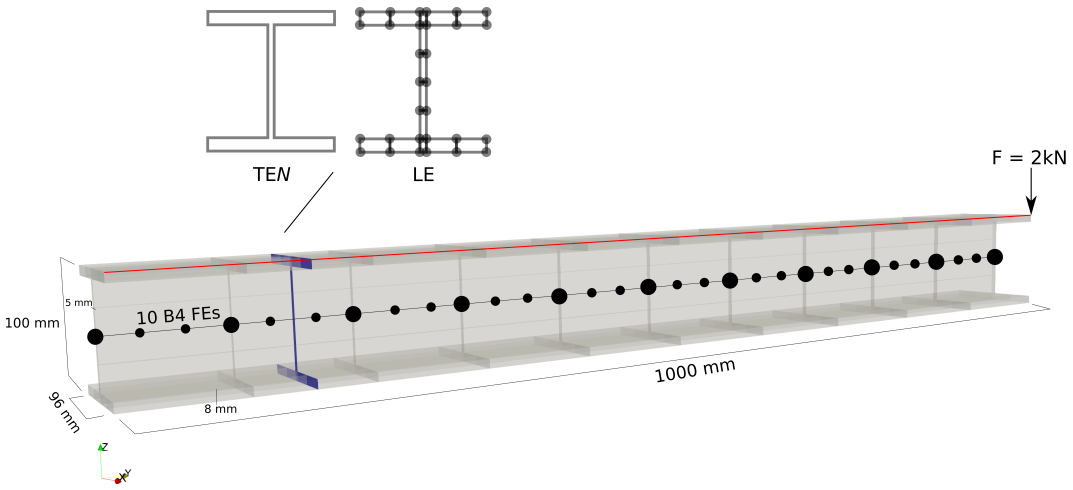

Fig. 8.4 Geometrical and modelling features of an I-section beam subjected to point load.

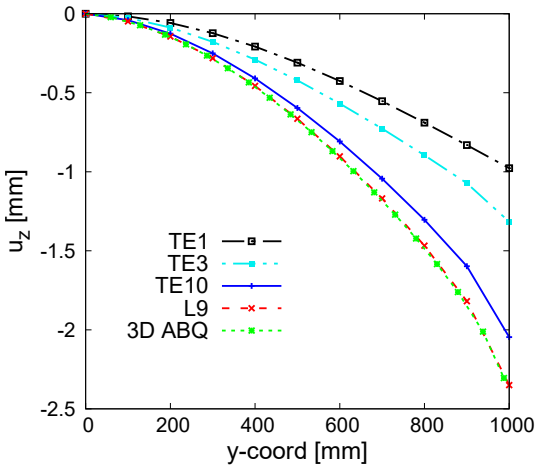

Fig. 8.5 Comparison of the vertical displacement along the red line in Fig. 8.4 using various theories. A numerical reference is provided by 3D Abaqus model.

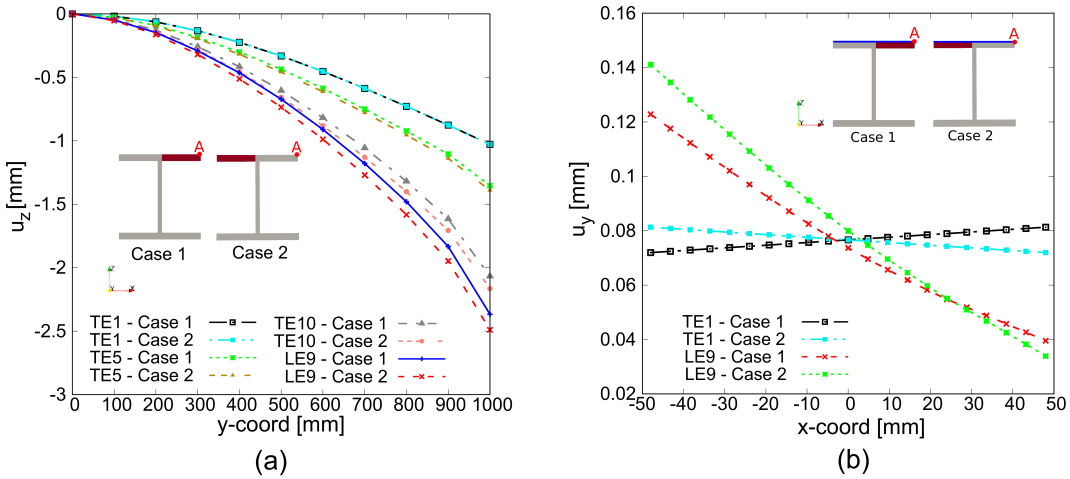

Fig. 8.6 a) Vertical displacement along the red line in Fig. 8.4 and b) longitudinal displacement along the blue line at $y = 1000$ mm are compared, using various theories and with two different damage scenarios. Point A denotes the loading point.

kinematics for CUF-based finite elements to achieve high accuracy. Notably, the curve generated by the low-order TE1 model exhibits significant deviation from the Abaqus 3D simulation. However, enhancing the kinematic theory results in a closer match, particularly evident when employing high-order LE9 models.

A subsequent numerical investigation focuses on an I-section beam to highlight the necessity of adopting a component-wise approach for damage detection. Two distinct regions of the cross-section have been subjected to damage, with identical extension and intensity. Specifically, the damage intensity (d) is set to 0.3, and these regions are situated on the right and left sides of the upper cap, denoted by red regions in Fig. 8.6. The damaged sections are confined to the vicinity of the clamped section, spanning $0 < y < 300$ mm, where a reduction in stiffness is expected a more pronounced influence on the beam's behavior.

Figure 8.6(a) displays the vertical component of the displacement along the red line for different FE models and both damage cases. A key observation arises from comparing the curves generated by employing low-order TE1 models. Notably, this theory fails to discern any discrepancy between the two damage scenarios in terms of vertical displacement. Such a limitation represents a significant drawback, particularly concerning damage detection. However, Fig. 8.6(a) also illustrates that enriching the beam kinematics enables better discrimination between the two damage cases. Similar observations hold for the longitudinal displacement, assessed along

E_{11} [MPa]	E_{22} [MPa]	E_{33} [MPa]	ν_{12}	ν_{13}	ν_{23}	G_{12} [MPa]	G_{13} [MPa]	G_{23} [MPa]
165.0	9.0	9.0	0.34	0.34	0.5	5.6	5.6	2.8

Table 8.1 Material properties.

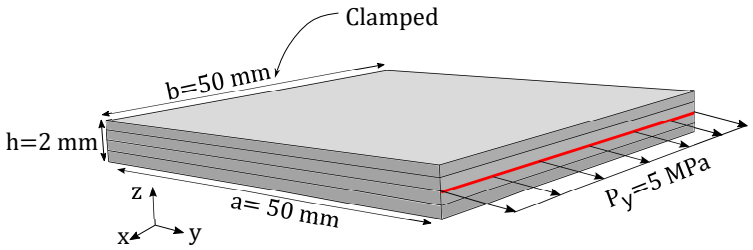

Fig. 8.7 Geometry and boundary conditions of the investigated composite laminate.

the blue line in Fig. 8.6(b) at the free section ($y = 1000$ mm). When utilizing TE1 models, an almost constant value of u_y is obtained due to the beam's rigid motion in the cross-section plane. Nonetheless, even with this low-order theory, a distinction between the two damage scenarios emerges in this case. Conversely, employing high-order LE theories facilitates an accurate depiction of the warping phenomenon experienced by the structure.

8.2.2 Composite laminate under uniaxial pressure

Another interesting case study involves a four-layer composite laminate, with stacking sequence $[90/0]_s$ (Fig. 7.39). The plies are of equal thickness and are made of an orthotropic material, whose properties are detailed in Table 8.1. TThe plate is clamped along one edge, wherease the opposite undergoes uniaxial traction. For the FE discretization along the longitudinal axis, three four-node cubic (B4) elements are utilized, while through-the-thickness discretization employs three LE9 elements for each layer. Various damage scenarios are explored, comprising nine distinct subportions of the entire domain. Each damaged area spans the entire stacking through the thickness, as depicted in Fig. 8.3a. The initial analysis examines the influence of damage location and intensity on the longitudinal displacement u_y along the middle surface of the laminate on one edge (red line in Fig. 8.7). Fig. 8.8 illustrates the introduction of isotropic interlaminar damage in a single region, with intensity ranging from 0 (indicating an undamaged structure) to 0.5 (resulting in a 50% reduction in region stiffness). The isotropic damage modelling will be adopted for all analyses in the present section. It is evident that damage location significantly

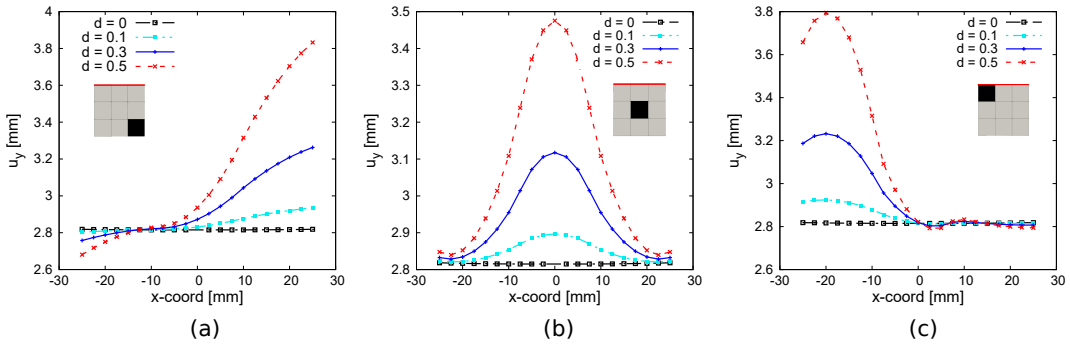

Fig. 8.8 Influence of a single damaged region on longitudinal displacement u_y.

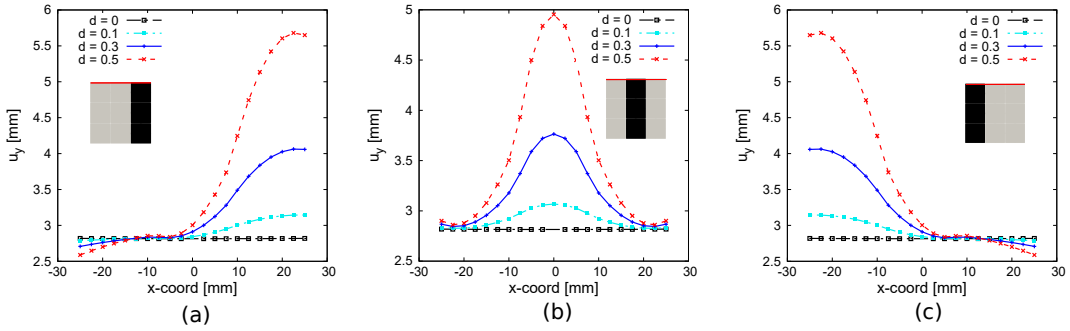

Fig. 8.9 Influence of three damaged regions on longitudinal displacement u_y.

affects the maximum displacement of u_y. Specifically, the maximum displacement occurs at the location of the damaged region, due to the stiffness reduction induced by the damage. In Figure 8.9, a cluster of three components experiences simultaneous damage. Similar to the previous scenario, the same type of damage is assigned on all four layers throughout the thickness. The affected regions exert a significant influence not only on the magnitude of the maximum displacement but also on its precise location. To examine the impact of layer-wise damage, Figure 8.10 illustrates the longitudinal displacement characteristics when an individual layer is subjected to damage. The study also explores the influence of the stacking sequence on the u_y displacement. Four distinct lamination configurations have been analyzed:

- Lamination 1 : [45/0/0/45] - Symmetric
- Lamination 2 : [45/0/45/0] - Asymmetric
- Lamination 3 : [90/0/0/90] - Symmetric
- Lamination 4 : [90/0/90/0] - Asymmetric

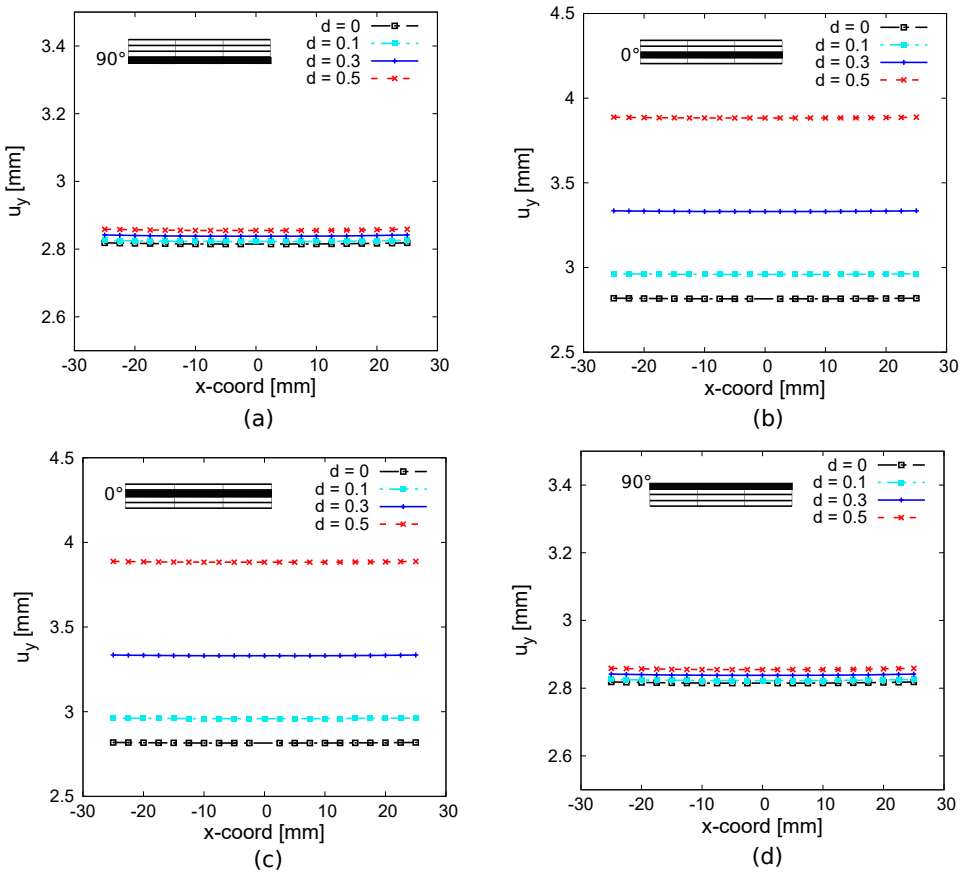

Fig. 8.10 Influence of layer-wise damage modelling on longitudinal displacement u_y, assessed along the red line.

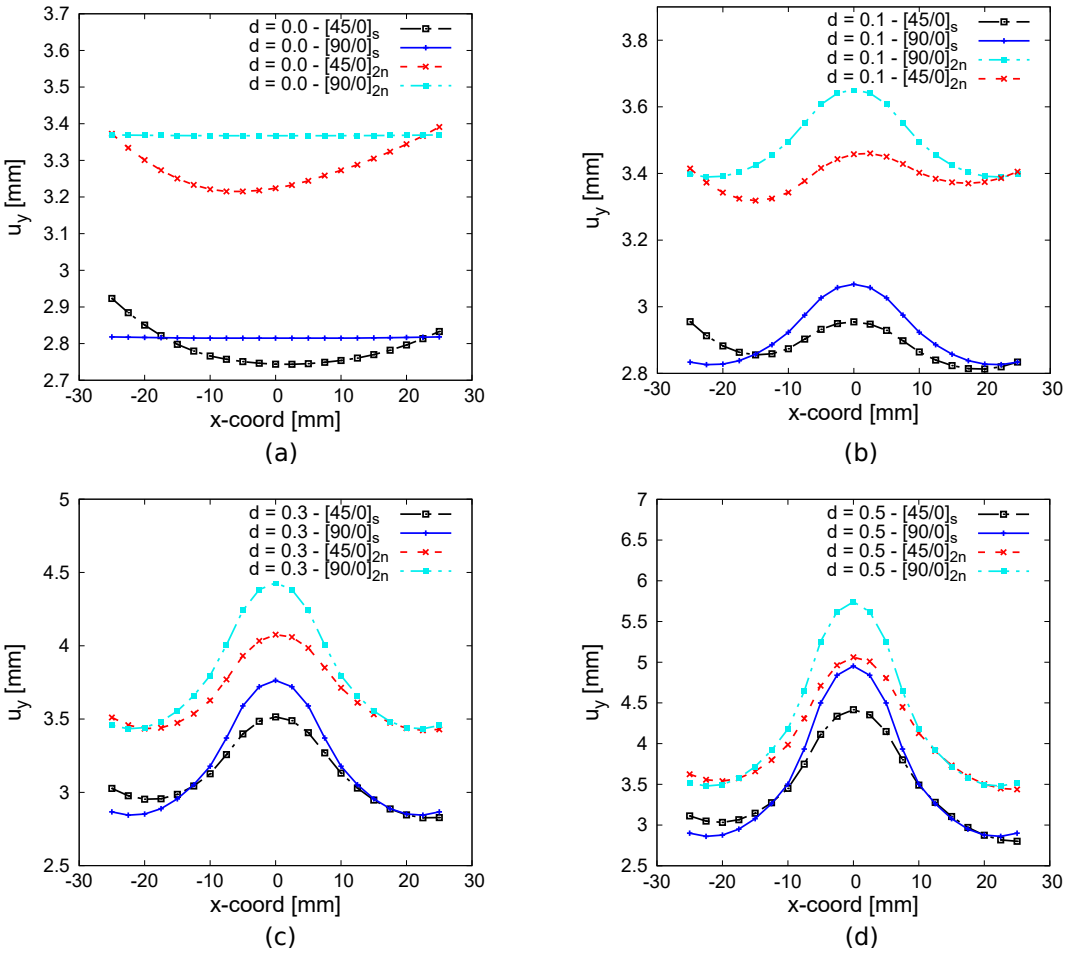

Fig. 8.11 Influence of the stacking sequence on longitudinal displacement u_y at fixed level of damage.

The results for four different damage scenarios have been displayed in Fig. 8.11.

Remarks about direct problem and damage simulation

The investigations conducted in Sections 8.2.1 and 8.2.2 yield significant insights. In section 8.2.1, the importance of employing high-order theories and component-wise approaches for accurate damage detection is demonstrated. Low-order theories inadequately capture complex mechanical behaviors such as bending and torsion, resulting in an inaccurate portrayal of the effects arising from localized damages. In section 8.2.2, the impact of damage in a composite laminate is explored. Initially, Figures 8.8, 8.9, and 8.10 provide insights into how damage location and intensity affect displacement. Notably, the magnitude and location of maximum displacement

can vary significantly when damaging different regions. An illustrative example is seen in cases (a) and (c) in Fig. 8.8. In the former, the maximum displacement u_y occurs at the plate's edge ($x = l/2$), while in the latter, with damage near the load application, the maximum displacement u_y is detected at $x > -l/2$. However, such differences are eliminated when damage spans the entire plate length, as depicted in Fig. 8.9, resulting in symmetric behavior in terms of displacement location and intensity for cases (a) and (c).

The results presented in Fig. 8.10 highlight that damage exerts a more pronounced influence on axial displacement when occurring in layer soriented at 0 degrees, compared to those oriented at 90 degrees. While this outcome is expected for the present case, different loading conditions such as bending and shear will yield a more intricate response of the structure to layer-wise damage, necessitating high-order theories for accurate description. Figure 8.11 depicts the variation in longitudinal displacement when various stacking sequences are adopted. As expected, different lay-ups lead to different structural responses due to the change in the laminate properties.

Chapter 9

AI-based damage detection methods

This chapter is devoted to introducing two different AI techniques for damage detection purposes. A vibration-based method is first introduced. An Artificial Neural Network (ANN) is employed to solve the inverse problem: given some specific features, the ANN should be able to predict both the location and intensity of damages in the investigated structure. For this method, some vibrational characteristics (e.g. natural frequencies and Modal Assurance Criterion (MAC) scalars) are considered. The influence of damage in aeronautical structures is first demonstrated in this chapter. Then, the procedure adopted to solve the inverse problem using ANN is illustrated. The second proposed technique uses displacement and strain field images to perform a complete mapping of damages in composite laminates. A Convolutional Neural Network (CNN) architecture is employed here. The common feature between the two methods is the creation of a training database using CUF-based models, allowing a component-wise modelling of the structures and thus the capability of introducing a different damage in each component of the structure.

9.1 Vibration-based damage detection

The first technique adopted for structural damage detection is the vibration-based method. This approach operates on the principle that structural damage induces alterations in dynamic parameters such as natural frequencies, mode shapes, and damping. The primary obstacle lies in establishing the correlation between these

dynamic parameters and the damage itself, enabling the development of an algorithm capable of accurately predicting both the location and severity of the damage.

In a recent investigation [172], it was demonstrated that establishing a straightforward correlation between changes in natural frequencies and the presence of damage is not always feasible. Specifically, certain types of damage can impact natural frequencies without affecting the corresponding mode shapes, or vice versa. To address this challenge, the authors introduced the Modal Assurance Criterion (MAC) as an additional evaluation metric alongside the analysis of natural frequencies. The MAC quantifies the correlation between modal shapes of damaged and undamaged structures by calculating the normalized scalar product of two modal vectors. Subsequently, these scalar values are organized into the MAC matrix:

$$MAC_{ij} = \frac{|\{\phi_{A_i}\}^T \{\phi_{B_j}\}|^2}{\{\phi_{A_i}\}^T \{\phi_{A_i}\} \{\phi_{B_j}\} \{\phi_{B_j}\}^T}$$

where $\{\phi_A\}$ and $\{\phi_B\}$ represent the damaged and undamaged modal vector for the i^{th} and j^{th} modes, respectively. The MAC indicator assumes values ranging from 0 (indicating no consistent correspondence) to 1 (representing a consistent correspondence) between the modal vectors. In [172], the goal pursued was to assess the influence of damage location and intensity on the vibration characteristics of the structure. Consequently, the study aimed to solve the direct problem in this regard.

9.1.1 Influence of damage on vibrational characteristics

In this section, two case studies to demonstrate the effect of damage on the structural dynamic parameters are proposed.

Three-stringer spar

The initial evaluation involves a longeron structure with three stiffeners, as depicted in Figure 9.1. The geometrical specifications of this structure are as follows: length (L) = 3 m, cross-sectional height (h) = 1 m, stringer area (A_s) = 1.6×10^{-3} m, panel thickness (t) = 2 mm, and distance between the top and middle stringers (b) = 0.3 m. The longeron is composed of a homogeneous and isotropic material with the

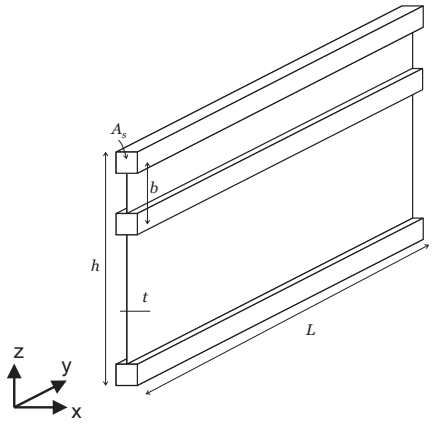

Fig. 9.1 Geometry of three-stringer spar.

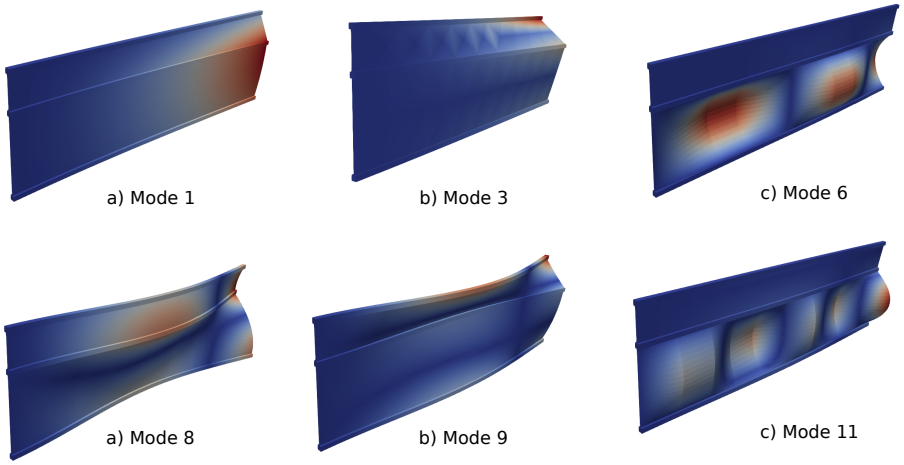

Fig. 9.2 Mode shapes of undamaged three-stringer spar.

following properties: Young's Modulus (E) = 75 GPa, Poisson's ratio (ν) = 0.33, and a density of 2700 kg/m^3. The spar is clamped at y = 0 mm.

This particular case study has previously undergone validation in a prior investigation [172]. The focus of the previous study was on calculating the natural frequencies of the structure using the CW beam model. Figure 9.2 showcases representative mode shapes of an intact three-stringer spar. Table 9.1 presents the frequencies for the undamaged structure as well as three different damage cases. The MAC matrices, depicted in Figure 9.3, illustrate the mode-to-mode comparisons between the undamaged structure and the aforementioned three damaged structures. These final two parameters play a crucial role in training the Artificial Neural Network (ANN).

	Undamaged	d=0.1	d=0.3	d=0.5
f_1	3.17	3.00	2.65	2.25
f_2	3.56	3.38	3.00	2.55
f_3	3.83	3.65	3.27	2.84
f_4	14.27	13.59	12.12	10.42
f_5	16.73	15.90	14.10	12.01
f_6	17.67	16.94	15.37	13.61
f_7	21.17	20.40	18.19	15.41
f_8	21.70	20.59	18.78	16.37
f_9	22.95	21.79	19.27	16.96
f_{10}	25.10	23.89	21.23	18.19
f_{11}	25.75	24.85	22.98	20.94
f_{12}	31.21	30.15	27.92	25.47
f_{13}	37.92	36.60	33.81	30.75
f_{14}	45.79	44.13	40.61	36.73
f_{15}	54.85	52.77	48.35	41.20

Table 9.1 First 15 natural frequencies (Hz) of the Three-stinger spar for the undamaged case and three damage scenarios.

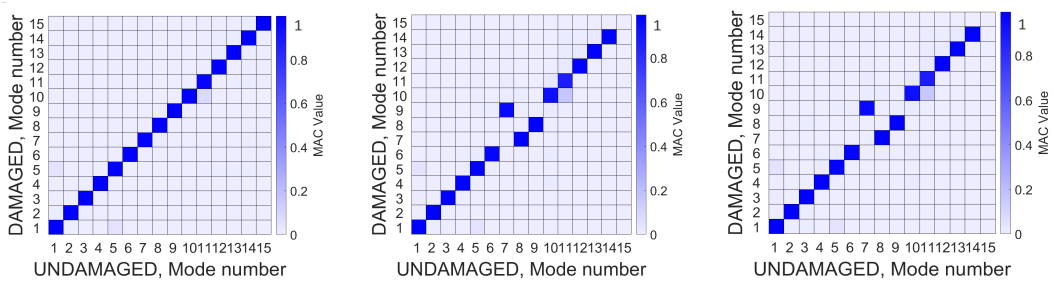

a) d = 0.1 **a) d = 0.3**

Fig. 9.3 MAC mode-to-mode comparison between undamaged and damaged three-stringer spar for different damage scenarios.

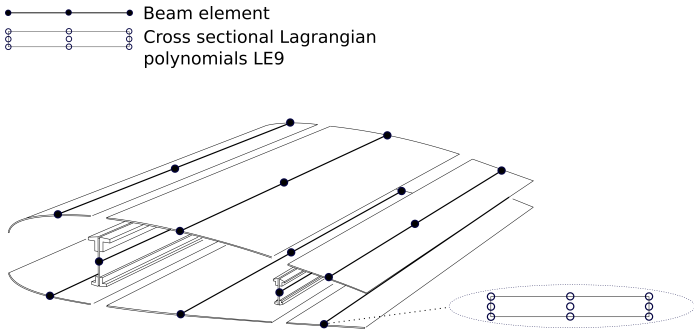

Fig. 9.4 CW model of a NACA profile wing.

Naca wing profile

As the second assessment, a complete wing is considered in this study. The wing features a straight configuration with a NACA 2415 airfoil, and its cross-sectional geometry is depicted in Figure **??**. The chord length (c) is set at 1 m. Each panel has a thickness of 3 mm, while the spar webs have a thickness of 5 mm. The dimensions of the spar caps can be found in the reference [173]. The overall length of the structure is $L = 6$ m. The wing consists of three wing boxes separated by transversal stiffening members located at sections $y = 2$ m, 4 m, and 6 m. The ribs have a thickness of 6 mm. For the purpose of illustration, the wing is assumed to be entirely made of a metallic material, specifically an aluminum alloy. The material properties of the aluminum alloy are as follows: elastic modulus $(E) = 75$ GPa, Poisson's ratio $(\nu) = 0.33$, and density $(\rho) = 2700$ kg/m^3. The wing is clamped at $y = 0$ mm. The validity of this model has been established in the reference [173].

As in the precedent case study, the CW model is considered. Each longeron, panel, leading, and trailing edge is discretized separately, as depicted in Figure 9.4. Nine B4 elements are utilized for discretization along the longitudinal axis, while a combination of L3, L4, and L9 elements is employed for the cross-section. Figure 9.5 showcases some typical mode shapes of an intact NACA profile wing. Table 9.2 presents the frequencies of 15 modes for both the intact structure and three distinct damage scenarios. Conversely, Figure 9.6 illustrates the MAC matrices for comparing mode shapes between the intact and the aforementioned three damaged structures.

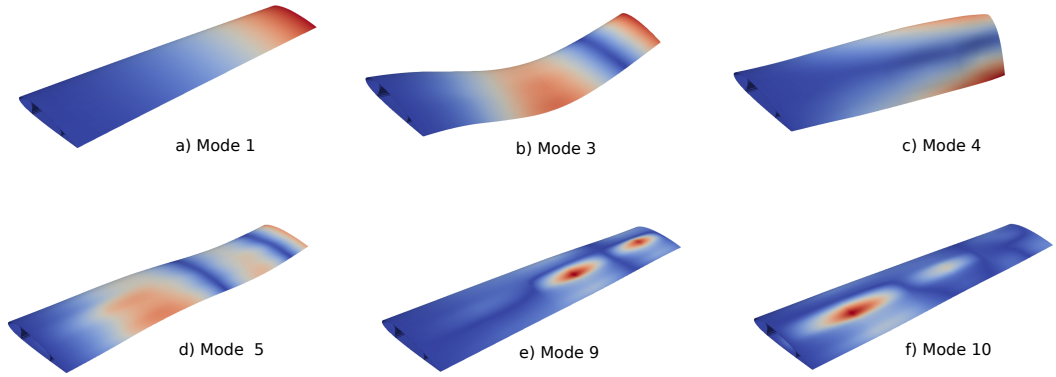

Fig. 9.5 Mode shapes of undamaged NACA profile wing.

	Undamaged	d=0.1	d=0.3	d=0.5
f_1	4.14	3.93	3.47	2.93
f_2	21.28	20.24	17.94	15.24
f_3	25.00	23.81	21.16	18.02
f_4	39.45	39.32	39.03	38.61
f_5	64.84	62.02	55.66	47.94
f_6	85.61	82.09	73.90	63.84
f_7	91.54	87.39	78.07	67.03
f_8	93.46	89.15	79.61	68.39
f_9	96.99	93.70	85.89	75.54
f_{10}	103.67	99.45	89.85	78.23
f_{11}	104.82	100.43	90.88	79.56
f_{12}	106.76	102.29	92.38	80.62
f_{13}	109.90	105.69	96.42	85.06
f_{14}	115.76	111.201	100.69	87.63
f_{15}	124.19	119.33	108.49	95.39

Table 9.2 First 15 natural frequencies (Hz) of the NACA profile wing for the undamaged case and three damage scenarios.

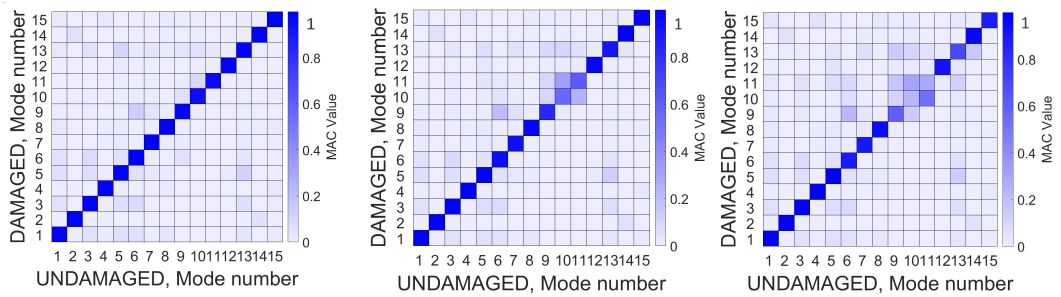

Fig. 9.6 MAC mode-to-mode comparison between undamaged and damaged NACA profile wings for different damage scenarios.

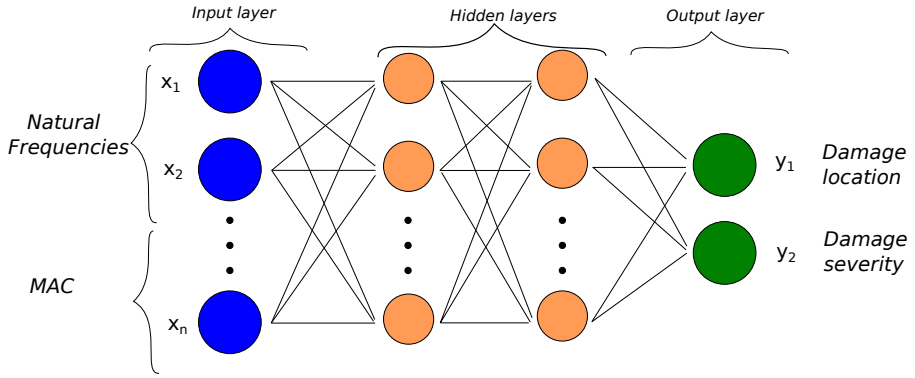

Fig. 9.7 Representation of the architecture of an Artificial Neural Network.

9.1.2 Simulation-driven ANN training process

Section 9.1.1 has elucidated the impact of damage on natural frequencies and mode shapes. In this study, the objective is to develop a model capable of detecting the location and intensity of all damages within separate components of the structure, given the free vibration characteristics (natural frequencies and MAC matrix scalars). This model consists of an Artificial Neural Network (ANN), trained through a database of damage scenarios generated using the CW approach. An artificial neural network is a group of interconnected neurons, typically organized into layers including an input layer, one or more hidden layers, and an output layer. Each layer may contain a varying number of neurons, and each neuron is connected to all neurons in the subsequent layer. An example of ANN architecture used in this work is depicted in Fig. 9.7. It is a feedforward neural network, employing hyperbolic tangent sigmoid transfer functions for the hidden layer(s) and linear functions for the output layer. An ANN can learn during the training process, which aims to reduce the network's error. The algorithm utilized for ANN training is Bayesian regularization backpropagation, wherein the error between the predicted and desired outputs is computed, followed by a backward step to adjust network parameters and minimize the error. Bayesian regularization is employed to ensure that the trained network exhibits good generalization qualities. Additional details regarding ANN architecture and training procedures can be found in [174], which serves as a reference for this study. Detecting the presence, quantifying, and locating damage through free vibration analysis necessitates an extensive training database for the neural network, including dynamic parameters of the structure. Consequently, a considerable number of analyses must be conducted. The adoption of the CW

	Component 1	Component 2	Component 3	Component 4
Sample 1	0.12	0.00	0.15	0.21
Sample 2	0.20	0.07	0.01	0.15
Sample 3	0.03	0.05	0.17	0.14
Sample 4	0.22	0.12	0.02	0.00
Sample 5	0.16	0.15	0.01	0.09
...		...	...	
...		...	...	
Sample N	0.14	0.04	0.18	0.12

Table 9.3 Example of database of N samples for a 4-Component structure. The damage introduced for each component is indicated in terms of stiffness reduction (1-d).

formulation is crucial for achieving highly accurate analysis at reduced computational costs, with the added benefit of localized damage detection at the component level.

The training database is established via Monte Carlo simulations based on the CW approach. Damage intensity is randomly assigned to each component, following a Gaussian distribution with a mean of 0 and a standard deviation of 0.1. Consequently, a database comprising N structures, covering a broad spectrum of potential damage scenarios, is assembled. An illustrative example of such a database for a structure with four components is presented in Table 9.3. Subsequently, free vibration analyses are conducted for all samples. The Artificial Neural Network (ANN) utilizes the first natural frequencies and MAC scalars of each structure for its training process. Once trained, the neural network can analyze new structures with different damage distributions. By inputting the first natural frequencies and MAC scalars of a structure, the ANN can predict the location and intensity of all damages. The accuracy of this prediction hinges on the ANN architecture. Some studies attempt to optimize the ANN architecture through design optimization methods [175, 176]. However, there is no definitive and universally proven method for defining all parameters beforehand. Therefore, in this study, the network architecture was primarily developed through a trial-and-error approach, contingent upon the specific problem under investigation. Parameters such as the number of hidden layers and neurons per layer were involved in this process. Fig. 9.8 depicts a flow chart outlining the entire process of vibration-based damage detection, from CW modeling of a structure to ANN testing.

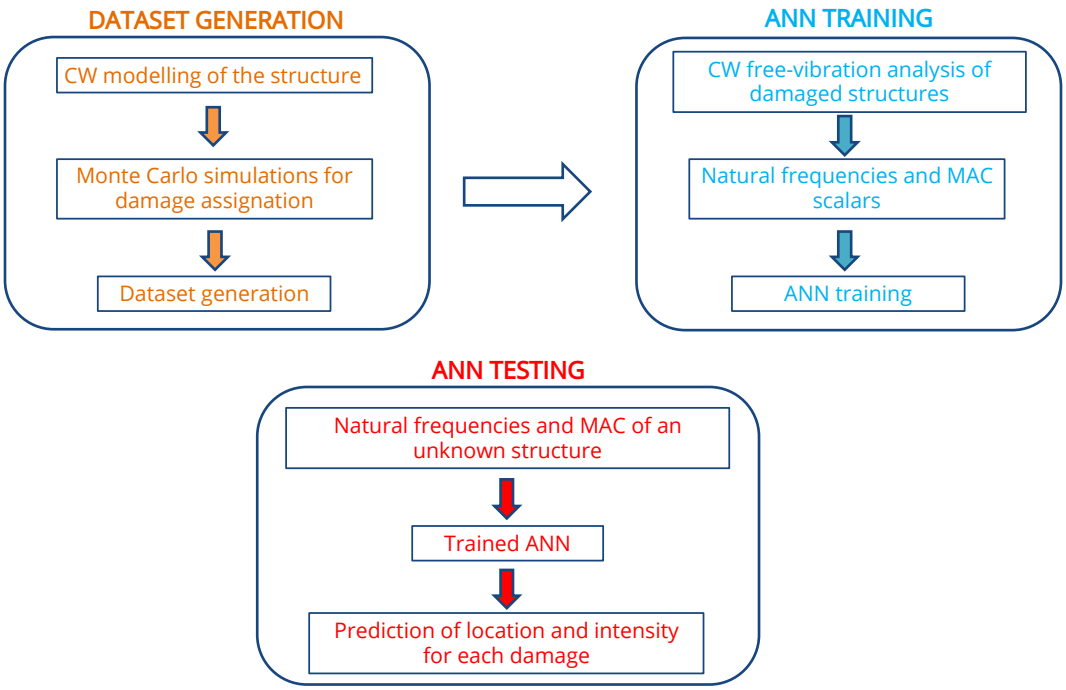

Fig. 9.8 Flowchart illustrating the comprehensive process for damage detection, spanning from the structural modeling phase to the training of the ANN.

9.2 Strain and displacement-based damage detection

The vibration-based damage detection approach presented in Section 9.1 has been applied to composite laminates [97]. Nevertheless, the results are not as promising as previous studies on thin-walled structures. This was mainly due to the monolithic nature of laminates, leading to the necessity of higher frequency mode computation to obtain sufficient information for damage detection. Furthermore, the actual measurement of natural frequencies does not represent an easy task to perform, especially if precise values and high-frequency modes are needed. For these reasons, virtually generated displacement and strain images retrieved by CUF-based analyses have been used to train a Convolutional Neural Network (CNN). The final objective is the complete mapping of damage in a composite structure.

9.2.1 Architecture

A convolutional neural network is a specific deep learning architecture [177], well-suited for image processing tasks. The key advantage of CNNs over traditional

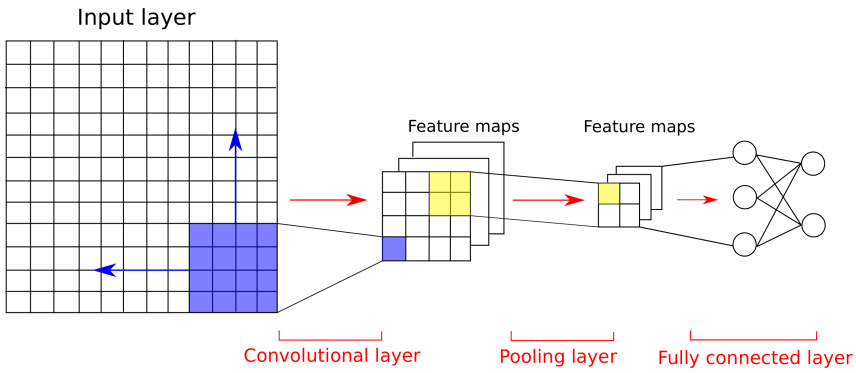

Fig. 9.9 Example of CNN architecture.

neural networks lies in their ability to handle high-dimensional inputs and mitigate overfitting. This is achieved through the local connectivity characteristic of CNNs, where each hidden unit is connected to a subset of the previous layer, reducing the number of learnable parameters and computational demands during training. Additionally, CNNs exhibit robustness to input translation and distortion [92]. CNNs are designed to process three-dimensional inputs, and their architecture typically comprises three main layers. Convolutional layers utilize two-dimensional learnable filters that slide over the input layer, computing dot products with small regions of the input to generate feature maps. These feature maps serve as inputs to subsequent layers. Subsequently, pooling layers perform downsampling operations using maximum or average operations. Finally, the fully connected layer computes the weighted sum of inputs similar to classical feedforward neural networks. Regularization techniques are commonly employed during CNN training to enhance model generalization to unseen data. In this work, dropout regularization and batch normalization layers are utilized. Fig. 9.9 illustrates an example of a CNN architecture.

9.2.2 Simulation-driven CNN training process

The capabilities of CUF and the component-wise formulation are once again used to conduct numerous analyses with high accuracy while minimizing computational resources. A database is constructed using CUF-based Monte Carlo simulations, wherein damage intensity is randomly assigned to each component, following a Gaussian distribution with a mean and standard deviation of 0.1. Consequently, a database comprising N samples is compiled to encompass a wide range of potential damage distributions. Unlike Section 9.1, orthotropic damage is considered in

	Component 1		Component 2		Component 3	
	d_1	d_2	d_1	d_2	d_1	d_2
Sample 1	0.11	0.20	0.02	0.01	0.16	0.23
Sample 2	0.23	0.05	0.24	0.06	0.00	0.14
Sample 3	0.02	0.15	0.034	0.06	0.15	0.12
...		...		...	...	...
...		...		...	...	...
Sample N	0.11	0.05	0.11	0.14	0.08	0.02

Table 9.4 Example of database of N samples for the three-component structure shown in Fig. 8.1. The damage introduced for each component is indicated in terms of longitudinal (d_1) and transversal (d_2) stiffness reduction.

this study. An illustrative example of such a database is presented in Table 9.4. Subsequently, a component-wise simulation of each damaged structure is conducted. The training process will entails feeding the CNN with representative displacement and strain field images. Finally, the accuracy of the CNN in predicting damage location and intensity is assessed using images of potentially damaged and unseen structures. A flowchart outlining the entire process is depicted in Fig. 9.10.

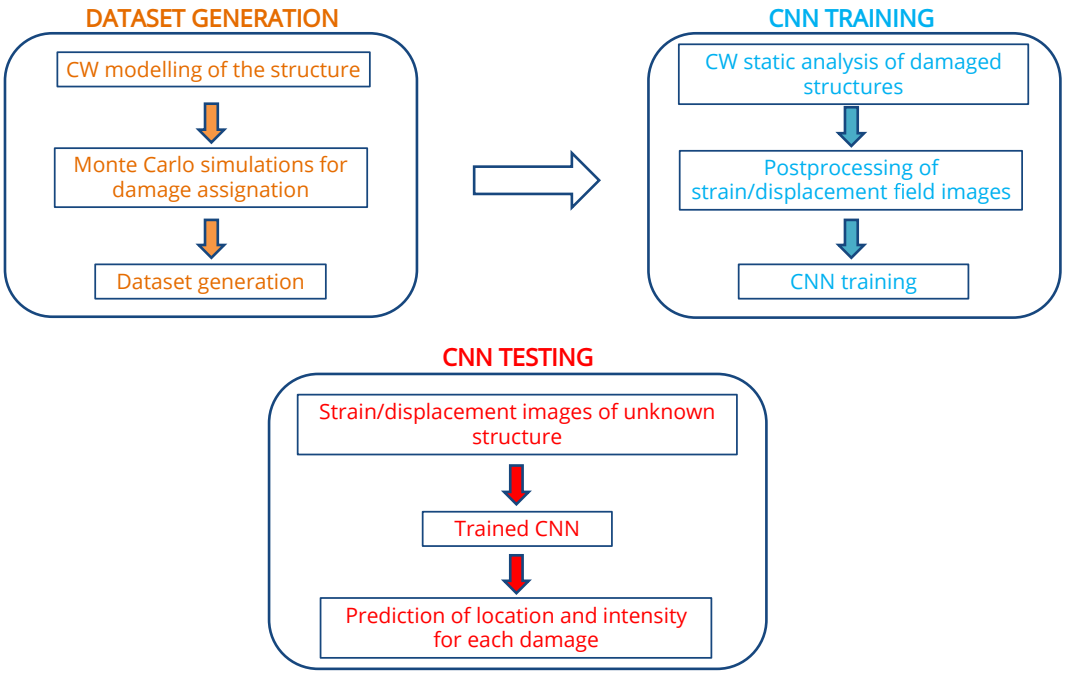

Fig. 9.10 Flowchart illustrating the comprehensive process for damage detection, spanning from the structural modeling phase to the training of the CNN.

Chapter 10

Numerical results on damage detection

This chapter proposes a selection of numerical examples obtained adopting the formulations and damage detection techniques presented in chapters 8 and 9. First, the vibration-based method is applied to aeronautical thin-walled structures, particularly to a stringer and a wing. In these cases, a simplified isotropic damage is considered. Then, convolutional neural networks are employed to predict damage location and intensity using displacement and strain field images as training database in composite laminates. For these assessments, both isotropic and orthotropic damage modelling are used.

10.1 Vibration-based method

This section introduces the damage detection results for the aeronautical structure previously introduced in Section 9.1, where the influence of damage on the vibrational response was investigated. The inverse problem is solved using ANN and a virtually generated training database.

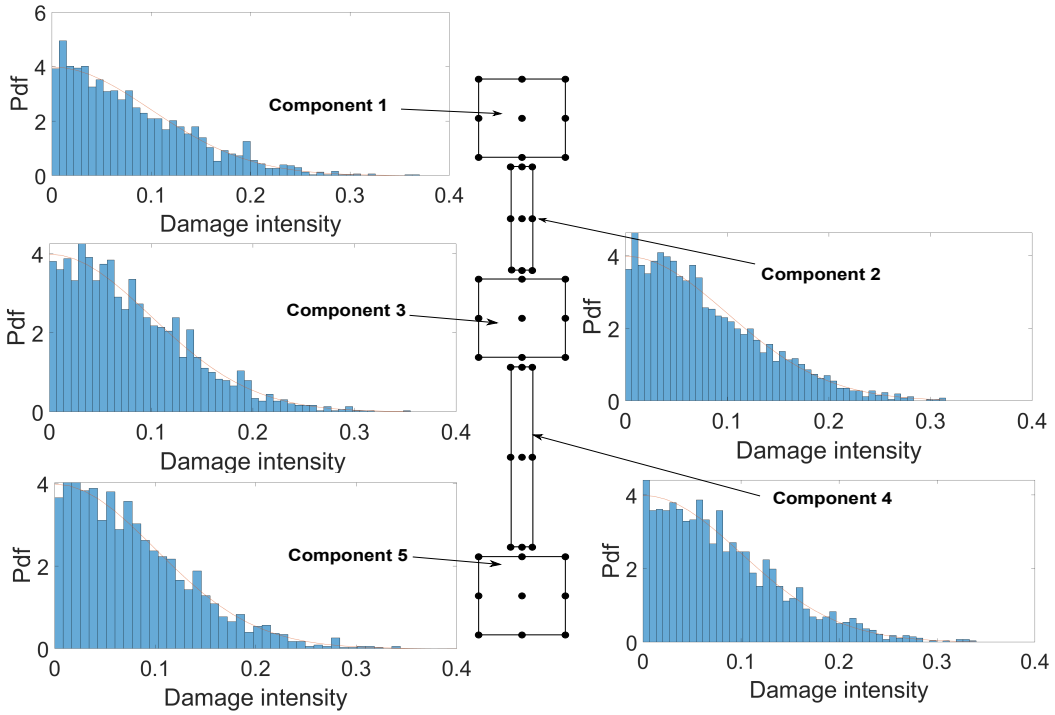

Fig. 10.1 Modeling of the three-stringer spar using the CW approach, along with the depiction of the Gaussian distribution representing the damage intensity for each component.

10.1.1 Three-stringer spar

The first case study is the three-stringer spar. Geometrical dimensions, modelling features and material properties are those listed in Section 9.1.1. The finite element model along the longitudinal axis consists of ten B4 elements. The CW model is composed of five L9 elements representing each component of the beam cross-section, as illustrated in Fig. 10.1. The probability density function of the damage intensity for each component is also depicted. A sensitivity analysis has been conducted to determine the architecture of the ANN. Two parameters have been investigated: number of hidden layers (Nl) and number of neurons for each layer (Nn). A training database of 2000 samples has been used. The results of this study are presented in Fig. 10.2. Each bar on the graph represents a simulation employing a different neural network, trained using the MATLAB toolbox [178]. The horizontal axis denotes the variable paramete, while the other parameter is held constant. The vertical axis indicates the Mean Squared Error (MSE) obtained when the trained

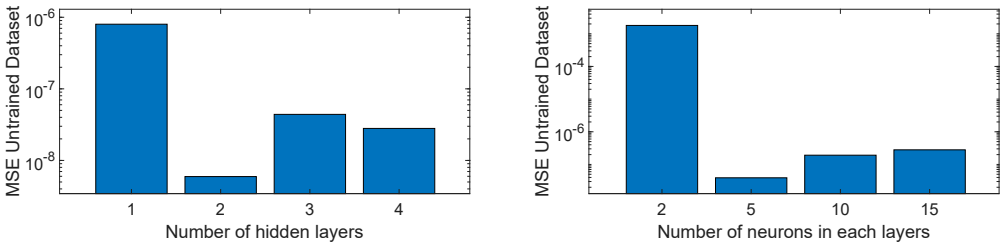

Fig. 10.2 (a) Influence of number of layers (Nn=5); (b) Influence of number of neurons per layer (Nl=1).

network is fed with dynamic parameters from an unseen structure. It reads:

$$MSE = \frac{\sum_{i=1}^{n}(y_i - \hat{y}_i)^2}{n}$$

where y_i represent the target and $\hat{y}_i$ the output of the network. It serves as a performance metric indicating the accuracy of the neural network in predicting the desired output. Lower MSE values signify better predictive capability of the neural network. It's worth noting that increasing the number of neurons and layers escalates the computational cost for training the neural network. From Fig. 10.2, it is evident that the optimal balance between performance and computational cost is achieved when the ANN comprises two hidden layers with five neurons each. It's important to emphasize that only networks with an equal number of neurons per layer were considered.

Consequently, the results presented hereafter have been found with a dataset of 2000 samples and a neural network consisting of two hidden layers, each comprising five neurons.

The network's performance is depicted in Fig. 10.3. The coefficient R represents the correlation coefficient, indicating the degree of association between the predicted output and the targets. It ranges from 0 to 1, where a value of 1 means perfect alignment between the predicted output and the targets. It's notable that this ANN achieves remarkably high accuracy in predicting both the location and intensity of damage in a three-stringer spar. Figures 10.4, 10.5, and 10.6 illustrate the comparison between the ANN's predictions (Blue Bars) and the solutions obtained through the CUF formulation (Red Bars). The components are labeled on the horizontal axis according to the structure's partition shown in Fig. 10.1, while the vertical axis represents the damage intensity. In Fig. 10.4, only one component of the structure is

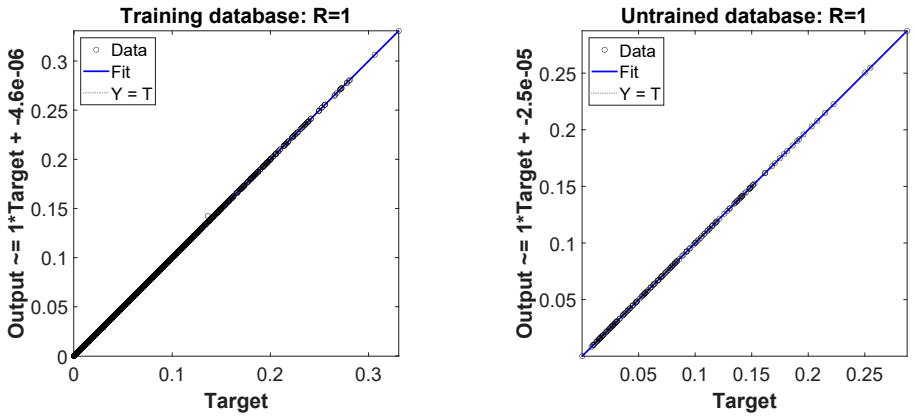

Fig. 10.3 Performance of the ANN with two hidden layers each containing five neurons, for a three-stringer spar geometry.

damaged, while in Fig. 10.5, a maximum of two components can be simultaneously damaged. In Fig. 10.6, all components are damaged simultaneously. When damage is introduced across multiple components, its severity can vary from one component to another. The samples depicted in these figures exhibit damage distributions distinct from those used during the training process. Another important observation regarding the results presented in Fig. 10.4 and Fig. 10.5 is the ANN's ability to identify the damaged component(s) and their corresponding intensity, even when only one or two components are affected.

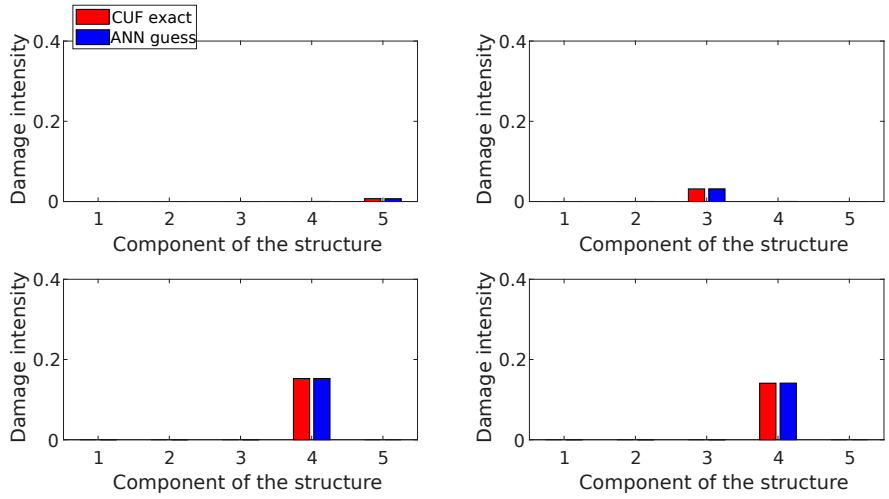

Fig. 10.4 Comparison between the exact CUF solution (Red bars) and the ANN output (Blue bars) for a three-stringer spar. Each graph illustrates a structure with only one damaged component.

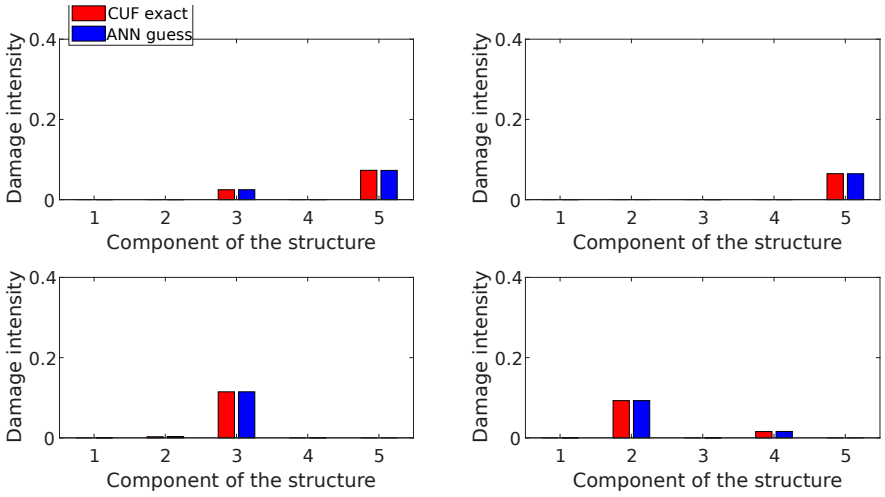

Fig. 10.5 Comparison between the exact CUF solution (Red bars) and the ANN output (Blue bars) for a three-stringer spar. Each graph illustrates a structure with a maximum of two components damaged, with the level of damage potentially differing between components.

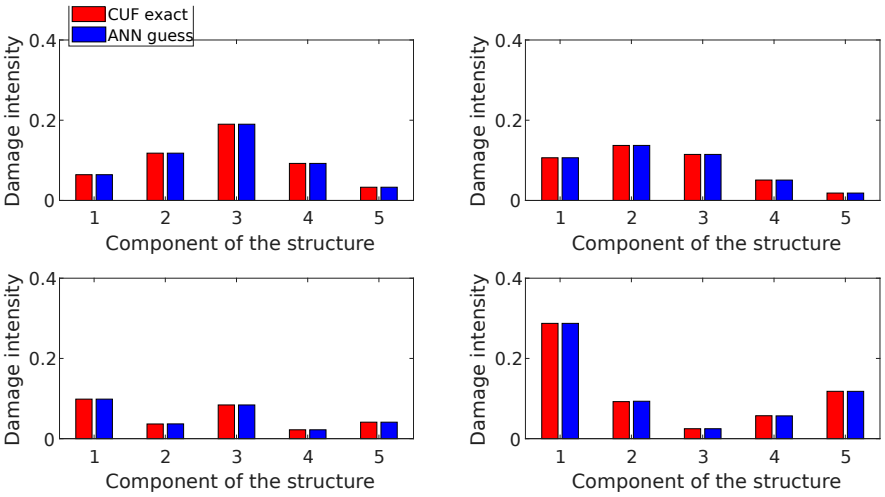

Fig. 10.6 Comparison between exact the CUF solution (Red bars) and the ANN output (Blue bars) for a three-stringer spar. Each graph illustrates a structure with all components damaged, with the level of damage potentially differing between components.

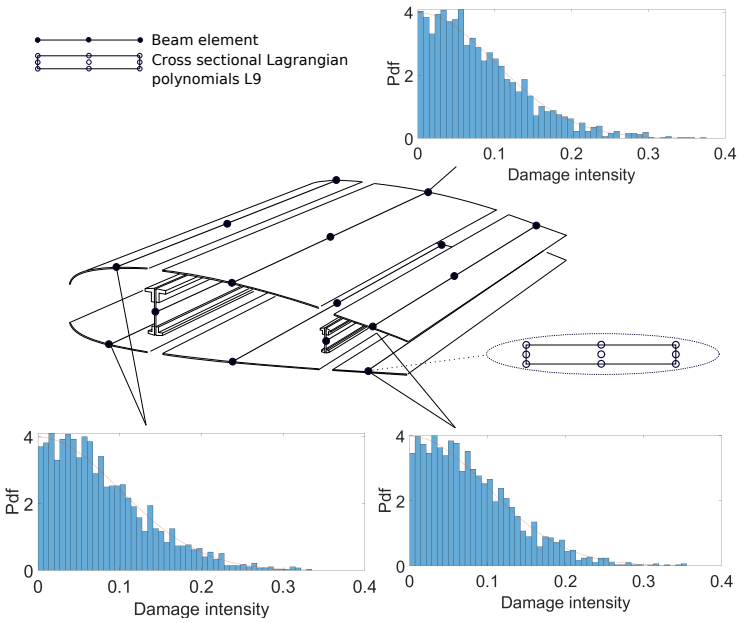

Fig. 10.7 CW model of a NACA profile wing and depiction of the Gaussian distribution of the damage intensity for certain components.

10.1.2 NACA Profile wing

The second assessment involves the wing discussed in Section 9.1.1. Similar to the previous case test, the CW model is employed. Each longeron, panel, leading, and trailing edge are meshed separately, as depicted in Fig. 10.7. Along the longitudinal axis, nine B4 elements are utilized for discretization, while a combination of L3, L4, and L9 elements is employed for the cross-section. The figure also displays the probability density function of the damage intensity for selected components. The use of the CW formulation enables the treatment of each bay individually. This means that a portion of the longeron in one bay can be damaged while the others remain intact, resulting in a more precise localization of damage within the structure. Consequently, a total of 18 components can potentially be damaged, six for each bay. The components for each bay are delineated in Fig. 10.8: Leading edge (Component 1), top panel (Component 2), trailing edge (Component 3), rear longeron (Component 4), bottom panel (Component 5), and front longeron (Component 6). No damage is introduced in the three ribs since even minor damage to a rib should not occur during typical operating conditions of this structure. The training dataset for the ANN comprises 2000 samples, with each sample representing a structure with a distinct damage distribution. The initial network architecture tested is identical to that used

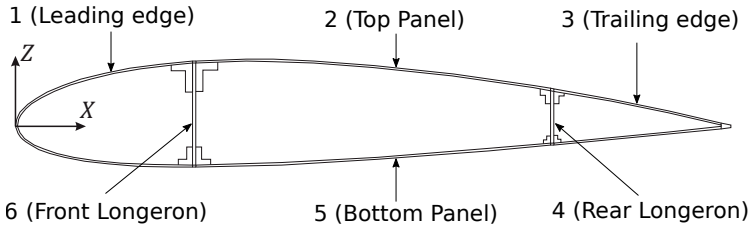

Fig. 10.8 Cross-section of the NACA profile wing with the enumeration of the components for a single bay.

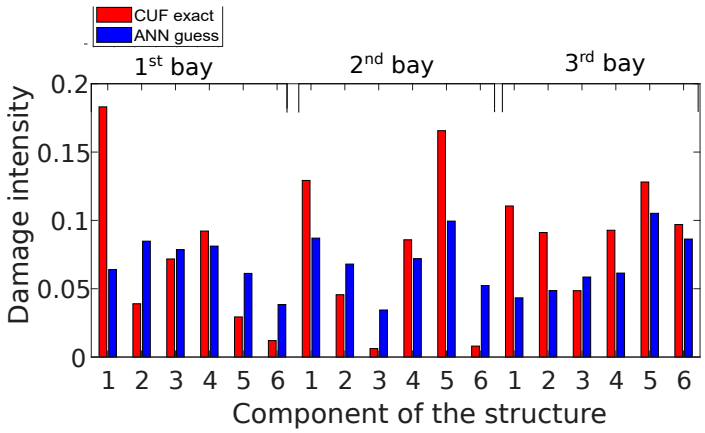

Fig. 10.9 Comparison between the exact CUF solution (Red bars) and the non-optimized ANN (Blue bars) for a profile wing. The ANN architecture employed comprises two hidden layers with five neurons in each.

in the three-stringer spar case, consisting of two hidden layers with five neurons each. All 18 components are simultaneously damaged, and the results are depicted in Fig. 10.9. The component numbers range from 1 to 6 for each bay, following the numbering scheme introduced in Fig. 10.8. Clearly, the network previously effective for the prior case test is inadequate for this problem. The correlation coefficient R is approximately 0.5, signifying diminished performance. The complexity of the FEM model has increased, with the number of involved components rising from 5 to 18. Hence, an iterative trial-and-error approach was undertaken to determine the optimal architecture. The resulting ANN comprises three hidden layers, each housing 28 neurons. Similar to the prior case test, the input and output consist of 15 natural frequencies plus the MAC scalars. Fig. 10.10 demonstrates the performance of this network, exhibiting remarkable accuracy in predicting damage location and intensity. A detailed examination reveals minimal discrepancies in predicting damage location and severity in components with minor defects. Figures 10.11 and 10.12 compare the CUF exact solution (Red bars) with the network's output (Blue bars) when one

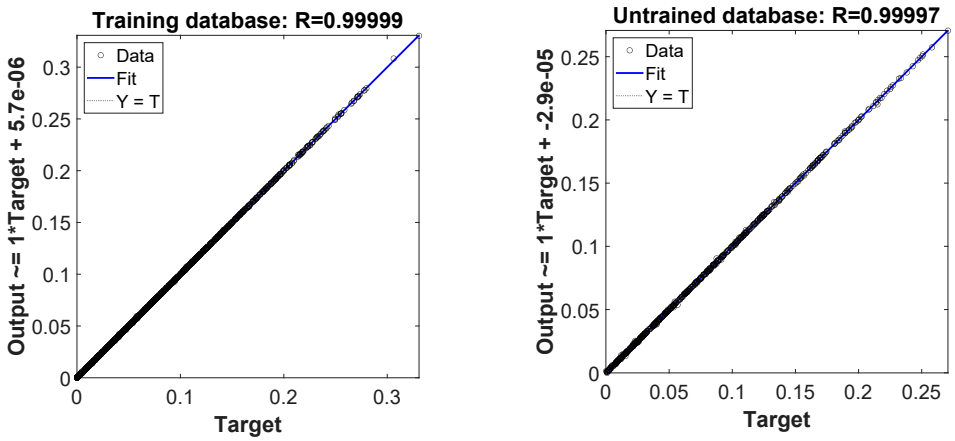

Fig. 10.10 Performance of the ANN with three hidden layers, each comprising 28 neurons, for a wing.

or two components were damaged, potentially spanning two different bays. The structures analyzed in these figures had damage distributions distinct from those used in training the ANN, indicating the network's ability to predict damage location and intensity with exceptional accuracy even in more complex structures like wing profiles. Figure 10.13 shows the results of the ANN when all components are damaged simultaneously. The same hypotheses have been made for figures 10.11 and 10.12.

10.2 Strain and displacement-based method

Figure 10.14 shows the architecture employed in this research. The field images adopted for training have a dimension of 413x413 pixels. Then, blocks formed by convolutional and average pooling layers were used before introducing fully connected ones. The final output of these layers will be the location and intensity of each damage in the investigated structure.

10.2.1 Composite plate with isotropic damage

The same composite laminate introduced in Section 8.2 is examined here for damage detection. Damage is introduced in each region of the structure using an isotropic formulation. In total, nine areas are identified, requiring the CNN to predict nine

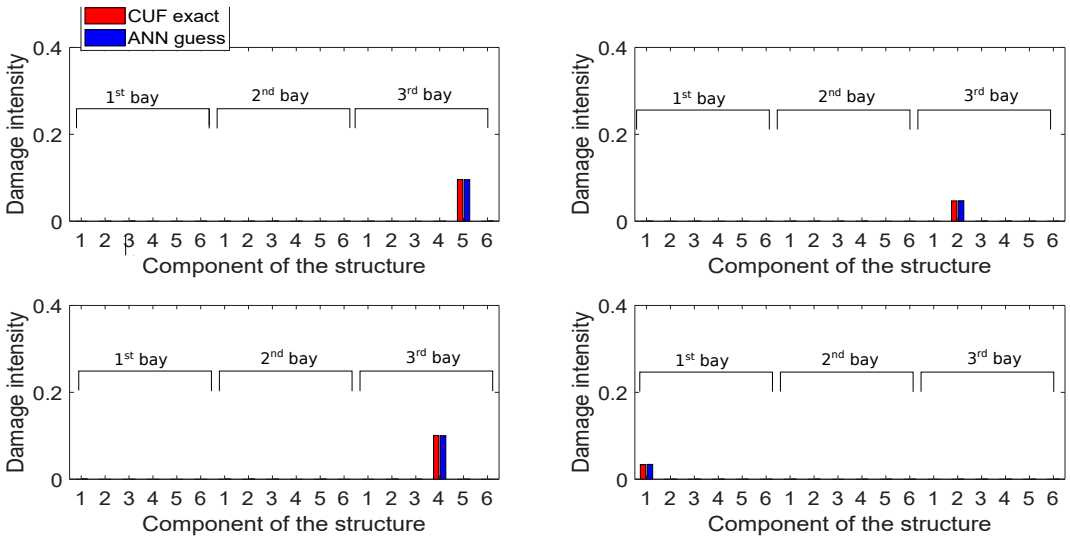

Fig. 10.11 Comparison between the exact CUF solution (Red bars) and the optimized ANN (Blue bars) for a profile wing. Each graph represents a structure with only one damaged component.

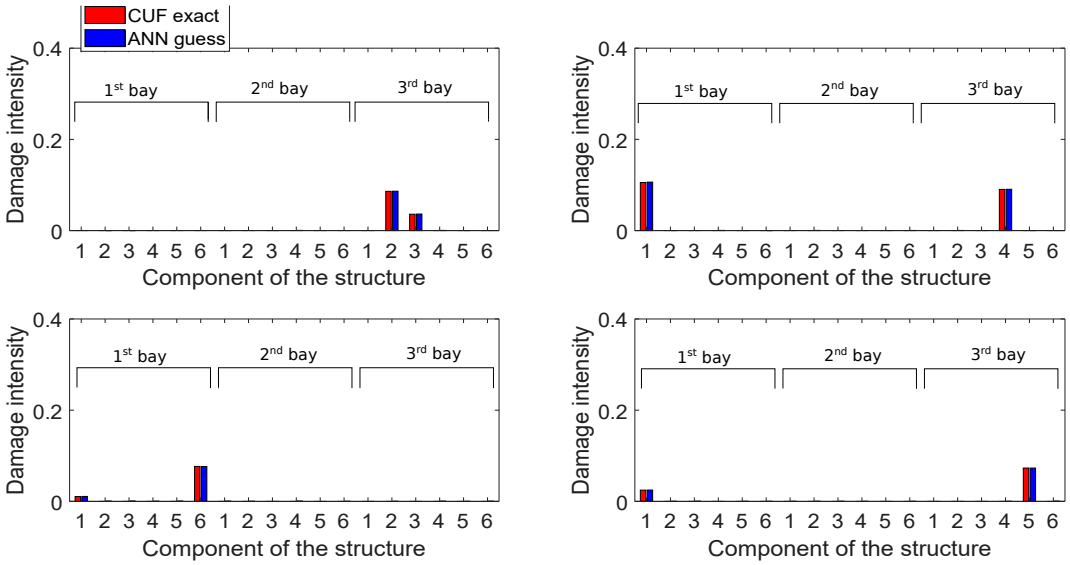

Fig. 10.12 Comparison between the exact CUF solution (Red bars) and the optimized ANN (Blue bars) for a profile wing. Each graph represents a structure with a maximum of two damaged components. The damage can vary from a component to another.

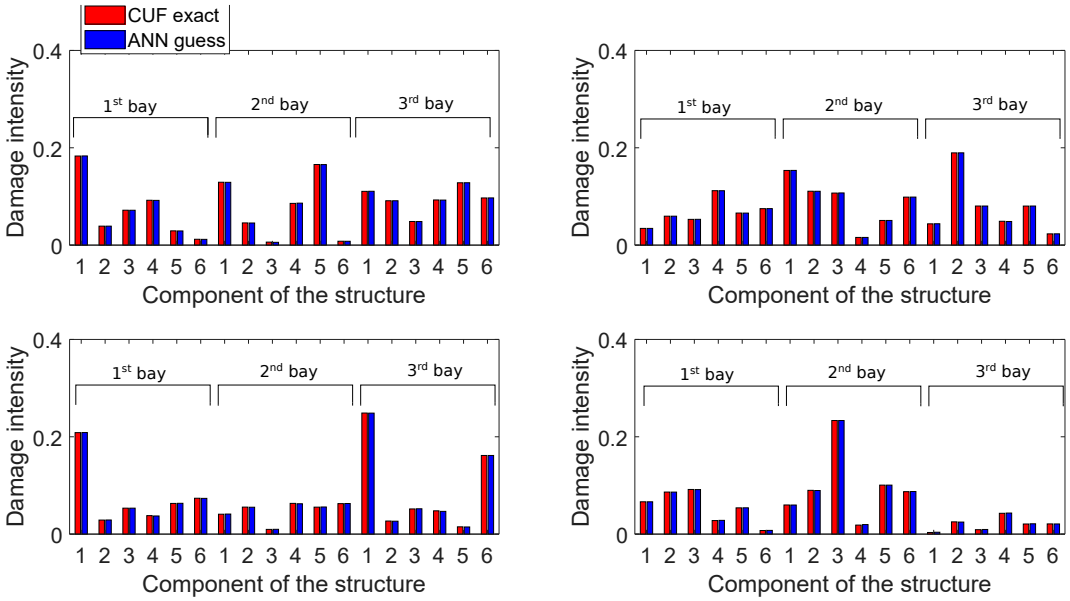

Fig. 10.13 Comparison between the exact CUF solution (Red bars) and the optimized ANN (Blue bars) for a profile wing. Each graph represent a structure with all components damaged. The damage can vary from a component to another.

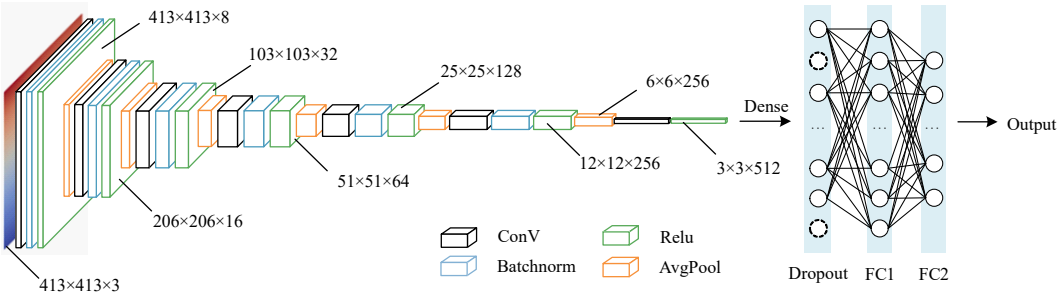

Fig. 10.14 CNN architecture employed in the present work.

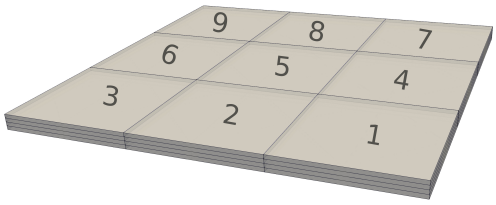

Fig. 10.15 Numbering of the regions for the investigated plate.

Number samples	Time elapsed	Regression coefficient
4000	17min 47sec	0.9785
6000	27min 08sec	0.9837
8000	36min 23sec	0.9865
10000	48min 18sec	0.9902

Table 10.1 Convergence study for the scenario considering isotropic damage model.

damage parameters d. These parameters are assigned through Monte Carlo simulation, with mean and standard deviation set to 0.1. It's noteworthy that the same damage is applied to each layer within a single region The boundary conditions consist of a uniaxial pressure applied on one edge, while the opposite edge remains clamped. Fig. 10.16 illustrates examples of images depicting two different damage scenarios: pristine and randomly damaged structures, respectively. The CNN will be fed numerous such images from structures with known damage distributions, with the ultimate aim of detecting damage in unseen structures. However, determining the appropriate number of images required for accurate prediction of damage intensity and severity necessitates a convergence study. The objective is to assess the minimum number of database samples needed to achieve the highest prediction accuracy possible. The proportion of sample numbers allocated to training, validation, and testing sets has been kept constant for all cases (i.e., 75%, 20%, and 5%, respectively). The CNN training process utilizes an NVIDIA GeForce GTX 1650 GPU. The results of the convergence study are displayed in Table 10.1. It is evident that a total of 4000 samples already ensures good prediction accuracy by the CNN, with a regression coefficient of 0.9785. While increasing the number of adopted samples enhances prediction accuracy, it also escalates the computational time required for CNN training. Hence, a trade-off between accuracy and computational time needs to be determined based on the specific application requirements. Thereafter, results are presented for the scenario involving 10000 database samples. A total of 500

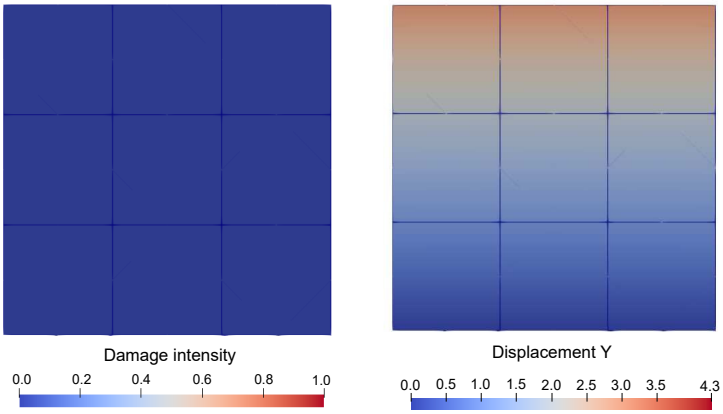

(a) Pristine structure

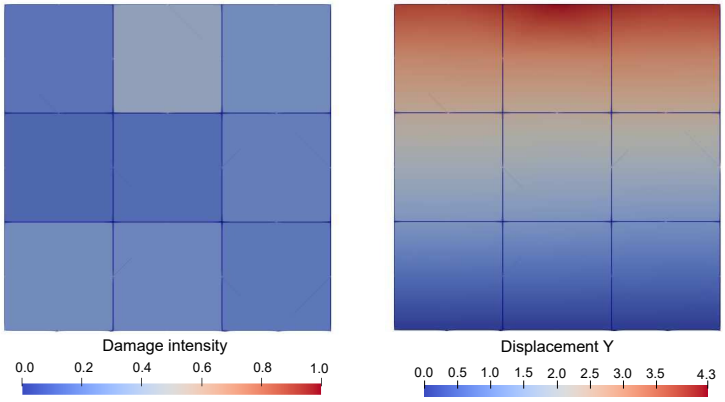

(b) Damaged structure

Fig. 10.16 Longitudinal displacement fields of a pristine and damaged structure considering the isotropic damage model.

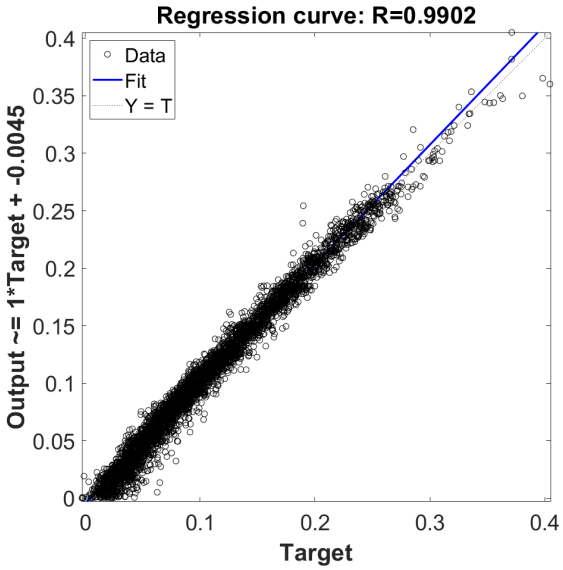

Fig. 10.17 Regression curve for the case with isotropic damage model.

unknown structures were input into the trained neural network to validate its ability to ascertain the location and intensity of damage in each structure. The regression curve depicted in Fig. 10.17 showcases a regression coefficient R near unity, indicating high accuracy in predicting the correct values of the CNN targets (i.e., damage). Figure 10.18 provides a comparison between the target value of damage intensity (red bars) and the CNN prediction in each region of the structure (blue bars) for two test samples, which are unfamiliar to the CNN. The vertical axis represents the intensity of the damage, while the horizontal axis displays the numbering of the regions, consistent with the partitioning illustrated in Fig. 10.15.

10.2.2 Composite plate with orthotropic damage

The previous case study, with the same boundary and load conditions, is replicated here for the detection of orthotropic damages. Reduction factors d_1 (representing longitudinal damage) and d_2 (representing transversal damage) are introduced in each of the nine regions through Monte Carlo simulations. Each layer within the same region will experience the same damage intensities. Therefore, the aim is now to predict the values of nine longitudinal damages d_1 and nine transversal damages d_2.

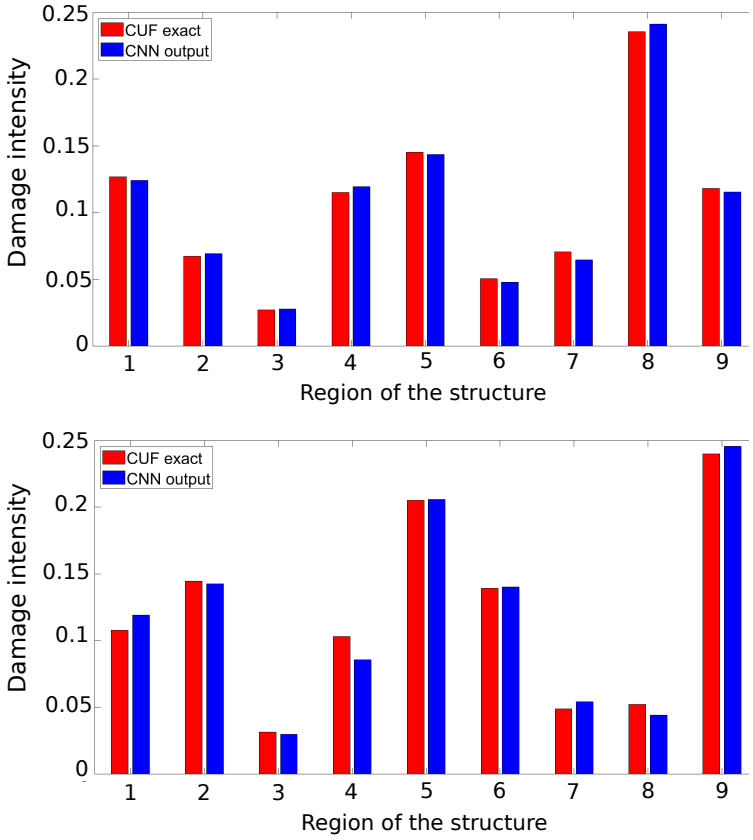

Fig. 10.18 Comparison between the target value and the CNN prediction in structures where all regions are damaged, considering the isotropic damage model.

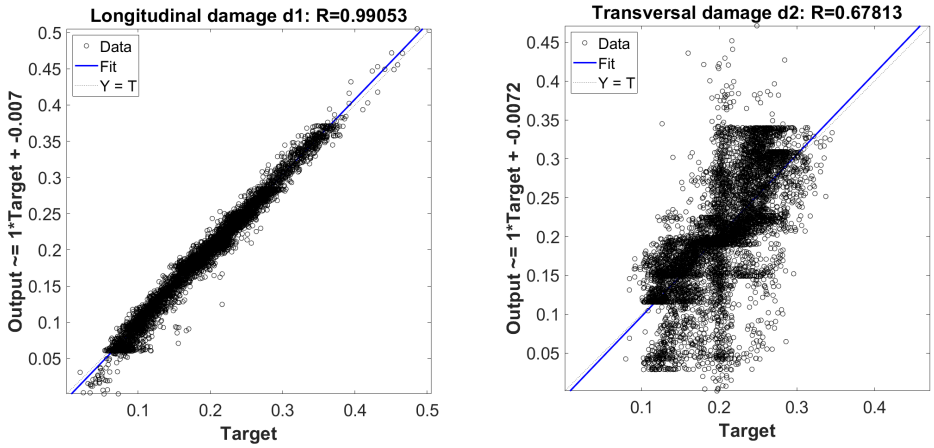

Fig. 10.19 Regression curve for the orthotropic damage model scenario using longitudinal displacement images.

Initially, longitudinal displacement field images were chosen for network training. The network architecture remained the same as in the isotropic damage case, with the only modification being the output layer now having 18 neurons instead of nine. The outcomes for both longitudinal and transversal damages are depicted in Fig. 10.19. The CNN effectively detects longitudinal damage d_1 with significant accuracy in all nine involved regions. However, the network struggles notably in predicting transversal damage d_2. This outcome could have been anticipated in advance. By utilizing only images of the axial displacement fields, the CNN can only discern information strictly related to longitudinal damage d_1, while limited or no information is available regarding the influence of transversal damage d_2 on the structural behavior. Consequently, this choice of training images cannot be deemed appropriate for the present case. To address the problem with orthotropic damage formulation, a different approach is adopted. For each training sample, a set of two images is introduced as input: the longitudinal displacement field u_y and the normal strain field ε_{xx}. An example of training images from a randomly damaged sample is depicted in Fig. 10.20. The objective is to provide the CNN with sufficient information to accurately predict both d_1 and d_2 parameters. Once the network training is complete, the test images from unseen structures are fed into the CNN for damage prediction. The results are illustrated in Fig. 10.21. It can be observed that the CNN maintains its ability to accurately predict the longitudinal damage d_1, while a noticeable enhancement is observed in the prediction of the transversal damage d_2. However, it is evident that the CNN's performance in predicting d_2 is not as

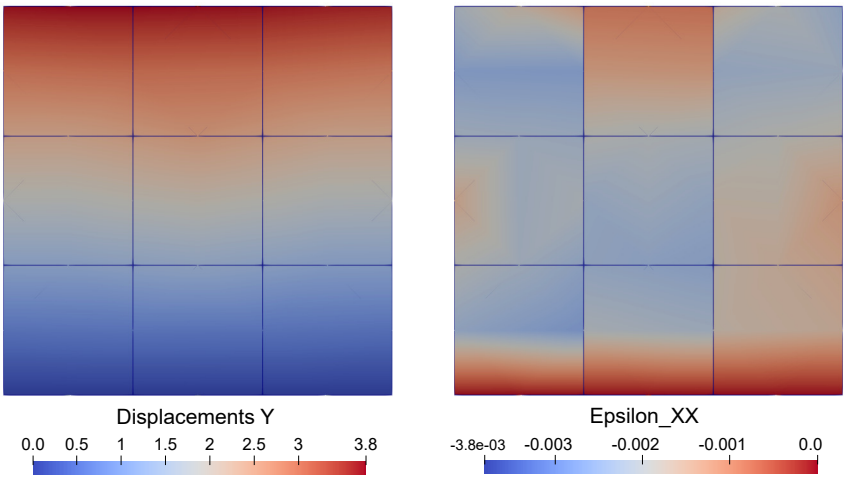

Fig. 10.20 Example of axial displacement and normal strain field images depicting a randomly damaged structure in the scenario of the orthotropic damage model.

N samples	Time elapsed	Regression coeff. d_1	Regression coeff. d_2
8000	48min11sec	0.9577	0.8809
10000	58min55sec	0.9731	0.8848
12000	73min27sec	0.9798	0.9165
14000	96min24sec	0.9845	0.9276

Table 10.2 Convergence study for the case with orthotropic damage model.

robust as for the d_1 parameter, with a regression coefficient of 0.927 compared to the value of 0.984 for the longitudinal parameter. Subsequently, a convergence study was conducted to explore the influence of the number of training samples on the results. The findings are presented in Table 10.2. It is clear from these results that there is an improvement in accuracy as the number of samples increases. Therefore, a larger database could potentially lead to better predictions, even for the transversal damage parameters.

Similar to the isotropic formulation case, a comparison between the network output (blue bars) and the target prediction (red bars) is illustrated in Fig. 10.22. The left graph pertains to the longitudinal damages for each of the nine regions, while the right graph pertains to the transverse damage parameters.

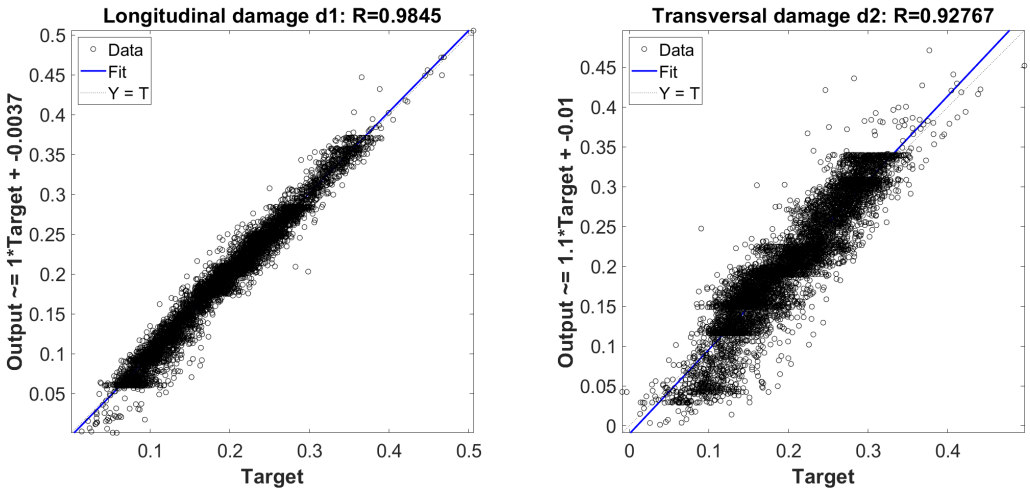

Fig. 10.21 Regression curve for the scenario featuring the orthotropic damage model, utilizing longitudinal displacement and normal strain images.

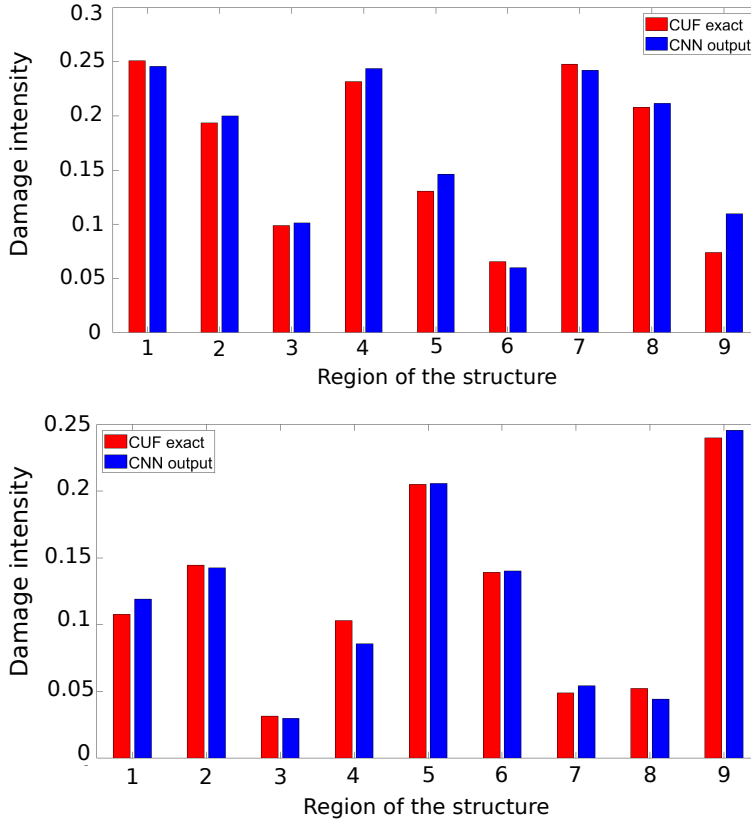

Fig. 10.22 Comparison between the target value and the CNN guess in a structure where all regions are damaged, using the orthotropic damage model.

Chapter 11

Conclusions

The present thesis proposes a series of techniques for the characterization of failure in isotropic and composite structures, from damage identification to the analysis of its propagation. The capabilities of the Carrera Unified Formulation (CUF) have been exploited to carry out progressive failure, global/local and damage detection analyses. CUF allows straightforward implementation of low to high order theories in a compact and automatic way. Within the CUF framework, the governing equation and the related finite element (FE) arrays of any model are formulated through Fundamental Nuclei (FNs), whose structure is independent of the theory approximation order. Furthermore, the use of Lagrange expansion (LE) permits the adoption of a Component Wise (CW) approach for structural modelling. First, a three-dimensional (3D) orthotropic damage model has been employed for progressive failure analysis in fibre-reinforced composites. The results have been validated with outcomes coming from literature and experimental campaigns. The framework has proven to provide accurate solutions in terms of damage progression and structural responses in a highly efficient manner. Then, CUF-based finite elements were coupled with a non-classical theory, peridynamics (PD). PD is a non-local theory based on integro-differential equations, which allows the formulation to deal with discontinuities, such as cracks. Two approaches have been proposed, and the advantages and shortcomings are highlighted. This framework has been employed for static and progressive failure analyses. Coupled FEM-PD models have been embedded within a global/local tool for localized progressive failure analysis. The two-step global/local approach has given reliable results regarding stress states and failure index evaluations, even considering local regions of complex structures, such

as an aeronautical wing. By introducing the coupled FEM/PD approach at the local scale, a localized progressive failure analysis in a specific region of a large structure is made possible. Finally, the potentialities of CUF have been exploited for damage detection in both isotropic metallic and composite structures. CUF-based finite element analyses are carried out in order to create an extensive database for training of Artifical (ANN) and Convolutional (CNN) Neural networks. These are fed with static or dynamic structural parameters to obtain a complete mapping of damages in an unknown structure as output.

Main results

The main novelties and results obtained during this period of the doctoral research can be summarized as follows:

- CUF-based finite element models have been presented and used for failure analysis in composite laminates by means of an orthotropic Hashin-based damage model;
- The proposed damage model has proven to correctly reproduce the damage distribution in the investigated structures, including some 3D effects that 2D models could not describe. Furthermore, the combination with CUF led to a significant reduction of the computational costs, though maintaining a high level of accuracy when results are compared with experimental and numerical campaigns;
- The non-classical peridynamics theory has been coupled with higher-order finite elements. Two methods have been proposed, and their advantages and shortcomings are enlisted. However, the adoption of these coupling approaches has solved some limitations of the peridynamic formulation, such as the exponential increase in the computational demand due to its non-local nature and the difficulties in correctly imposing boundary conditions on the PD domain;
- The intrinsic non-local nature of peridynamics has been exploited for progressive failure analysis in quasi-brittle structures. The coupling with refined elements has allowed using the peridynamic grid only in regions where the

crack was more likely to nucleate and propagate. The outcomes have been compared with results from the literature, showing good agreement in terms of structural response and description of damage propagation;

- A global/local tool has been extended to deal with larger domains. The global analysis is carried out in a commercial FEM software (Nastran). Then, a region to be locally refined is chosen and a local analysis through CUF-based finite element models is performed. The results have proven consistent with those obtained by modelling the entire structure with higher-order elements.
- An innovative framework for localized progressive failure analysis has been proposed. PD for crack propagation has been embedded within the global/local tool, showing some good preliminary results for simple benchmark cases.
- The capabilities of CUF in modelling structures in a component-wise manner have been exploited for dealing with damage detection. The need for higher-order elements to accurately evaluate damage effects has been demonstrated.
- A vibration-based damage detection method has been developed. An artificial neural network is fed with vibrational characteristics (natural frequencies and MAC matrix) of damaged structures. After training, the network is able to provide the location and intensity of each damage of an unknown structure.
- The damage modelling has been extended to deal with orthotropic damages. An alternative method has been proposed for detection in composite laminates. A convolutional neural network is trained with images of displacement and strain fields of the composite laminate.

Future works

The work presented in this thesis can represent a first step towards interesting developments. Within the present research, the CUF has shown good performance in progressive failure and damage detection analysis, thus paving the way for future research, including:

- the extension of coupled FEM-PD model to deal with failure in different materials, such as composite laminates;

- the extension of the global/local approach for dealing with localized progressive failure in composite laminates, by using the Hashin-based orthotropic damage model proposed in this research;
- the integration of the global/local approach within an optimization framework for aircraft design;
- the adoption of hybrid (experimentally and numerically generated) data as database to train the neural networks for damage detection purposes.
- the development of a framework where the global/local approach is used in combination with deep learning algorithm for dealing with both detection of damage and investigation of its progression.

References

[1] Z. P Bažant and B.H. Oh. Crack band theory for fracture of concrete. *Matériaux et construction*, 16:155–177, 1983.

[2] L. M Kachanov. Rupture time under creep conditions. *International journal of fracture*, 97(1-4):11–18, 1999.

[3] J. Lemaitre and J.L. Chaboche. *Mécanique des matériaux solides*. 1988.

[4] D. Krajcinovic. Continuous damage mechanics revisited: Basic concepts and definitions. *Journal of Applied Mechanics*, 52(4):829–834, 1985.

[5] R. Talreja. A continuum mechanics characterization of damage in composite materials. *Proceedings of the Royal Society of London. A. Mathematical and Physical Sciences*, 399:195 – 216, 1985.

[6] R. Talreja. Damage characterization. In *Composite Materials Series*, volume 4, pages 79–103. Elsevier, 1991.

[7] A. L. J. T. R. Matzenmiller, J. Lubliner, and R. L. Taylor. A constitutive model for anisotropic damage in fiber-composites. *Mechanics of materials*, 20(2):125–152, 1995.

[8] P. Ladeveze and E. LeDantec. Damage modelling of the elementary ply for laminated composites. *Composites Science and Technology*, 43(3):257–267, 1992.

[9] P. Ladevèze, O. Allix, J. F. Deü, and D. Lévêque. A mesomodel for localisation and damage computation in laminates. *Computer Methods in Applied Mechanics and Engineering*, 183(1):105–122, 2000.

[10] M.F.S.F de Moura and J.P.M Gonçalves. Modelling the interaction between matrix cracking and delamination in carbon–epoxy laminates under low velocity impact. *Composites Science and Technology*, 64(7):1021–1027, 2004.

[11] S.R. Hallett, W. Jiang, B. Khan, and M. R. Wisnom. Modelling the interaction between matrix cracks and delamination damage in scaled quasi-isotropic specimens. *Composites Science and Technology*, 68(1):80–89, 2008.

[12] X.C. Sun, M.R. Wisnom, and S.R. Hallett. Interaction of inter- and intralaminar damage in scaled quasi-static indentation tests: Part 2 – numerical simulation. *Composite Structures*, 136:727–742, 2016.

[13] J. Reiner, M. Veidt, M. Dargusch, and L. Gross. A progressive analysis of matrix cracking-induced delamination in composite laminates using an advanced phantom node method. *Journal of Composite Materials*, 51(20):2933–2947, 2017.

[14] H.W. Wang, H.W. Zhou, H.W. Ji, and X.C. Zhang. Application of extended finite element method in damage progress simulation of fiber reinforced composites. *Materials and Design*, 55:191–196, 2014.

[15] S.A. Silling. Reformulation of elasticity theory for discontinuities and long-range forces. *Journal of the Mechanics and Physics of Solids*, 48(1):175–209, 2000.

[16] J. Xu, A. Askari, O. Weckner, and S. Silling. Peridynamic analysis of impact damage in composite laminates. *Journal of Aerospace Engineering - J AEROSP ENG*, 21, 2008.

[17] S. Silling and A. Askari. Peridynamic model for fatigue cracking. 2014.

[18] Y. Ha and F. Bobaru. Studies of dynamic crack propagation and crack branching with peridynamics. *International Journal of Fracture*, 162:229–244, 2010.

[19] Y Ha and F. Bobaru. Characteristics of dynamic brittle fracture captured with peridynamics. *Engineering Fracture Mechanics*, 78(6):1156–1168, 2011.

[20] E. Madenci, K. Colavito, and N. Phan. Peridynamics for unguided crack growth prediction under mixed-mode loading. *Engineering Fracture Mechanics*, 167, 2016.

[21] S.A. Silling and E. Askari. A meshfree method based on the peridynamic model of solid mechanics. *Computers & structures*, 83(17-18):1526–1535, 2005.

[22] Q.V. Le and F. Bobaru. Surface corrections for peridynamic models in elasticity and fracture. *Computational Mechanics*, 61(4):499–518, 2018.

[23] F. Scabbia, M. Zaccariotto, and U. Galvanetto. A novel and effective way to impose boundary conditions and to mitigate the surface effect in state-based peridynamics. *International Journal for Numerical Methods in Engineering*, 122(20):5773–5811, 2021.

[24] F. Scabbia, M. Zaccariotto, and U. Galvanetto. A New Surface Node Method to Accurately Model the Mechanical Behavior of the Boundary in 3D State-Based Peridynamics. *Journal of Peridynamics and Nonlocal Modeling*, pages 1–35, 2023.

[25] G. Lubineau, Y. Azdoud, F. Han, C. Rey, and A. Askari. A morphing strategy to couple non-local to local continuum mechanics. *Journal of the Mechanics and Physics of Solids*, 60(6):1088–1102, 2012.

[26] F. Han and G. Lubineau. Coupling of nonlocal and local continuum models by the arlequin approach. *International Journal for Numerical Methods in Engineering*, 89(6):671–685, 2012.

[27] P. Seleson, S. Beneddine, and S. Prudhomme. A force-based coupling scheme for peridynamics and classical elasticity. *Computational Materials Science*, 66:34–49, 2013.

[28] P. Seleson, Y. Ha, and S. Beneddine. Concurrent coupling of bond-based peridynamics and the navier equation of classical elasticity by blending. *International Journal for Multiscale Computational Engineering*, 13(2), 2015.

[29] S. Silling, D. Littlewood, and P. Seleson. Variable horizon in a peridynamic medium. *Journal of Mechanics of Materials and Structures*, 10(5):591–612, 2015.

[30] W. Sun, J. Fish, and G. Zhang. Superposition of non-ordinary state-based peridynamics and finite element method for material failure simulations. *Meccanica*, 55, 2019.

[31] U. Galvanetto, T. Mudric, A. Shojaei, and M. Zaccariotto. An effective way to couple FEM meshes and Peridynamics grids for the solution of static equilibrium problems. *Mechanics Research Communications*, 76:41–47, 2016.

[32] M. Zaccariotto, T. Mudric, D. Tomasi, A. Shojaei, and U. Galvanetto. Coupling of FEM meshes with Peridynamic grids. *Computer Methods in Applied Mechanics and Engineering*, 330:471–497, 2018.

[33] S. P. Timoshenko and J. N. Goodier. *Theory of elasticity*. McGraw-Hill, 1970.

[34] L. Euler. Principia pro motu sanguinis per arterias determinando. *Opera posthuma mathematica et physica anno 1844 detecta*, 2:814–823, 1775.

[35] E. Reissner. The effect of transverse shear deformation on the bending of elastic plates. *Journal of Applied Mechanics*, 12(2):A69–A77, 1945.

[36] G. Kirchhoff. Über das gleichgewicht und die bewegung einer elastischen scheibe. *Journal Für die Reine und Angewandte Mathematik (Crelles Journal)*, 1850(40):51–88, 1850.

[37] E. Carrera. A class of two dimensional theories for multilayered plates analysis. *Atti Accademia delle Scienze di Torino, Memorie Scienze Fisiche*, 19-20:49–87, 1995.

[38] E. Carrera. Theories and finite elements for multilayered, anisotropic, composite plates and shells. *Archives of Computational Methods in Engineering*, 9(2):87–140, 2002.

[39] E. Carrera, M. Cinefra, M. Petrolo, and E. Zappino. *Finite Element Analysis of Structures through Unified Formulation*. John Wiley & Sons, Chichester, West Sussex, UK, 2014.

[40] M.H. Nagaraj, I. Kaleel, E. Carrera, and M. Petrolo. Elastoplastic micromechanical analysis of fiber-reinforced composites with defects. *Aerotecnica Missili & Spazio*, 101(1):53–59, 2022.

[41] A. Pagani, M. Enea, and E. Carrera. Quasi-static fracture analysis by coupled three-dimensional peridynamics and high order one-dimensional finite elements based on local elasticity. *International Journal for Numerical Methods in Engineering*, 123(4):1098–1113, 2022.

[42] A. Pagani and A.R. Sanchez-Majano. Influence of fiber misalignments on buckling performance of variable stiffness composites using layerwise models and random fields. *Mechanics of Advanced Materials and Structures*, 29(3):384–399, 2022.

[43] A. R. Sánchez-Majano, R. Azzara, A. Pagani, and E. Carrera. Accurate stress analysis of variable angle tow shells by high-order equivalent-single-layer and layer-wise finite element models. *Materials*, 14(21):6486, 2021.

[44] I. Kaleel, M. Petrolo, A.M. Waas, and E. Carrera. Micromechanical progressive failure analysis of fiber-reinforced composite using refined beam models. *Journal of Applied Mechanics*, 85(2), 2018.

[45] A. Pagani, R. Azzara, B. Wu, and E. Carrera. Effect of different geometrically nonlinear strain measures on the static nonlinear response of isotropic and composite shells with constant curvature. *International Journal of Mechanical Sciences*, 209:106713, 2021.

[46] A.G. de Miguel, A. Pagani, and E. Carrera. Structural health monitoring: Numerical simulation of Lamb waves via higher-order models. In *Advances in Predictive Models and Methodologies for Numerically Efficient Linear and Nonlinear Analysis of Composites*, pages 125–140. Springer, 2019.

[47] R. Azzara, E. Carrera, and A. Pagani. Nonlinear and linearized vibration analysis of plates and shells subjected to compressive loading. *International Journal of Non-Linear Mechanics*, 141:103936, 2022.

[48] R. Azzara, E. Carrera, M. Filippi, and A. Pagani. Time response stress analysis of solid and reinforced thin-walled structures by component-wise models. *International Journal of Structural Stability and Dynamics*, 20(14):2043010, 2020.

[49] I. Hirai, B. Wang, and W. Pilkey. An efficient zooming method for finite element analysis. *International Journal for Numerical Methods in Engineering*, 20:1671 – 1683, 1984.

[50] J. B. Ransom and N. F. Knight Jr. Global/local stress analysis of composite panels. *Computers & structures*, 37(4):375–395, 1990.

[51] K. M. Mao and C. T. Sun. A refined global-local finite element analysis method. *International Journal for Numerical Methods in Engineering*, 32(1):29–43, 1991.

[52] J. D. Whitcomb. Iterative global/local finite element analysis. *Computers & structures*, 40(4):1027–1031, 1991.

[53] A. K. Noor. Global-local methodologies and their application to nonlinear analysis. *Finite Elements in Analysis and Design*, 2(4):333–346, 1986.

[54] J. Whitcomb and K. Woo. Global/local finite element analysis of geometrically nonlinear structures. In *33rd Structures, Structural Dynamics and Materials Conference*, page 2236, 1992.

[55] I. Babuška, J. Chandra, and J. Flaherty. *Adaptive computational methods for partial differential equations*, volume 16. SIAM, 1983.

[56] I. Babuska, B. A Szabo, and N. Katz. The p-version of the finite element method. *SIAM Journal on Numerical Analysis*, 18(3):515–545, 1981.

[57] I. Babuška and M. Dorr. Error estimates for the combined h and p versions of the finite element method. *Numerische Mathematik*, 37(2):257–277, 1981.

[58] S. Hühne, J. Reinoso, E. Jansen, and R. Rolfes. A two-way loose coupling procedure for investigating the buckling and damage behaviour of stiffened composite panels. *Composite Structures*, 136:513–525, 2016.

[59] M. Akterskaia, E. Jansen, S. Hühne, and R. Rolfes. Efficient progressive failure analysis of multi-stringer stiffened composite panels through a two-way loose coupling global-local approach. *Composite Structures*, 183:137–145, 2018.

[60] M. Akterskaia, E. Jansen, S. Hallett, P. Weaver, and R. Rolfes. Analysis of skin-stringer debonding in composite panels through a two-way global-local method. *Composite Structures*, 202:1280–1294, 2018.

[61] G. Labeas, S. Belesis, I. Diamantakos, and K. Tserpes. Adaptative progressive damage modeling for large-scale composite structures. *International Journal of Damage Mechanics*, 21(3):441–462, 2012.

[62] L. Gendre, O. Allix, P. Gosselet, and F. Comte. Non-intrusive and exact global/local techniques for structural problems with local plasticity. *Computational Mechanics*, 44(2):233–245, 2009.

[63] R. Vescovini, C. Davila, and C. Bisagni. Failure analysis of composite multi-stringer panels using simplified models. *Composites Part B: Engineering*, 45(1):939–951, 2013.

[64] A. Orifici, R. Thomson, I. Herszberg, T. Weller, R. Degenhardt, and J. Bayandor. An analysis methodology for failure in postbuckling skin–stiffener interfaces. *Composite Structures*, 86(1-3):186–193, 2008.

[65] J.N. Reddy. *Mechanics of laminated composite plates and shells: theory and analysis*. CRC press, 2003.

[66] G. Silva, A. Do Prado, P. Cabral, R. De Breuker, and J. Dillinger. Tailoring of a composite regional jet wing using the slice and swap method. *Journal of Aircraft*, 56(3):990–1004, 2019.

[67] E. Carrera, A. de Miguel, M. Filippi, I. Kaleel, A. Pagani, M. Petrolo, and E. Zappino. Global-local plug-in for high-fidelity composite stress analysis in femap/NX nastran. *Mechanics of Advanced Materials and Structures*, 28(11):1121–1127, 2021.

[68] E. Carrera, A. G. De Miguel, M. Filippi, I. Kaleel, A. Pagani, M. Petrolo, and E. Zappino. Global-local plug-in for high-fidelity composite stress analysis in ABAQUS. *Mechanics of Advanced Materials and Structures*, 28(14):1445–1450, 2021.

[69] K. Diamanti and C. Soutis. Structural health monitoring techniques for aircraft composite structures. *Progress in Aerospace Sciences*, 46(8):342–352, 2010.

[70] A Rytter. Vibration based inspection of civil engineering structures [P.h.D. thesis]. *Aalborg University*, 1993.

[71] S. Kessler and S. Spearing. Damage detection in composite materials using lamb wave methods. *Smart Materials and Structures*, 11:269, 04 2002.

[72] R.S.C. Monkhouse, P. Wilcox, M.J.S. Lowe, R.P. Dalton, and P. Cawley. The rapid monitoring of structures using interdigital lamb. *Smart Materials and Structures*, 9:304, 06 2000.

[73] X. Bao and L. Chen. Recent progress in distributed fiber optic sensors. *Sensors (Basel, Switzerland)*, 12:8601–39, 2012.

[74] R. Sante. Fibre optic sensors for structural health monitoring of aircraft composite structures: Recent advances and applications. *Sensors (Basel, Switzerland)*, 15:18666–713, 08 2015.

[75] S.Z. Zhang, Y.J. Yan, and Z. Wu. Electric potential detection for structural surface crack using coating sensors. *Sensors and Actuators A: Physical*, 137:223–229, 2007.

[76] M. Şahin and R. Shenoi. Vibration-based damage identification in beam-like composite laminates by using artificial neural networks. *Journal of Mechanical Engineering Science*, 217:661–676, 2003.

[77] A. Pagani, R. Azzara, R. Augello, and E. Carrera. Stress states in highly flexible thin-walled composite structures by unified shell model. *AIAA Journal*, pages 1–14, 2021.

[78] L. Grassia, M. Iannone, A. Califano, and A. D'Amore. Strain based method for monitoring the health state of composite structures. *Composites Part B: Engineering*, 176:107253, 2019.

[79] Ho Hwang and Cheol Kim. Damage detection in structures using a few frequency response measurements. *Journal of Sound and Vibration*, 270:1–14, 02 2004.

[80] J. Zhou, Z. Li, and J. Chen. Damage identification method based on continuous wavelet transform and mode shapes for composite laminates with cutouts. *Composite Structures*, 191:12–23, 2018.

[81] C. Hirwani and S. Panda. Nonlinear transient analysis of delaminated curved composite structure under blast/pulse load. *Engineering with Computers*, 36, 2020.

[82] A. Labib, D. Kennedy, and C. Featherston. Free vibration analysis of beams and frames with multiple cracks for damage detection. *Journal of Sound and Vibration*, 333(20):4991–5003, 2014.

[83] R. Capozucca. Vibration of CFRP cantilever beam with damage. *Composite Structures*, 116:211–222, 2014.

[84] Y. Yan, Q. Ren, N. Xia, and L. Zhang. A close-form solution applied to the free vibration of the Euler–Bernoulli beam with edge cracks. *Archive of Applied Mechanics*, 86, 2016.

[85] M. Şahin and R. Shenoi. Quantification and localisation of damage in beam-like structures by using artificial neural networks with experimental validation. *Engineering Structures*, 25:1785–1802, 2003.

[86] H. Das and D. Parhi. Application of neural network for fault diagnosis of cracked cantilever beam. In *2009 World Congress on Nature and Biologically Inspired Computing, NABIC 2009 - Proceedings*, pages 1303 – 1308, 2010.

[87] S. Suresh, S. N. Omkar, R. Ganguli, and V. Mani. Identification of crack location and depth in a cantilever beam using a modular neural network approach. *Smart Materials and Structures*, 13, 2004.

[88] K. Sumangala. Damage assessment of prestressed concrete beams using Artificial Neural Network (ANN) approach. *Computers and Structures*, 84:1709–1718, 2006.

[89] R. A. Saeed, A. Galybin, and V. Popov. Crack identification in curvilinear beams by using ANN and ANFIS based on natural frequencies and frequency response functions. *Neural Computing and Applications*, 21:1629–1645, 2012.

[90] K. Aydin and O. Kisi. Damage diagnosis in beam-like structures by artificial neural networks. *Journal of Civil Engineering and Management*, 21, 2015.

[91] H. Fathnejat, P. Torkzadeh, E. Salajegheh, and R. Ghiasi. Structural damage detection by model updating method based on cascade feed-forward neural network as an efficient approximation mechanism. *Internationl journal of optimization in civil engineering*, 4:451–472, 2014.

[92] Y. LeCun, L. Bottou, Y. Bengio, and P. Haffner. Gradient-based learning applied to document recognition. *Proceedings of the IEEE*, 86(11):2278–2324, 1998.

[93] M. Saadatmorad, R.A. Jafari-Talookolaei, M. Pashaei, and S. Khatir. Damage detection on rectangular laminated composite plates using wavelet based convolutional neural network technique. *Composite Structures*, 278:114656, 2021.

[94] J. Wu, X. Xu, C. Liu, C. Deng, and X. Shao. Lamb wave-based damage detection of composite structures using deep convolutional neural network and continuous wavelet transform. *Composite Structures*, 276:114590, 2021.

[95] S. Teng, G. Chen, G. Liu, J. Lv, and F. Cui. Modal strain energy-based structural damage detection using convolutional neural networks. *Applied Sciences*, 9:3376, 2019.

[96] M. Slonski and M. Tekieli. 2D digital image correlation and region-based convolutional neural network in monitoring and evaluation of surface cracks in concrete structural elements. *Materials*, 13:3527, 08 2020.

[97] M. Enea, A. Pagani, and E. Carrera. Damage detection in composites by ai and high-order modelling surface-strain-displacement analysis. In *European Workshop on Structural Health Monitoring*, pages 330–337. Springer, 2023.

[98] N. Gulgec, M. Takáč, and S. Pakzad. Convolutional neural network approach for robust structural damage detection and localization. *Journal of Computing in Civil Engineering*, 33, 2019.

[99] Y. Wang, Q. Luo, H. Xie, Q. Li, and G. Sun. Digital image correlation (dic) based damage detection for cfrp laminates by using machine learning based image semantic segmentation. *International Journal of Mechanical Sciences*, page 107529, 2022.

[100] Bing P. Reliability-guided digital image correlation for image deformation measurement. *Appl. Opt.*, 48(8):1535–1542, 2009.

[101] M. Li, D. Jia, Z. Wu, Qiu. S., and W He. Structural damage identification using strain mode differences by the ifem based on the convolutional neural network (CNN). *Mechanical Systems and Signal Processing*, 165:108–289, 2022.

[102] A. Cabboi, C. Gentile, and A. Saisi. From continuous vibration monitoring to fem-based damage assessment: Application on a stone-masonry tower. *Construction and Building Materials*, 156:252–265, 2017.

[103] A. Forghani, A. Poursartip, and R. Vaziri. An orthotropic non-local approach to modeling intra-laminar damage progression in laminated composites. *International Journal of Solids and Structures*, 180:160–175, 2019.

[104] J. Lemaitre, A. Benallal, R. Billardon, and D. Marquis. *Thermodynamics and phenomenology*, pages 209–223. 01 2002.

[105] J. Lemaitre and J. L. Chaboche. *Mechanics of solid materials*. Cambridge university press, 1994.

[106] M. R. T. Arruda, L. Almeida-Fernandes, L. Castro, and J. R. Correia. Tsai–Wu based orthotropic damage model. *Composites Part C: Open Access*, 4:100122, 2021.

[107] M. R. T. Arruda, M. Trombini, and A. Pagani. Implicit to Explicit Algorithm for ABAQUS Standard User-Subroutine UMAT for a 3D Hashin-Based Orthotropic Damage Model. *Applied Sciences*, 13(2), 2023.

[108] Z. Hashin. Failure Criteria for Unidirectional Fiber Composites. *Journal of Applied Mechanics*, 47(2):329–334, 06 1980.

[109] I. Lapczyk and J. A. Hurtado. Progressive damage modeling in fiber-reinforced materials. *Composites Part A: Applied Science and Manufacturing*, 38(11):2333–2341, 2007.

[110] Z. Bazant and B. Oh. Crack Band Theory for Fracture of Concrete. *Matériaux et Constructions*, 16:155–177, 05 1983.

[111] M.H. Nagaraj, J. Reiner, R. Vaziri, E. Carrera, and M. Petrolo. Progressive damage analysis of composite structures using higher-order layer-wise elements. *Composites Part B: Engineering*, 190:107921, 2020.

[112] J. Shen, M. R. T. Arruda, and A. Pagani. A consistent crack bandwidth for higher-order beam theories: application to concrete. *International Journal of Damage Mechanics*, Submitted.

[113] S.A. Silling, M. Epton, O. Weckner, J. Xu, and E. Askari. Peridynamic states and constitutive modeling. *Journal of Elasticity*, 88(2):151–184, 2007.

[114] P. Seleson. Improved one-point quadrature algorithms for two-dimensional peridynamic models based on analytical calculations. *Computer Methods in Applied Mechanics and Engineering*, 282:184–217, 2014.

[115] F. Scabbia, M. Zaccariotto, and U. Galvanetto. Accurate computation of partial volumes in 3D peridynamics. *Engineering with Computers*, pages 1–33, 2022.

[116] F. Bobaru and Y.D. Ha. Adaptive refinement and multiscale modeling in 2D peridynamics. *Journal for Multiscale Computational Engineering*, 9(6):635–659, 2011.

[117] P. Seleson and D.J. Littlewood. Convergence studies in meshfree peridynamic simulations. *Computers & Mathematics with Applications*, 71(11):2432–2448, 2016.

[118] M.L. Parks, S.J. Plimpton, R.B. Lehoucq, and S.A. Silling. Peridynamics with LAMMPS: a user guide. Technical report, Sandia National Laboratories, 2008.

[119] J. T. Foster. *Dynamic crack initiation toughness: Experiments and peridynamic modeling*. PhD thesis, Purdue University, 2009.

[120] J. T. Foster, S. A. Silling, and W. Chen. An energy based failure criterion for use with peridynamic states. *International Journal for Multiscale Computational Engineering*, 9(6), 2011.

[121] E. Madenci and S. Oterkus. Ordinary state-based peridynamics for plastic deformation according to von mises yield criteria with isotropic hardening. *Journal of the Mechanics and Physics of Solids*, 86:192–219, 2016.

[122] D. Dipasquale, G. Sarego, M. Zaccariotto, and U. Galvanetto. A discussion on failure criteria for ordinary state-based peridynamics. *Engineering Fracture Mechanics*, 186:378–398, 2017.

[123] S. Silling and E. Askari. A meshfree method based on the peridynamic model of solid mechanics. *Computers & Structures*, 83:1526–1535, 2005.

[124] T. Ni, M. Zaccariotto, Q. Zhu, and U. Galvanetto. Static solution of crack propagation problems in peridynamics. *Computer Methods in Applied Mechanics and Engineering*, 346:126–151, 2019.

[125] K.J. Bathe. *Finite element procedure*. Prentice Hall, Upper Saddle River, New Jersey, USA, 1996.

[126] K. Washizu. *Variational Methods in Elasticity and Plasticity*. Pergamon, Oxford, 1968.

[127] E. Carrera. Theories and finite elements for multilayered plates and shells: a unified compact formulation with numerical assessment and benchmarking. *Archives of Computational Methods in Engineering*, 10(3):215–296, 2003.

[128] E. Carrera, A. Pagani, and M. Petrolo. Use of Lagrange multipliers to combine 1D variable kinematic finite elements. *Computers and Structures*, 129:194–206, 2013.

[129] S. P. Timoshenko. On the transverse vibrations of bars of uniform cross section. *Philosophical Magazine*, 43:125–131, 1922.

[130] E. Carrera, G. Giunta, and M. Petrolo. *Beam structures: classical and advanced theories*. John Wiley & Sons, 2011.

[131] E. Carrera, G. Giunta, P. Nali, and M. Petrolo. Refined beam elements with arbitrary cross-section geometries. *Computers and Structures*, 88(5–6):283–293, 2010.

[132] E. Carrera, M. Maiarú, and M. Petrolo. Component-wise analysis of laminated anisotropic composites. *International Journal of Solids and Structures*, 49:1839–1851, 2012.

[133] E. Carrera, A. Pagani, and M. Petrolo. Classical, refined and component-wise theories for static analysis of reinforced-shell wing structures. *AIAA Journal*, 51(5):1255–1268, 2013.

[134] G. Giunta, F. Biscani, S. Belouettar, and E. Carrera. Analysis of thin-walled beams via a one-dimensional unified formulation through a navier-type solution. *International Journal of Applied Mechanics*, 3:407–434, 09 2011.

[135] A. Pagani, M. Boscolo, J. R. Banerjee, and E. Carrera. Exact dynamic stiffness elements based on one-dimensional higher-order theories for free vibration analysis of solid and thin-walled structures. *Journal of Sound and Vibration*, 332(23):6104–6127, 2013.

[136] E. Carrera, M. Cinefra, M. Petrolo, and E. Zappino. *Finite Element Analysis of Structures through Unified Formulation*. John Wiley & Sons, 2014.

[137] M. Zaccariotto, D. Tomasi, and U. Galvanetto. An enhanced coupling of PD grids to FE meshes. *Mechanics Research Communications*, 84:125–135, 2017.

[138] G. Ongaro, P. Seleson, U. Galvanetto, T. Ni, and M. Zaccariotto. Overall equilibrium in the coupling of peridynamics and classical continuum mechanics. *Computer Methods in Applied Mechanics and Engineering*, 381:113515, 2021.

[139] S.A. Silling. Linearized theory of peridynamic states. *Journal of Elasticity*, 99(1):85–111, 2010.

[140] T. Ni, M. Zaccariotto, Q.Z. Zhu, and U. Galvanetto. Coupling of FEM and ordinary state-based peridynamics for brittle failure analysis in 3D. *Mechanics of advanced materials and structures*, 28(9):875–890, 2021.

[141] R. H. MacNeal. *The NASTRAN theoretical manual*, volume 221. Scientific and Technical Information Office, National Aeronautics and Space, 1970.

[142] E. Reissner and Y. Stavsky. Bending and Stretching of Certain Types of Heterogeneous Aeolotropic Elastic Plates, 1961.

[143] R. Augello, A. Pagani, E. Carrera, and A. Iannotta. Stress and failure onset analysis of thin composite deployables by global/local approach. *AIAA Journal*, pages 1–13, 2022.

[144] R. Mindlin. Influence of rotatory inertia and shear on flexural motions of isotropic, elastic plates. *Journal of Applied Mechanics-transactions of The Asme*, 18:31–38, 1951.

[145] J. Reiner, T. Feser, D. Schueler, M. Waimer, and R. Vaziri. Comparison of two progressive damage models for studying the notched behavior of composite laminates under tension. *Composite Structures*, 207:385–396, 2019.

[146] L. Almeida-Fernandes, N. Silvestre, and J. R. Correia. Characterization of transverse fracture properties of pultruded GFRP material in tension. *Composites Part B: Engineering*, 175:107095, 2019.

[147] A. M. Girão Coelho, J. Toby Mottram, and K. A. Harries. Finite element guidelines for simulation of fibre-tension dominated failures in composite materials validated by case studies. *Composite Structures*, 126:299–313, 2015.

[148] L. Almeida-Fernandes, N. Silvestre, J. R. Correia, and M. R. T. Arruda. Fracture toughness-based models for damage simulation of pultruded GFRP materials. *Composites Part B: Engineering*, 186:107818, 2020.

[149] T.J.R. Hughes. *The finite element method: linear static and dynamic finite element analysis*. Courier Corporation, 2012.

[150] B. Lopes, M. R. T. Arruda, L. Almeida-Fernandes, L. Castro, N. Silvestre, and J. R. Correia. Assessment of mesh dependency in the numerical simulation of compact tension tests for orthotropic materials. *Composites Part C: Open Access*, 1:100006, 2020.

[151] W. Liu, P. Feng, and J. Huang. Bilinear softening model and double K fracture criterion for quasi-brittle fracture of pultruded FRP composites. *Composite Structures*, 160:1119–1125, 2017.

[152] A. Pagani and E. Carrera. Coupling three-dimensional peridynamics and high-order one-dimensional finite elements based on local elasticity for the linear static analysis of solid beams and thin-walled reinforced structures. *International Journal for Numerical Methods in Engineering*, 121(22):5066–5081, 2020.

[153] E. Carrera and A. Pagani. Analysis of reinforced and thin-walled structures by multi-line refined 1D/beam models. *International Journal of Mechanical Sciences*, 75:278–287, 2013.

[154] E. Carrera, A. Pagani, and M. Petrolo. Classical, refined, and component-wise analysis of reinforced-shell wing structures. *AIAA journal*, 51(5):1255–1268, 2013.

[155] A. Pagani and E. Carrera. Coupling 3D peridynamics and high order 1D finite elements based on local elasticity for the linear static analysis of solid beams and thin-walled reinforced structures. *International Journal for Numerical Methods in Engineering*, 121, 2020.

[156] R. Durand and F. Silva. Three-dimensional modeling of fracture in quasi-brittle materials using plasticity and cohesive finite elements. *International Journal of Fracture*, 228:1–26, 2021.

[157] F. Bobaru, M. Yang, L. Frota Alves, S. Silling, E. Askari, and J. Xu. Convergence, adaptive refinement, and scaling in 1d peridynamics. *International Journal for Numerical Methods in Engineering*, 77:852–877, 2009.

[158] Brokenshire DR. *A study of torsion fracture tests*. PhD thesis, Cardiff University, 1995.

[159] A. Jefferson, B.I.G. Barr, T. Bennett, and S.C. Hee. Three dimensional finite element simulation of fracture test using craft concrete model. *Computers and Concrete*, 1, 2004.

[160] T. Gasser and G. Holzapfel. 3D crack propagation in unreinforced concrete.: A two-step algorithm for tracking 3D crack paths. *Computer Methods in Applied Mechanics and Engineering*, 195:5198–5219, 2006.

[161] E. Gurses and C. Miehe. A computational framework of three dimensional configurational-force-driven crack propagation. *Computer Methods in Applied Mechanics and Engineering - COMPUT METHOD APPL MECH ENG*, 198:1413–1428, 2009.

[162] I. Zreid and M. Kaliske. A gradient enhanced plasticity–damage microplane model for concrete. *Computational Mechanics*, 62, 2018.

[163] T. NI, M. Zaccariotto, Q. Zhu, and U. Galvanetto. Coupling of FEM and ordinary state-based peridynamics for brittle failure analysis in 3D. *Mechanics of Advanced Materials and Structures*, 2019.

[164] K. Wright. Chebyshev Collocation Methods for Ordinary Differential Equations. *The Computer Journal*, 6(4):358–365, 1964.

[165] E. Carrera. Historical review of zig-zag theories for multilayered plates and shells. *Appl. Mech. Rev.*, 56(3):287–308, 2003.

[166] Z. Hashin. Failure criteria for unidirectional fiber composites. *Journal of Applied Mechanics*, 47(2):329–334, 1980.

[167] T. H. Lorriot, G. Marion, R. Harry, and H. Wargnier. Onset of free-edge delamination in composite laminates under tensile loading. *Composites Part B: Engineering*, 34(5):459–471, 2003.

[168] R. B. Pipes and N. J. Pagano. Interlaminar stresses in composite laminates under uniform axial extension. *Journal of composite materials*, 4(4):538–548, 1970.

[169] R. B. Pipes and N. J. Pagano. Interlaminar stresses in composite laminates—an approximate elasticity solution. *Journal of Applied Mechanics*, 41(3):668–672, 1974.

[170] A.G. de Miguel, E. Carrera, A. Pagani, and E. Zappino. Accurate evaluation of interlaminar stresses in composite laminates via mixed one-dimensional formulation. *AIAA Journal*, 56:1–13, 09 2018.

[171] M. Shahbazi. *An efficient virtual testing framework to simulate the progression of damage in notched composite laminates*. PhD thesis, University of British Columbia, 2017.

[172] E. Carrera, A. Pagani, and M. Petrolo. Free vibrations of damaged aircraft structures by Component-Wise analysis. *AIAA Journal*, 54:1–16, 2016.

[173] E. Carrera, A. Pagani, and M. Petrolo. Component-Wise method applied to vibration of wing structures. *Journal of Applied Mechanics*, 80(4):041012, 2013.

[174] H. B. Demuth, M. H. Beale, O. De Jess, and M. T. Hagan. *Neural Network Design*. Martin Hagan, 2nd edition, 2014.

[175] P. Benardos and G. Vosniakos. Optimizing feedforward artificial neural network architecture. *Engineering Applications of Artificial Intelligence*, 20:365–382, 2007.

[176] J. Arifovic and R. Gençay. Using genetic algorithms to select architecture of a feedforward artificial neural network. *Physica A: Statistical Mechanics and its Applications*, 289:574–594, 01 2001.

[177] Y. Bengio, Y. LeCun, and D. Henderson. Globally trained handwritten word recognizer using spatial representation, convolutional neural networks, and hidden markov models. In J. Cowan, G. Tesauro, and J. Alspector, editors, *Advances in Neural Information Processing Systems*, 1993.

[178] Inc. The MathWorks. *Deep learning toolbox*. Natick, Massachusetts, United State, 2020.